DUCTILE-BRITTLE FRACTURE OF AMORPHOUS GLASSY POLYMERS

A THESIS SUBMITTED TO
THE GRADUATE SCHOOL OF NATURAL AND APPLIED SCIENCES
OF
MIDDLE EAST TECHNICAL UNIVERSITY

BY

SELÇUK BAŞDEMİR

IN PARTIAL FULFILLMENT OF THE REQUIREMENTS
FOR
THE DEGREE OF MASTER OF SCIENCE
IN
MECHANICAL ENGINEERING

SEPTEMBER 2024

Approval of the thesis:

DUCTILE-BRITTLE FRACTURE OF AMORPHOUS GLASSY POLYMERS

submitted by **SELÇUK BAŞDEMİR** in partial fulfillment of the requirements for the degree of **Master of Science in Mechanical Engineering Department, Middle East Technical University** by,

Prof. Dr. Naci Emre Altun
Dean, Graduate School of **Natural and Applied Sciences** _____

Prof. Dr. Serkan Dağ
Head of Department, **Mechanical Engineering** _____

Prof. Dr. Hüsnü Dal
Supervisor, **Mechanical Engineering Department, METU** _____

Examining Committee Members:

Prof. Dr. Haluk Darendeliler
Mechanical Engineering, METU _____

Prof. Dr. Hüsnü Dal
Mechanical Engineering, METU _____

Prof. Dr. Serkan Dağ
Mechanical Engineering, METU _____

Assoc. Prof. Dr. Ercan Gürses
Aerospace Engineering, METU _____

Assoc. Prof. Dr. Cihan Tekoğlu
Mechanical Engineering, TOBB _____

Date:05.09.2024

I hereby declare that all information in this document has been obtained and presented in accordance with academic rules and ethical conduct. I also declare that, as required by these rules and conduct, I have fully cited and referenced all material and results that are not original to this work.

Name, Surname: Selçuk Başdemir

Signature :

ABSTRACT

DUCTILE-BRITTLE FRACTURE OF AMORPHOUS GLASSY POLYMERS

Başdemir, Selçuk
M.S., Department of Mechanical Engineering
Supervisor: Prof. Dr. Hüsnü Dal

September 2024, 87 pages

Amorphous glassy polymers are extensively used in industrial sectors like microelectronics, medical devices, and aerospace. Their design and application have become crucial due to their varying fracture responses, which can range from ductile to brittle depending on factors such as entanglement density, temperature, and loading rate. Ductile responses are driven by diffuse shear zones exhibiting volume-preserving inelastic deformations, while brittle responses are manifested by small crack-like defects with fibrillar bridges separated by micro-voids, indicating void formation through nucleation and propagation.

This thesis focuses on describing shear yielding and crazing phenomena through evolution equations. It also extends the modeling of fracture using a crack phase-field approach, allowing for the simultaneous consideration of ductile and brittle failure. This approach is based on a novel failure criterion that features both a critical amount of plastic strain and void volume fraction, making it more physically grounded than current models. Additionally, a coupled thermo-mechano-fracture model for amorphous glassy polymers is introduced, enabling simultaneous treatment of ductile and brittle fracture.

Constitutive formulations for shear yielding, crazing, and void volume fraction are derived, starting with the local and conductive components of the dissipation inequality. The model's governing equations integrate mechanics with the crack phase-field and temperature evolution, addressing the global thermal problem—a key focus of this research. The model's performance is evaluated using local and global Newton-type update algorithms, tested against experimental data from homogeneous and inhomogeneous tests, revealing significant temperature dependency on failure type and interaction between loading rate and temperature due to dissipative heating.

Keywords: Amorphous glassy polymers, Crack phase–field, Crazing, Finite thermo-viscoplasticity, Void growth

ÖZ

AMORF CAMSI POLİMERLERİN SÜNEK-GEVREK KIRILMASI

Başdemir, Selçuk
Yüksek Lisans, Makina Mühendisliği Bölümü
Tez Yöneticisi: Prof. Dr. Hüsnü Dal

Eylül 2024 , 87 sayfa

Amorf camsı polimerler, mikroelektronik, tıbbi cihazlar ve havacılık gibi sanayi alanlarında yaygın olarak kullanılmaktadır. Tasarımları ve kullanımları, dolanma yoğunluğu, sıcaklık ve yükleme hızı gibi faktörlere bağlı olarak sünekten gevreğe değişebilen kırılma tepkileri nedeniyle önemli hale gelmiştir. Sünek tepkiler, hacim koruyucu inelastik deformasyonlar sergileyen yaygın kesme bölgeleriyle, gevrek tepkiler ise mikro boşluklarla ayrılmış fibril köprülerden oluşan küçük çatlak benzeri kusurlarla ortaya çıkar. Bu durum, boşluk oluşumunun çekirdeklenme ve yayılma adımlarını içerdiğini gösterir.

Bu tez, kesme akması ve çatlama olgusunun evrim denklemleriyle tanımlanmasına odaklanmaktadır. Ayrıca, sünek ve gevrek kırılmayı aynı anda ele almayı sağlayan bir çatlak faz alanı yaklaşımı ile kırılma modellemesi genişletilmiştir. Bu yaklaşım, hem kritik plastik deformasyonu hem de boşluk hacim fraksiyonunu içeren yeni bir hasar kriterine dayanmaktadır ve mevcut modellere kıyasla daha fiziksel temelli olduğu iddia edilmektedir. Ayrıca, amorf camsı polimerler için önerilen bu hasar kriterine dayalı bir termomekanik-kırılma modeli sunularak sünek ve gevrek kırılma aynı anda ele alınabilmektedir.

Kesme akması, çatlama ve boşluk hacmi fraksiyonu için türetilen yapısal formüller, yerel ve iletken bileşenlerin yitim eşitsizliğiyle başlar. Modelin mekanik denklemleri, çatlak faz alanı ve sıcaklık evrim denklemiyle birleştirilmiş ve çalışmanın temel odak noktalarından biri olan genel termal problem ele alınmıştır. Modelin performansı, yerel ve genel Newton tipi güncelleme algoritmalarıyla değerlendirilmiş, homojen ve heterojen testlerden elde edilen deneysel verilere dayanarak test edilmiştir. Bulgular, sıcaklığın kırılma türü üzerindeki önemli etkisi ile yükleme hızı ve katıdaki yayılabilir ısı nedeniyle sıcaklık değişimi arasındaki etkileşimi ortaya koymuştur.

Anahtar Kelimeler: Amorf camsı polimerler, Çatlak faz alanı, Çatlama, Sonlu termo-viskoplastisite, Boşluk büyümesi

I dedicate this thesis to Turkish film director and producer Zeki Demirkubuz and his great movie Kader (El Destino, 2006)

ACKNOWLEDGMENTS

I would like to express my deepest gratitude to my advisor, Prof. Dr. Hüsnü Dal, for his continuous support, guidance, and encouragement throughout my thesis. His expertise and invaluable insights have been instrumental in shaping this thesis, and his patience and understanding have been a constant source of motivation.

This work is built upon the valuable contributions of Dr. Osman Gültekin. I am deeply grateful for his support during my early steps in academia, which has been instrumental in guiding my research and development.

I would also like to extend my thanks to the faculty and staff of the Mechanical Engineering Department at Middle East Technical University for providing a stimulating academic environment.

Special thanks to my laboratory colleagues, Dr. Kemal Açıkgöz, Dr. Oğuz Ziya Tikenoğulları, Alp Kağan Açan, Bülent Efe Tanış, Recep Durna and Yasin Gargı who consistently provided their ideas and support throughout the thesis studies and my other research endeavours and also for making this journey a memorable one.

My heartfelt thanks go to my parents Sadi Başdemir and Güler Başdemir, and my brother Burak Başdemir for their unwavering support and belief in me. Their encouragement has been the driving force behind my achievements.

Lastly, I also extend my sincere thanks to my close friends, Furkan Çağatay Korkmaz, Semih Durmaz and Tahsin Ahi, who have been my pillars of support throughout this journey. Your encouragement, understanding, and friendship have made the challenges of this process more bearable and the successes more meaningful.

TABLE OF CONTENTS

LIST OF TABLES

TABLES

LIST OF FIGURES

FIGURES

LIST OF ABBREVIATIONS

FEM	Finite element method
XFEM	Extended finite element method
CZM	Cohesive zone modeling
TEM	Transmission electron micrograph
HVEM	High–voltage electron micrograph
PC	Polycarbonate
PS	Polystyrene
PMMA	Poly-methylmethacrylate
NR	Newton-Raphson
$\mathcal{B}$	Denotes the body
$\partial\mathcal{B}$	Denotes the boundary of the body
$\mathcal{P}$	Particle $\mathcal{P}$ in body $\mathcal{B}$
$\{\boldsymbol{e_1}, \boldsymbol{e_2}, \boldsymbol{e_3}\}$	Reference frame for spatial coordinates
$\{\boldsymbol{E_1}, \boldsymbol{E_2}, \boldsymbol{E_3}\}$	Reference frame for material coordinates
χ_0	Reference configuration
χ_t	A configuration at time t
$\boldsymbol{X}$	Coordinates of a point in material representation
$\boldsymbol{x}$	Coordinates of a point in spatial representation
$\boldsymbol{U}$	Displacement vector in material representation
$\boldsymbol{u}$	Displacement vector in spatial representation
$\boldsymbol{V}$	Velocity vector in material representation
$\boldsymbol{v}$	Velocity vector in spatial representation
$\boldsymbol{A}$	Acceleration vector in material representation
$\boldsymbol{a}$	Acceleration vector in spatial representation
$\boldsymbol{F}$	Deformation gradient
$\boldsymbol{U}$	Right stretch tensor
$\boldsymbol{v}$	Left stretch tensor
J	Determinant of deformation gradient

$d\boldsymbol{X}$	Lagrangian infinitesimal line element
$d\boldsymbol{x}$	Eulerian infinitesimal line element
$d\boldsymbol{A}$	Lagrangian infinitesimal area element
$d\boldsymbol{a}$	Eulerian infinitesimal area element
dV	Lagrangian infinitesimal volume element
dv	Eulerian infinitesimal volume element
λ_a	Principle stretches
$\boldsymbol{N}_a$	Eigenvectors in Lagrangian coordinates
$\boldsymbol{n}_a$	Eigenvectors in Eulerian coordinates
$\boldsymbol{C}$	Right Cauchy-Green tensor
$\boldsymbol{b}$	Left Cauchy-Green tensor (or Finger tensor)
$\mathcal{S}$	A cut region
$\partial\mathcal{S}$	Boundary of a cut region
$\boldsymbol{t}(\boldsymbol{x}, \boldsymbol{n})$	Traction vector at $\boldsymbol{x}$ with normal n
$\boldsymbol{\sigma}$	Cauchy stress tensor
$\boldsymbol{P}$	First Piola-Kirchhoff stress tensor
$\boldsymbol{\tau}$	Kirchhoff stress tensor
$\boldsymbol{S}$	Second Piola-Kirchhoff stress tensor
ψ	Helmholtz free energy
$\boldsymbol{g}$	Eulerian metric tensor
$\boldsymbol{G}$	Lagrangian metric tensor
μ	Shear modulus
κ	Bulk modulus
ν	Poisson's ratio
N	Order of material model
$\mathbb{C}$	Tangent modulus
ε	Strain
q	Local heat flux density
k	Material conductivity
∇T	Temperature gradient

CHAPTER 1

MOTIVATION AND OVERVIEW

1.1 Introduction

Optimal use and design of materials in goods have become a significant task in the key industrial sectors ranging from micro–electronics to aerospace and medical industry. Mechanical properties such as low weight and high fracture toughness blended with workability and manufacturability ultimately render polymers, especially thermoplastics, superior over metals. Thermoplastics are distinguished from thermosets by their behavior with rising temperature levels. In fact, thermoplastics can melt when heated above melting temperature θ_m owing to their secondary bonds, e.g., van der Waals and hydrogen, forming the entanglements between polymer chains. Most thermoplastics possess linear or branched molecular structure unlike the cross–linked network structure associated with thermosets. Classified under thermoplastics amorphous glassy polymers, such as polystyrene (PS), polycarbonate (PC) and polymethylmethacrylate (PMMA) have broad end–use applications in the industry. Therefore, it is of utmost interest to assess the durability and the fracture response of those polymers when subjected thermal and mechanical loading. For details regarding the basics of polymeric materials, we refer among others to POWELL & HOUSZ [99] and HAWARD & YOUNG [56]. The aforementioned properties of glassy polymers heavily depend on the microstructure (entanglement density and the anisotropy in the molecular alignment), temperature level and the external loading rate which may transition the fracture response from ductile to brittle or vice versa. The brittle response of amorphous polymers is revealed by very small, see Fig. 1.1(a), inelastically deformed zones, namely *crazes* whose thickness is measured in some micrometers, see KRAMER [72]. Crazes are very small crack-like defects containing a sequence

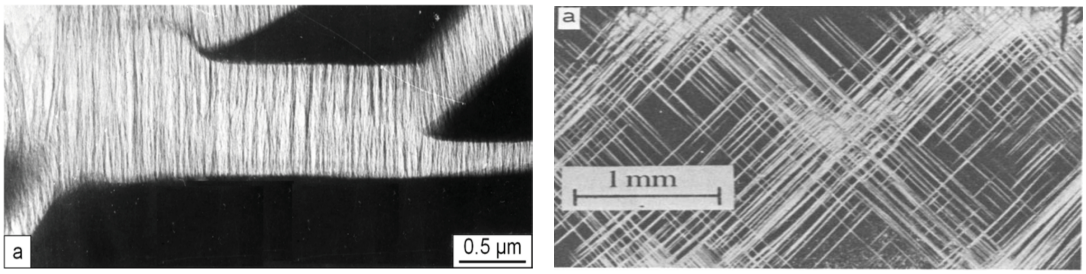

a) *b*)

Figure 1.1: High–voltage electron micrograph (HVEM) and transmission electron micrograph (TEM) images of PS films undergoing (a) fibrillar bridge formation, adopted from MICHLER & BALTÁ-CALLEJA [83]; (b) micro–shear bands, adopted from BOWDEN & RAHA [24], respectively.

of fibrillar bridges and elongated micro–voids, thereby resembling the void formation consisting of nucleation and growth stages. Their formation is driven by tensile straining followed by volumetric inelastic deformations. In fact, the development of crazes is favored by high strain-rate, relatively low temperature levels (well below glass transition temperature θ_g), and low entanglement density. The ductile response of amorphous polymers is, on the other hand, manifested by diffuse shear zones involving much larger amount of material and thereby a larger process zone, see Fig. 1.1(b). These zones are created by *shear yielding* mechanisms which are accompanied by substantial volume-preserving inelastic deformations. Shear yielding generally occurs under low strain-rate, relatively high temperature levels (around glass transition temperature θ_g) and high entanglement density. Addition of various fillers in glassy polymers promote multiple concurrent craze nucleation sites enhancing the fracture toughness remarkably as indicated by SEELIG & VAN DER GIESSEN [103, 104].

1.2 Literature Overview

1.2.1 Shear yielding in amorphous glassy polymers

At high temperature levels and low strain–rate amorphous glassy polymers exhibit volume-preserving plastic deformations as the yield stress is reached earlier than the crazing stress, i.e. stress necessary to initiate crazing, see BERGER & KRAMER [18] and IMAI & BROWN [59]. Besides, amorphous polymers such as PC predominantly experience shear yielding due to their high entanglement density making it hard for

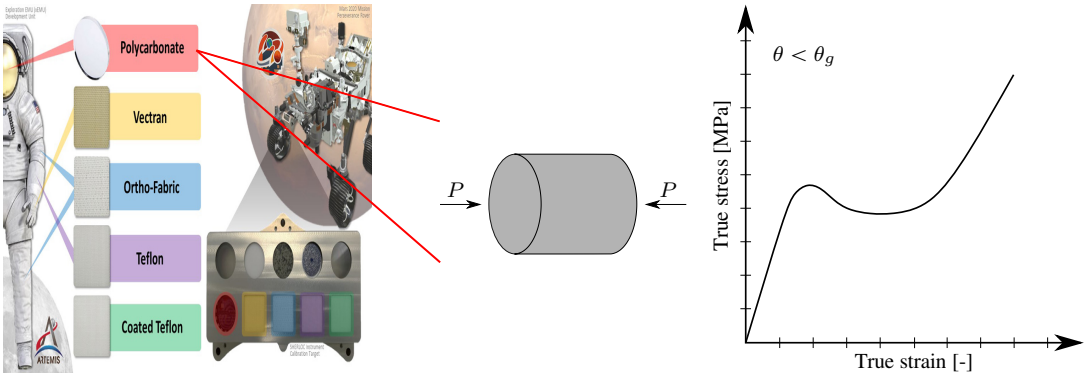

Figure 1.2: PC used in spacesuits especially for helmet bubbles and visors. Qualitative true stress-strain relationship typical for PC subjected to uniaxial compression P leading to ductile fracture. Reconstructed from www.nasa.gov.

crazes to develop. A qualitative ductile response of a cylindrical PC specimen under compressive load P is illustrated in Fig. 1.2.

The elasto–viscoplastic response of amorphous polymers originates from the disordered micro–structure inherent in the material. The well–accepted studies by ARGON [10] and BOYCE ET AL. [26] state that an amorphous polymer must overcome two physical source of resistance prior to the ductile mechanical response; first, the inter–molecular resistance to segment rotation which is explained by the *double–kink theory* and second, the entropic resistance to molecular orientation, the so–called rubbery response. While the double–kink theory sets a free enthalpy barrier by the surrounding chains to the rotation of a double–kink formed in a single chain, the entropic resistance corresponds to an external stress state that retains the texture in the sense of plastic stretches as the chains orient themselves in the principal loading directions.

We refer to the seminal works of ARGON [10], BOYCE ET AL. [26], ARRUDA ET AL. [14, 16] and HASAN & BOYCE [53] for the fundamentals of the finite viscoplastic response of glassy polymers due to shear yielding. The theory is further elaborated by WU & VAN DER GIESSEN [116–118], TOMITA & TANAKA [109], GOVAERT ET AL. [48], ANAND ET AL. [5–7], MIEHE ET AL. [89, 90], and FLEISCHHAUER ET AL. [43]. Pre– and post–yield softening of PC as seen in the load–displacement diagrams during the cold–drawing process are conspicuously smooth and curved [89]. In order to account for this smooth transition, HASAN & BOYCE [53] proposed the *free volume flow theory* that considers several internal variables motivated by microme-

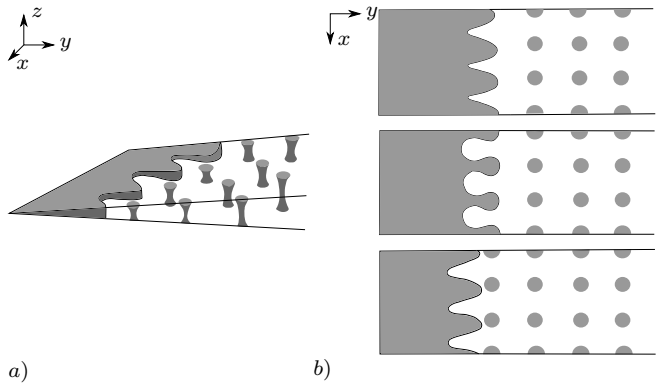

Figure 1.3: Schematic description of (a) wedge–shaped craze tip advance as the stress induced melt transforms into fibrils via the Taylor meniscus instability; (b) xy–plane of craze depicting the cascade of events leading to craze tip advance starting from the top image. Reconstructed from KRAMER [72].

chanics. The *local free volume* theory presented by ANAND & GURTIN [7], on the other hand, introduces a single scalar state variable representing the free volumes due to plastic deformation. A three–dimensional, thermo-mechanical extension of the approach, i.e. [53], was conducted by MIEHE ET AL. [90], whereas an endochronic time scale in the sense of VALANIS [113] and an activation free energy modified from KOCKS ET AL. [71] were added into the flow rule by FLEISCHHAUER ET AL. [43] improving the modeling capacity in the neighborhood of the yield point as well as capturing the rate dependency of the yield point over a wide range.

1.2.2 Crazing in amorphous glassy polymers

Crazes can be visualized as very small, localized, and plastically deformed zones consisting of a dense array of fibrils separated by microvoids. Craze phenomenon can be observed in three stages, namely, the initiation, growth and the breakdown, respectively. Locations where crazes nucleate are naturally existing surface grooves and dust particles or rubber particles added into the microstructure. The embryonic phase of crazing has an initial width ranging between 5–20 [nm] rendering craze initiation largely elusive. As a matter of fact, there exist no holistic explanation untangling the mystery despite the abundance of experiments. Nonetheless, it is conjectured that the localization of plastic strains induces lateral stresses which, in turn, leads to high hydrostatic stresses resulting in voids which link up with remaining polymer ligaments

between them. Afterwards, they turn into stable fibrillar crazes. More comprehensive information can be found in the reviews of KAMBOUR [68], KRAMER [72], ISHIKAWA ET AL. [61] and references therein. Criteria for craze initiation can be investigated in terms of (i) principal stresses, e.g., STERNSTEIN & MYERS [105]; (ii) principal strains, e.g., OXBOROUGH & BOWDEN [98]; (iii) the linear elastic fracture mechanics (LEFM), e.g., ANDREWS & BEVAN [8] and BUCKNALL [29]; (iv) lowering of the glass transition temperature at sites of craze nucleation, e.g., GENT [47]; (v) a cavitation problem triggered by triaxial stresses, e.g., KRAMER [72] and ARGON ET AL. [9, 12].

The fibrils generated lie normal to the craze bulk-interface and grow in the direction of maximum principal stress in the isotropic material. Such an advance in width occurs as the new material from craze bulk-interface is drawn into the fibrils, elongating them under constant stretch and thickness analogous to the cold drawing mechanism of macroscopic polymer fibers, see KRAMER [72]. The propagation of a craze in length is explained by the *Taylor meniscus instability* in which the tip of the craze melts into several void fingers as illustrated in Fig. 1.3. Introduced first by ARGON [11], this mechanism is elaborated through experiments on PS by ARGON & SALAMA [13]. In the meniscus instability, the yielded polymer at the air–polymer interface around the craze tip constitutes a melted layer into which the so–called meniscus propagates. At this point, if loading continues, then the fibrils are further extended due to decrease in the entanglement density in the middle of each fibril, thereby making them more likely to break. Amorphous polymers such as PMMA primarily exhibit crazing induced brittle response due to the low entanglement density. A qualitative brittle response of a dog–bone shaped PMMA specimen subjected to tensile loading P is illustrated in Fig. 1.4.

To date, numerous studies have been proposed to model the crazing induced failure in amorphous polymers according to; (i) the critical crack tip opening displacement incorporated into cohesive zone type discrete models, e.g., TIJSSENS ET AL. [108], based on the interferometric measurements carried out by DÖLL [40]; (ii) critical inelastic strain criterion, e.g., GEARING & ANAND [45]; (iii) the fracture toughness, e.g., HUI ET AL. [58]. Apart from that YANG ET AL. [119] developed a microscopic statistical model in which a Weibull distribution reflects the craze fibril breakdown by

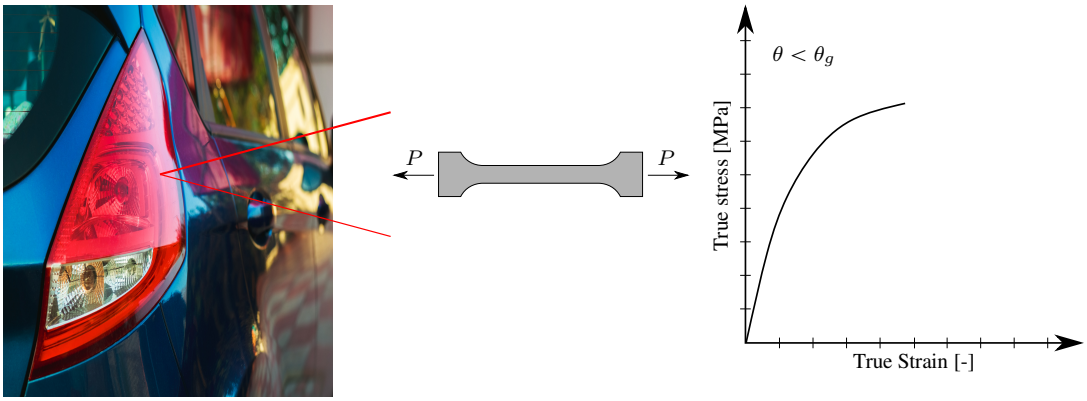

Figure 1.4: PMMA used in a stop lamp on an automobile. Qualitative true stress-strain relationship typical for PMMA subjected to uniaxial extension P leading to brittle fracture.

means of the random disentanglement of molecular strands at the craze–bulk interface.

1.2.3 Phase field models of fracture

Modeling of fracture in materials have seen a paradigm shift over the last two decades. Instead of handling the discontinuities via discrete methods such as cohesive zone modeling (CZM) and extended finite element method (XFEM), the crack phase field approach (CPF) avoids the realization of those sharp crack topologies and surmounts the well-known shortcomings, i.e. determination of curvilinear crack paths, crack kinking and branching angles, of the classical theory of brittle fracture treated in GRIFFITH [49] and IRWIN [60]. Based on the variational principle the early treatments of CPF, e.g., FRANCFORT & MARIGO [44], BOURDIN ET AL. [22], BULIGA [30], BRAIDES [27], feature a diffuse crack topology between the intact and the ruptured parts of the solid converging to the free discontinuity problem, i.e. Γ-convergence, as the length scale parameter l vanishes in the limit case. Recent contributions by MIEHE ET AL. [91, 94] defines fracture only in tension, a precise characterization of the dissipation, and introduce an artificial viscosity that stabilizes post-critical solution paths. CPF approach has been successfully applied to several multi–physics problems including, but not restricted to, thermo-elasto-plastic brittle and ductile fracture, such as AMBATI ET AL. [2–4], BORDEN ET AL. [20, 21], and MIEHE ET AL. [85,86,88,92,93] in isotropic materials. Anisotropic CPF models were

among others presented by LI ET AL. [76], TEICHTMEISTER ET AL. [107], CLAYTON & KNAP [32], NGUYEN ET AL. [97], GÜLTEKIN ET AL. [50–52], MANDAL ET AL. [78, 79], and DENLI ET AL. [39].

1.3 Scope of the thesis

Despite the evident influence on the mechanical response, there are very few contributions attempting to model the competition between ductile and brittle behavior of amorphous polymers. ESTEVEZ ET AL. [42] proposed a cohesive zone formulation through craze and cohesive surface opening rate along with the craze initiation sensitivity. The drawback of the study is the dependence of the model on *a priori* existing crack inserted in the mesh. The models presented by GEARING & ANAND [45] and JIANG ET AL. [67] are independent from the existing crack tip. However, they are not mesh objective as being based on element deletion technique upon the critical craze strain is reached. The very recent contributions made by MIEHE ET AL. [92] and NARAYAN & ANAND [96] incorporated CPF approach in order to model the brittle and ductile fracture in view of the critical value of the accumulated craze strain and/or the disentanglement strain akin to plastic strain, respectively.

In this contribution, we propose a new *constitutive model* for the ductile and brittle fracture of amorphous polymers that relates the phenomena of crazing to a physical measure, improving experimental observations and better informing the theoretical and numerical approaches. In addition, a new *failure criterion* that synchronously predicts shear yielding and crazing induced crack initiation and growth in the context of crack phase–field approach is presented. To this end, Argon–type viscoplastic flow rule in the sense of BOYCE ET AL. [26] in combination of the local free volume theory by ANAND & GURTIN [7] are adopted for the shear yielding of amorphous glassy polymers, while the craze flow is treated according to GEARING & ANAND [45]. Concurrent evolution of the dilatational and volume preserving plastic flow is inhibited by a stress based craze initiation criterion based on [45] which is incorporated into a switch function. In this work, we have conceptually combined the scalar state variable describing the local free volume theory with the void volume fraction in the case of shear induced flow. Besides, the normal components of the rate of the craze strain drives the growth of the void volume fraction in the case of craze induced flow.

Craze nucleation is promoted by both the hydrostatic and deviatoric components of the tensile stress, corroborating our hypothesis that the void volume fraction is driven by both shear yielding and crazing parts. We follow MIEHE ET AL. [87] and establish the entire kinematic framework in the logarithmic strain space based on metric tensors describing shear yielding and crazing. The proposed failure criterion features the critical amounts of plastic strain and void volume fraction. Such a modality predicts the macroscopic crack initiation and growth at once, leading to ductile or brittle failure, as such purports to be more physically grounded compared to what have been proposed so far in the literature.

The thesis is organized as follows: The investigation starts in Chapter 2 with continuum mechanics prelimenary. All mathematical background to be able to understand proposed work is provided in this chapter, briefly. Chapter 3 deals with underlying kinematics and the thermodynamical restrictions and the evolution equations emanating from shear yielding and crazing behavior, which, in turn, drive the evolution of the void volume fraction. In the sequel, the global form of the multi-physics problem is outlined with regard to balance and non–local evolution equations reflecting the deformation and the crack phase-field. Then, specific forms of the constitutive functions governing the finite viscoplasticity of amorphous glassy polymers and the novel failure criterion elucidating the ductile and brittle fracture. Finally, the capability of the model is assessed via verification and validation of the proposed algorithm with respect to representative homogeneous and inhomogeneous tests in Chapter 4 and all the remarks are concluded in Chapter 5.

CHAPTER 2

INTRODUCTION TO CONTINUUM THEORY

In this chapter, It will be given a brief introduction to continuum mechanics to be able to clearly examine the proposed coupled thermo-viscoelastic fracture model for ductile-brittle failure of amorphous glassy polymers.

2.1 Basic concepts in Continuum Mechanics

Continuum mechanics is a branch of mechanics dealing with stresses in all states of matter (solid, liquid and gas) and flow or deformation of the materials. In continuum aproach, it is disregarded the molecular structure matter and imagine it as no gaps or empty spaces in the material. Beside the media we are considering, all the mathematical functions entering the theories are continous functions (at least piecewise continious). Therefore, this hypotetical continious material in space and time is called ***continuum*** or ***continious medium***. The method of continuum mechanics is used as powerful and effective tool to understand several physical phenomena sufficiently without detail knowledge of the complexity of the internal microstructure.
Continuum mechanics deals with interactions between forces, motions, heat fluxes, temperature changes at a specific point within a material. Unlike rigid-body mechanics, which disregards the deformation a body undergoes during motion, continuum mechanics focuses on the complex relationship between deformation and forces such as body forces (force per unit volume) and traction (force per unit area). Additionally, continuum mechanics provides a thorough analysis of both translational and rotational motion of a body. Fundamental equations in continuum mechanics can be classified into two categories:

Physical conservation laws

- balance of mass
- balance of linear momentum
- balance of angular momentum
- balance of energy *(first law of thermodynamics)*
- balance of entropy *(second law of thermodynamics)*

Constitutive equations specific to material

- stress-strain relation
- heat flux-temperature (gradient) relation for heat conduction $(q = -k\nabla T)$

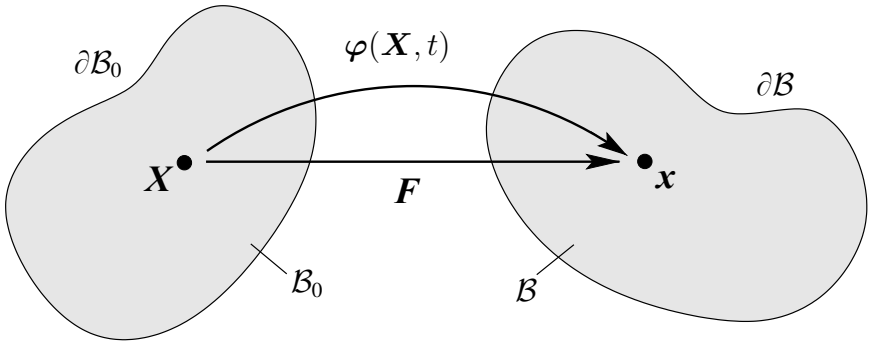

Figure 2.1: Mathematical description of the motion of a body $\mathcal{B}$ in $\mathcal{R}$.

These balance laws and proposed constitutive relations for amorphous glassy polymers will be introduced comprehensively in Section 2.2 and 3.4, respectively.

2.1.1 Kinematics

Let $\mathcal{B}_0$ represent a continuum body containing point $\mathcal{P}$ at a given instant t_0. Then, one can introduce a right-handed reference frame with rectangular coordinate system having an origin at $\mathcal{O}$. This coordinate system is spanned by orthonormal unit vectors $\{\boldsymbol{e}_a\} = \{\boldsymbol{e}_1, \boldsymbol{e}_2, \boldsymbol{e}_3\}$. While the continuum body $\mathcal{B}_0$ is moving in space through time, it covers arbitrary spatial regions $\mathcal{B}$ in that space. Each one-to-one mapping between these regions, or namely ***configuration***, can be denoted as $\chi_0, ..., \chi_t$. The continuous body $\mathcal{B}$ may have infinitely many configurations in the space from time to time and

every point $\mathcal{P}$ laying in $\mathcal{B}$ corresponds to another arbitrary point, namely ***position***, in these configurations $(\chi_0, ..., \chi_t)$. The configuration at time insant t_0 is represented by χ_0 and it refers to undeformed configuration or predefined reference configuration depending on the nature of the problem. The configuration at $t = 0$ is called initial configuration and since we agree that undeformed and initial configurations coincide for simplicity, χ_0 is also denoted as initial configuration. However, this may not be the case in dynamics. Position of an arbitrary point $\mathcal{P} \in \mathcal{B}$ at $t = 0$ can be identified by the position vector $\boldsymbol{X}$ with respect to fixed predefined origin $\mathcal{O}$. As the continuum body moves in space from initial configuration to another, the position vector associated with point $\mathcal{P}$ changes and is labelled as $\boldsymbol{x}$, see (Figure 2.1). Basis vectors of position vectors $\boldsymbol{X}$ and $\boldsymbol{x}$ are denoted as $\boldsymbol{E}_i$ and $\boldsymbol{e}_i$ respectively.

$$\boldsymbol{x} = \chi_t(\mathcal{P}) = \chi_t {\chi_0}^{-1}(\boldsymbol{X}) = \chi_t \circ \chi_0^{-1}(\boldsymbol{X}) =: \boldsymbol{\varphi}_t(\boldsymbol{X}),$$

$$\boldsymbol{\varphi} = \begin{cases} \mathcal{B}_0 \longrightarrow \mathcal{B} \in \mathcal{R}^3 \\ \boldsymbol{X} \longmapsto \boldsymbol{x} = \boldsymbol{\varphi}(\boldsymbol{X}, t) \end{cases} \tag{2.1}$$

The motion of the body $\mathcal{B}_0$ can be defined by a mapping $\boldsymbol{\varphi}$. Since the deformation map is one-to-one, it's inverse can be denoted by $\boldsymbol{X} = \boldsymbol{\varphi}^{-1}(\boldsymbol{x}, t)$, uniquely. For simplicity, we follow Einstein's summation convention, where can be expressed $\boldsymbol{A} = A_{ij..k}\boldsymbol{e}_i \otimes \boldsymbol{e}_j \otimes ... \otimes \boldsymbol{e}_k$. The symbol $\otimes$ refers to the dyadic product with orthonormal base vectors $\boldsymbol{e_a}$ and all subscripts $(i, j, ..., k)$ take values from set $\{1, 2, 3\}$.

In the light of these, one can delineate the definiton of displacement

$$\boldsymbol{U}(\boldsymbol{X}, t) = \boldsymbol{x}(\boldsymbol{X}, t) - \boldsymbol{X} \quad \text{and} \quad \boldsymbol{u}(\boldsymbol{x}, t) = \boldsymbol{x} - \boldsymbol{X}(\boldsymbol{x}, t) \tag{2.2}$$

Derivative of the deformation map with respect to time gives velocity

$$\boldsymbol{V}(\boldsymbol{X}, t) = \frac{\partial}{\partial t}\boldsymbol{\varphi}(\boldsymbol{X}, t) \quad \text{and} \quad \boldsymbol{v}(\boldsymbol{x}, t) = \boldsymbol{V}[\boldsymbol{\varphi}^{-1}(\boldsymbol{x}, t), t] \tag{2.3}$$

Then, second derivative of the deformation map refers to acceleration clearly

$$\boldsymbol{A}(\boldsymbol{X}, t) = \frac{\partial^2 \boldsymbol{\varphi}}{\partial t^2} \quad \text{and} \quad \boldsymbol{a}(\boldsymbol{x}, t) = \boldsymbol{A}[\boldsymbol{\varphi}^{-1}(\boldsymbol{x}, t), t] \tag{2.4}$$

Uppercase letters for tensorial quantities means that these quantities are in reference*(material)* coordinates. On the other hand, any tensorial quantity in current*(spatial)*

coordinates is denoted by lowercase letters.

Deformation gradient, line, area and volume mapping:

One of the primary objectives of mechanics is to study the deformation (i.e., changes in size and shape) of a continuum body as it transitions from one configuration to another. To capture this deformation, a fundamental measure is defined to relate two configurations. In the context of a continuum body's motion, the local deformation at any point along a trajectory is represented by a tangent vector. These infinitesimal vector elements in the reference (undeformed) and current (deformed) configurations are known as material and spatial line elements, respectively. The deformation gradient, denoted by $\boldsymbol{F}$, provides a mapping between these elements as described by the equation:

$$d\boldsymbol{x} = \boldsymbol{F}(\boldsymbol{X}, t)d\boldsymbol{X} \quad \text{or} \quad dx_a = F_{aA}dX_A \tag{2.5}$$

where the deformation gradient is defined as:

$$\boldsymbol{F}(\boldsymbol{X}, t) = \frac{\partial \varphi_t(\boldsymbol{X}, t)}{\partial \boldsymbol{X}}. \tag{2.6}$$

The deformation gradient plays a crucial role in parameterizing the trajectories of particles $\mathcal{P} \in \mathcal{B}$, providing a detailed description of deformation (see HAUPT [54] and HOLZAPFEL [57]). In Figure 2.2, three fundamental maps of a continuum are illustrated: (a) The deformation gradient $\boldsymbol{F}$ as a mapping of an infinitesimal line element, (b) its cofactor cof$[\boldsymbol{F}]$ as an area map, and (c) its determinant det$[\boldsymbol{F}]$ as a volume map. In addition to the line element $d\boldsymbol{X}$, the infinitesimal area and volume elements in the reference configuration are denoted by $d\boldsymbol{A}$ and dV, respectively (see Figure 2.2). The deformation of these elements is characterized by deformation gradient-based quantities, such as the cofactor cof$[\boldsymbol{F}] = \text{det}[\boldsymbol{F}]\boldsymbol{F}^{-T}$ and the Jacobian $J = \text{det}[\boldsymbol{F}] > 0$:

$$d\boldsymbol{a} = \text{cof}\boldsymbol{F}d\boldsymbol{A} \quad \text{and} \quad dv = JdV. \tag{2.7}$$

Here, $J(\boldsymbol{X}, t)$ represents the determinant of the deformation gradient $\boldsymbol{F}$. Since the material is impenetrable, meaning that the volume cannot become negative, a con-

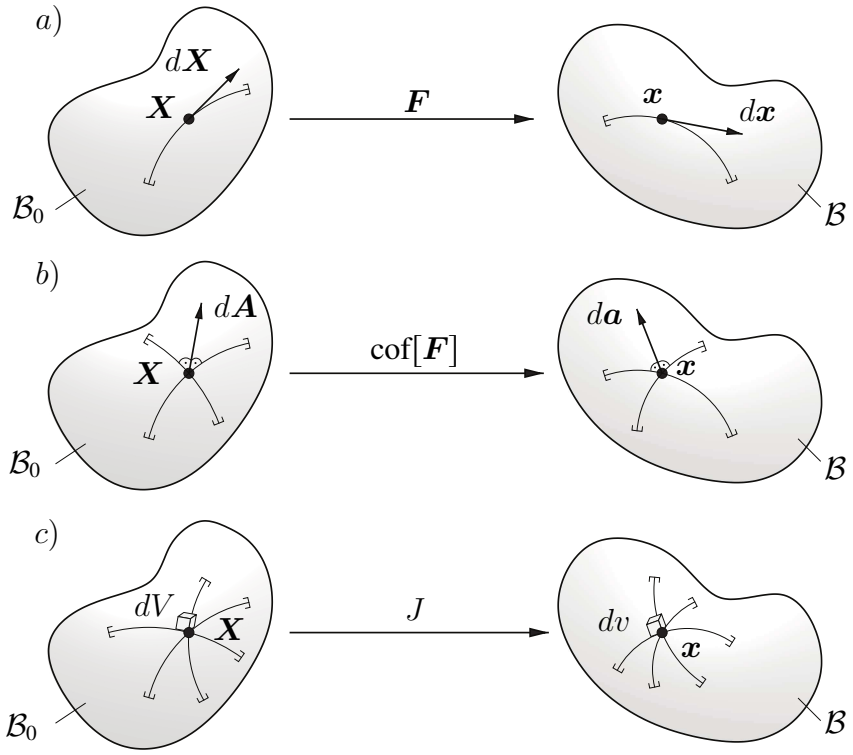

Figure 2.2: Three fundamental maps of a continuum: (a) The deformation gradient$\boldsymbol{F}$ as a mapping of a tiny line element, (b) its cofactor cof$[\boldsymbol{F}]$ as an area map, and (c) and its determinant det$[\boldsymbol{F}]$as a volume map.

dition where $J(\boldsymbol{X}, t) < 0$ is physically impossible. Furthermore, the deformation gradient is invertible, so $J(\boldsymbol{X}, t) \neq 0$.

The deformation process maps the unit tangent vector, $\boldsymbol{T}$, from the reference or Lagrangian configuration to its corresponding counterpart, $\boldsymbol{t}$, in the current Eulerian configuration, as illustrated in Figure 2.3.

Push-forward and Pull-back Operations:

If different reference frames are used for the reference and current configurations, vector and tensor quantities can be resolved in either frame depending on the analysis choice. The transformation between material and spatial coordinates is accomplished through push-forward and pull-back operations, allowing for the conversion of quantities between the two coordinate systems. These operations enable the analysis of the body's deformation and motion in a way that aligns with our analytical needs.

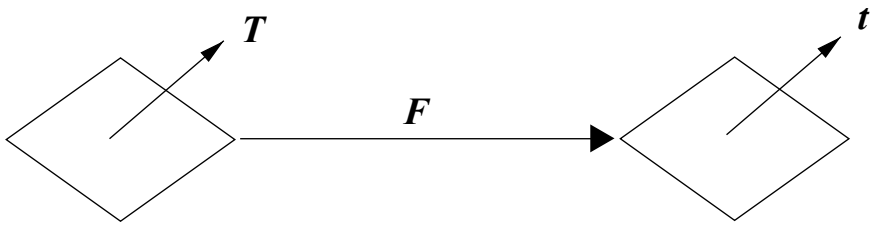

Figure 2.3: Deformation gradient mapping.

$$\begin{aligned} \boldsymbol{t} &= \boldsymbol{F}\boldsymbol{T} \text{ : push-forward of } \boldsymbol{T}, \\ \boldsymbol{T} &= \boldsymbol{F}^{-1}\boldsymbol{t} \text{ : pull-back of } \boldsymbol{t}. \end{aligned} \tag{2.8}$$

Deformation and Strain Measures:

The mapping of a unit vector $\boldsymbol{A}$ in the reference configuration to a vector $\boldsymbol{a}$ in the current configuration is defined as:

$$\boldsymbol{a} = \boldsymbol{F}\boldsymbol{A}. \tag{2.9}$$

According to this definition, the stretch (λ) of the vector $\boldsymbol{A}$ due to deformation is given by $\lambda = |\boldsymbol{a}|$. To further examine the extent of the stretch, we consider the square of the stretch:

$$\lambda^2 = \boldsymbol{a} \cdot \boldsymbol{a} = \boldsymbol{F}\boldsymbol{A} \cdot \boldsymbol{F}\boldsymbol{A} = \boldsymbol{A}\boldsymbol{F}^T \cdot \boldsymbol{F}\boldsymbol{A} = \boldsymbol{A} \cdot \boldsymbol{C}\boldsymbol{A}, \tag{2.10}$$

where $\boldsymbol{C} = \boldsymbol{F}^T\boldsymbol{F}$.

The tensor $\boldsymbol{C}$, derived from λ^2, is a commonly used measure of deformation in material coordinates. It is a second-order symmetric positive definite tensor and is often called the *right Cauchy-Green tensor* in material coordinates. Its spatial counterpart, denoted as $\boldsymbol{b}$, is known as the *Finger tensor* or the *left Cauchy-Green tensor*. The Finger tensor is derived from the definition of λ^{-2} as the square of the inverse stretch:

$$\lambda^{-2} = \boldsymbol{A} \cdot \boldsymbol{A} = \boldsymbol{F}^{-1}\boldsymbol{a} \cdot \boldsymbol{F}^{-1}\boldsymbol{a} = \boldsymbol{a}\boldsymbol{F}^{-T} \cdot \boldsymbol{F}^{-1}\boldsymbol{a} = \boldsymbol{a} \cdot \boldsymbol{b}^{-1}\boldsymbol{a}. \tag{2.11}$$

The tensor $\boldsymbol{b} = \boldsymbol{F}\boldsymbol{F}^T$ is also symmetric and positive definite. In the absence of deformation, $\boldsymbol{F}$ equals the identity tensor $\boldsymbol{I}$, and therefore $\boldsymbol{b}$ and $\boldsymbol{C}$ also equal $\boldsymbol{I}$. The

identity tensor $\boldsymbol{I}$ is defined as $\delta_{ij}\boldsymbol{e}_i \otimes \boldsymbol{e}_j$, where δ_{ij} is the Kronecker delta, equal to 1 for $i = j$ and $\delta_{ij} = 0$ for $i \neq j$.

The polar decomposition of the deformation gradient $\boldsymbol{F}$ can be expressed as:

$$\boldsymbol{F} = \boldsymbol{R}\boldsymbol{U} = \boldsymbol{v}\boldsymbol{R}. \tag{2.12}$$

This decomposition allows us to separate $\boldsymbol{F}$ into two components: pure rotation($\boldsymbol{R}$) and pure stretch($\boldsymbol{U}$ and/or $\boldsymbol{v}$).

The right-stretch tensor $\boldsymbol{U}$ and the left-stretch tensor $\boldsymbol{v}$ satisfy the properties:

$$\boldsymbol{U}^2 = \boldsymbol{U}\boldsymbol{U} = \boldsymbol{C} \quad \text{and} \quad \boldsymbol{v}^2 = \boldsymbol{v}\boldsymbol{v} = \boldsymbol{b}. \tag{2.13}$$

These tensors describe the stretch and deformation behavior of the material. The tensor $\boldsymbol{R}$ is a proper orthogonal tensor with det$\boldsymbol{R} = 1$, representing a valid rotation. Additionally, det$\boldsymbol{U} =$ det$\boldsymbol{v} = J > 0$.

The right-stretch tensor $\boldsymbol{U}$ has a relationship given by:

$$\boldsymbol{U}\boldsymbol{N_a} = \lambda_a \boldsymbol{N_a}, \text{where} \quad |\boldsymbol{N_a}| = 1, \text{and} \quad a = 1, 2, 3. \tag{2.14}$$

The set $\{\boldsymbol{N_a}\}$ represents the eigenvectors of $\boldsymbol{U}$, while λ_a corresponds to the eigenvalues. From Equation (2.17), we can deduce that:

$$\boldsymbol{C}\boldsymbol{N_a} = \boldsymbol{U}^2\boldsymbol{N_a} = \lambda_a^2 \boldsymbol{N_a}, a = 1, 2, 3. \tag{2.15}$$

Since both $\boldsymbol{U}$ and $\boldsymbol{C}$ are purely Lagrangian measures, they share the same eigenvectors known as principal axes. Similarly, we can derive a comparable relationship for $\boldsymbol{b}$ using Equation (2.17):

$$\boldsymbol{b}\boldsymbol{n_a} = \boldsymbol{v}^2\boldsymbol{n_a} = \lambda_a^2 \boldsymbol{n_a}, a = 1, 2, 3. \tag{2.16}$$

The eigenvalues of $\boldsymbol{v}$ and $\boldsymbol{b}$ are also equal to λ_a and λ_a^2, respectively. Both $\boldsymbol{v}$ and $\boldsymbol{b}$ have the same set of orthonormal eigenvectors as spatial measures. In conclusion,

for a given deformation gradient $\boldsymbol{F}$, we can extract crucial information about the material's deformation and stretch by analyzing the tensors $\boldsymbol{U}$, $\boldsymbol{v}$, $\boldsymbol{C}$, and $\boldsymbol{b}$. This relationship indicates that $\boldsymbol{v}$ and $\boldsymbol{b}$ are collinear in spatial coordinates. For distinct values of λ_1, λ_2 and λ_3 the symmetric tensors $\boldsymbol{U}$, $\boldsymbol{v}$, $\boldsymbol{C}$ and $\boldsymbol{b}$ can be expressed in their spectral decomposition forms as follows

$$\begin{aligned} \boldsymbol{U}^2 = \boldsymbol{C} = \sum_{a=1}^{3} \lambda_a^2 \boldsymbol{N_a} \otimes \boldsymbol{N_a}, \\ \boldsymbol{v}^2 = \boldsymbol{b} = \sum_{a=1}^{3} \lambda_a^2 \boldsymbol{n_a} \otimes \boldsymbol{n_a}. \end{aligned} \tag{2.17}$$

Where λ_a represent the principal stretches *(eigenvalues)* and $\boldsymbol{N_a}$ and $\boldsymbol{n_a}$ denote the principal directions *(eigenvectors)* in the Lagrangian and Eulerian frameworks, respectively.

Furthermore, the deformation gradient can be represented as:

$$\boldsymbol{F} = \sum_{a=1}^{3} \lambda_a \boldsymbol{n_a} \otimes \boldsymbol{N_a}, \tag{2.18}$$

which is a two-point tensor. As $\boldsymbol{F}$ may not be symmetric, the λ_a values can not be directly considered as the eigenvalues of $\boldsymbol{F}$. Since both $\boldsymbol{C}$ and $\boldsymbol{b}$ are symmetric and positive definite, they possess three uniquely defined invariants. The scalar invariants of $\boldsymbol{C}$ can be summarized as:

$$\begin{aligned} I_1(\boldsymbol{C}) = \lambda_1^2 + \lambda_2^2 + \lambda_3^2, \\ I_2(\boldsymbol{C}) = \lambda_1^2\lambda_2^2 + \lambda_1^2\lambda_3^2 + \lambda_2^2\lambda_3^2, \\ I_3(\boldsymbol{C}) = \lambda_1^2\lambda_2^2\lambda_3^2 = J^2. \end{aligned} \tag{2.19}$$

Additionally, within a generalised coordinate system, both the reference $\mathcal{B}_0$ and the spatial $\mathcal{B}$ manifolds are equipped locally with the Lagrangian metric $\boldsymbol{G}$ and Eulerian counterpart (current metric) $\boldsymbol{g}$. These metric tensors are crucial in converting covariant and contravariant entities within the Lagrangian and Eulerian manifolds. If cartesian basis vectors are employed, metric tensors are

$$\boldsymbol{G} = \delta_{AB} \boldsymbol{E}^A \otimes \boldsymbol{E}^B \quad and \quad \boldsymbol{g} = \delta_{ab} \boldsymbol{e}^a \otimes \boldsymbol{e}^b. \tag{2.20}$$

The right Cauchy Green tensor and the inverse of the left Cauchy Green tensor can be formulated utilising these metric tensors.

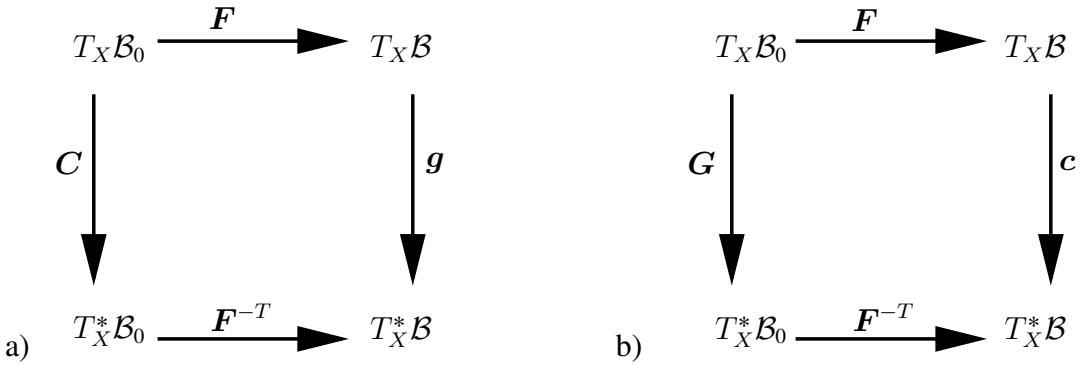

Figure 2.4: Definition of metric tensors. a) current metric in Lagrangian configuration; b) reference metric in Eulerian configuration.

The right Cauchy Green tensor and the inverse of the left Cauchy Green tensor can be expressed using metric tensors denoted as

$$\boldsymbol{C} = \boldsymbol{F}^{\boldsymbol{T}}\boldsymbol{g}\boldsymbol{F} \tag{2.21}$$

and

$$\boldsymbol{c} = \boldsymbol{F}^{-\boldsymbol{T}}\boldsymbol{G}\boldsymbol{F}^{-\boldsymbol{1}} \tag{2.22}$$

these equations correspond to the pullback of the current metric $\boldsymbol{g}$ and the push forward of the Lagrangian metric $\boldsymbol{G}$, respectively. The left Cauchy Green tensor, also known as the Finger tensor, is represented by $\boldsymbol{b} = \boldsymbol{c}^{-1}$. Please refer to Figure 2.4 for a geometric interpretation.

2.1.2 Stress expressions

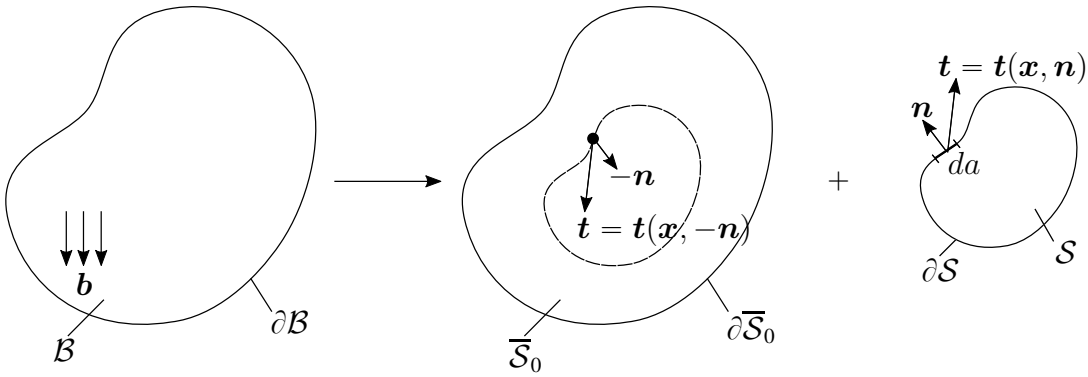

Figure 2.5: The removal of slice $\mathcal{S}$ from the body $\mathcal{B}$ depicts the tractions and normals associated with both the slice $\mathcal{S}$ and the remaining portion $\overline{\mathcal{S}}$.

Consider a body $\mathcal{B}$ with specific boundary conditions applied to $\partial\mathcal{B}$ and subjected to

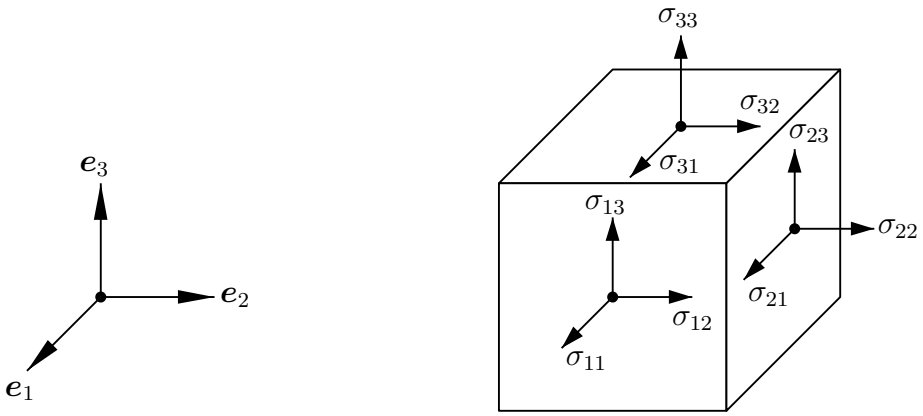

Figure 2.6: Stress components on the surfaces of unit cube.

internal boy forces. Suppose a section of the boundary, $\partial\mathcal{S}$, is isolated as shown in Figure 2.5. The isolated section, denoted as $\mathcal{S}$, is subjected to the traction force $\boldsymbol{t}$ and the body force $\boldsymbol{b}$ in its current configuration. The net forces acting on the isolated section $\mathcal{S}$ of body $\mathcal{B}$ and the remaining part $\overline{\mathcal{S}}$ are given by:

$$\boldsymbol{\mathcal{F}_1} = \int_{\mathcal{S}} \boldsymbol{b}\, dv + \int_{\partial\mathcal{S}} \boldsymbol{t}(\boldsymbol{x}, \boldsymbol{n})\, ds, \tag{2.23}$$

$$\boldsymbol{\mathcal{F}_2} = \int_{\overline{\mathcal{S}}} \boldsymbol{b}\, dv + \int_{\partial\overline{\mathcal{S}}} \boldsymbol{t}(\boldsymbol{x}, -\boldsymbol{n})\, ds. \tag{2.24}$$

$\boldsymbol{\mathcal{F}} = \boldsymbol{\mathcal{F}_1} + \boldsymbol{\mathcal{F}_2}$ is the total net force applied on the body. Notice that the integration of the body forces over the entire body, expressed as $\int_{\mathcal{B}} \boldsymbol{b}\, dv$, is the sum of the integrations over the slice $\int_{\mathcal{S}} \boldsymbol{b}\, dv$ and its complement $(\int_{\overline{\mathcal{S}}} \boldsymbol{b}\, dv)$. These expressions lead to important equality:

$$\int_{\partial\mathcal{S}} \boldsymbol{t}(\boldsymbol{x}, \boldsymbol{n})\, ds + \int_{\partial\overline{\mathcal{S}}} \boldsymbol{t}(\boldsymbol{x}, -\boldsymbol{n})\, ds \tag{2.25}$$

which can be locally simplified to:

$$\boldsymbol{t}(\boldsymbol{x}, \boldsymbol{n}) = -\boldsymbol{t}(\boldsymbol{x}, -\boldsymbol{n}) \tag{2.26}$$

This relationship is known as Cauchy's fundamental lemma. It reflects Newton's third law of motion, stating that when two surfaces are in contact, they will exert equal magnitude of force in opposite directions to each other.

$$\begin{aligned} \boldsymbol{t}_1 &= \sigma_{11}\boldsymbol{e}_1 + \sigma_{12}\boldsymbol{e}_2 + \sigma_{13}\boldsymbol{e}_3 \\ \boldsymbol{t}_2 &= \sigma_{21}\boldsymbol{e}_1 + \sigma_{22}\boldsymbol{e}_2 + \sigma_{23}\boldsymbol{e}_3 \\ \boldsymbol{t}_3 &= \sigma_{31}\boldsymbol{e}_1 + \sigma_{32}\boldsymbol{e}_2 + \sigma_{33}\boldsymbol{e}_3 \end{aligned} \tag{2.27}$$

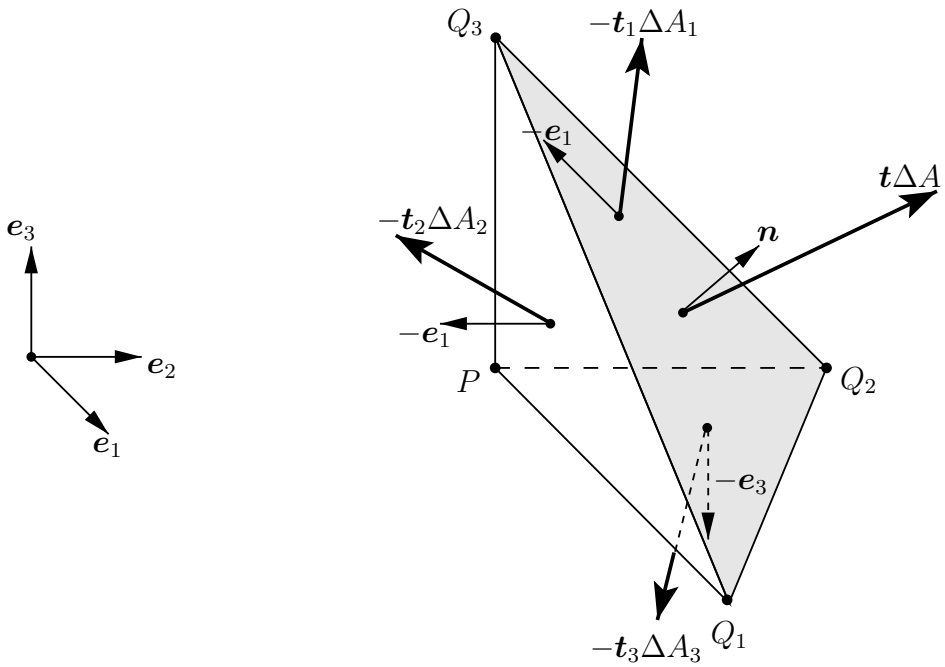

Figure 2.7: Traction components on triangular section taken from the unit cube.

In a more compact form, Equation (2.27) can be rewritten as:

$$\boldsymbol{t}_i = \sigma_{ij}\boldsymbol{e}_j \quad or \quad \sigma_{ij} = \boldsymbol{t}_j \cdot \boldsymbol{e}_j \tag{2.28}$$

Next, consider a section of a unit cube (Figure 2.6) visualized as a tetrahedron (Figure 2.7). The force equilibrium from the free body diagram is

$$\boldsymbol{t}\Delta A - \boldsymbol{t}_1\Delta A_1 - \boldsymbol{t}_2\Delta A_2 - \boldsymbol{t}_3\Delta A_3 = 0. \tag{2.29}$$

$$n_1 = \frac{\Delta A_1}{\Delta A} \quad n_2 = \frac{\Delta A_2}{\Delta A} \quad n_3 = \frac{\Delta A_3}{\Delta A} \tag{2.30}$$

Substituting surface normal components in Equaiton (2.30) into Equaiton (2.29) leads to

$$[\boldsymbol{t} - \boldsymbol{t}_1 n_1 - \boldsymbol{t}_2 n_2 - \boldsymbol{t}_3 n_3]\Delta A = 0 \tag{2.31}$$

or in a compact form

$$\begin{aligned} \boldsymbol{t} = \boldsymbol{t}_i n_i \quad &\text{from Equation (2.28)} \\ \boldsymbol{t} = n_i\sigma_{ij}\boldsymbol{e}_j = t_j\boldsymbol{e}_j \end{aligned} \tag{2.32}$$

leading to

$$t_j = n_i\sigma_{ij} \quad or \quad \boldsymbol{t} = \boldsymbol{\sigma}\boldsymbol{n} \tag{2.33}$$

This is known as *Cauchy's stress theorem*, $\sigma = F(t)/A(t)$ where σ is Cauchy stress, $F(t)$ is actual force and $A(t)$ is actual area. The Cauchy stress vector, $\boldsymbol{t}(\boldsymbol{x}, t, \boldsymbol{n})$ calculates the stress relative to the deformed area, which is called the true stress. If we define the first Piola-Kirchoff stress vector $\boldsymbol{T}(\boldsymbol{X}, t, \boldsymbol{N})$ parallel to $\boldsymbol{t}(\boldsymbol{x}, t, \boldsymbol{n})$ and calculate the first Piola-Kirchoff stress with this vector using the undeformed area, this stress is engineering stress.

$$\begin{aligned} \boldsymbol{P} d\boldsymbol{A} &= \boldsymbol{\sigma} d\boldsymbol{a}, \\ \boldsymbol{P} = J\boldsymbol{\sigma}\boldsymbol{F}^{-T} &= \boldsymbol{\tau}\boldsymbol{F}^{-T}, \\ \boldsymbol{\tau} &= J\boldsymbol{\sigma} \\ \boldsymbol{S} = \boldsymbol{F}^{-1}\boldsymbol{P} &= \boldsymbol{F}^{-1}\boldsymbol{\tau}\boldsymbol{F}^{-T}, \end{aligned} \tag{2.34}$$

where $\boldsymbol{P}$ is the first Piola-Kirchhoff stress, $\boldsymbol{\tau}$ is the Kirchhoff stress and $\boldsymbol{S}$ is the second Piola-Kirchhoff stress tensors (Figure 2.8). The semi-pull-back of the first Piola-Kirchhoff stress gives rise to the symmetric second Piola-Kirchhoff stress ($\boldsymbol{S}$), which serves as an important alternative stress measure.

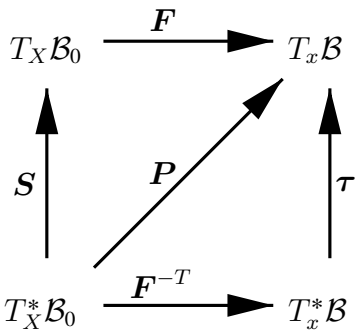

Figure 2.8: Relationship between stresses.

In Figure 2.8, $T_X\mathcal{B}_0$ and $T_x\mathcal{B}$ refer to tangent spaces in reference and current configurations respectively while $T_X^*\mathcal{B}_0$ and $T_x^*\mathcal{B}$ correspond to co-tangent space in those configurations.

2.2 Balance Laws

Balance laws are fundamental principals in continuum mechanics that explain the conservation of physical quantities within a system. These laws are obtained from governing differential equations and are cruical for describing the material behaviour

under arbitrary physical conditions. Under following subsections, each law will be discussed, briefly. All derivations are done for a unit volume of current configuration.

2.2.1 Conservation of Mass

The total mass in a closed system is neither created or destroyed within a system so that it is constant under action of any motion.

$$\boxed{m = \int_{\mathcal{B}} \rho d\upsilon = \int_{\mathcal{B}_0} \rho_0 dV = constant \quad \Rightarrow \quad \frac{dm}{dt} = 0} \tag{2.35}$$

The continuity equation which describes local conservation of mass at any point in a continuum is shown as

$$\boxed{\frac{d\rho}{dt} + \rho \operatorname{div} \boldsymbol{v} = 0}, \tag{2.36}$$

where ρ, ρ_0 and $\boldsymbol{v}$ are the current density, reference density and the spatial velocity, respectively.

2.2.2 Conservation of Momentum

The change in the momentum of a body over time is equal to the sum of the forces acting on the body. Thus, conservation of momentum is expressed as

$$\boxed{\frac{d}{dt}\int_{\mathcal{B}} \rho \boldsymbol{v} d\upsilon = \int_{\mathcal{B}} \rho \boldsymbol{b} d\upsilon + \int_{\partial\mathcal{B}} \boldsymbol{t} dA}. \tag{2.37}$$

The Cauchy's theorem states that

$$\boxed{\boldsymbol{t} = \boldsymbol{\sigma}\boldsymbol{n}}, \tag{2.38}$$

where $\boldsymbol{b}$ is the body forces acting on unit deformed volume, $\boldsymbol{t}$ is the surface traction vector applied on unit deformed area and $\boldsymbol{\sigma}$ is the Cauchy stress tensor. Combining equations (2.36) and (2.37), expression for the local form of the momentum balance is obtained

$$\boxed{\rho \dot{\boldsymbol{v}} = \operatorname{div} \boldsymbol{\sigma} + \rho \boldsymbol{b}}. \tag{2.39}$$

2.2.3 Conservation of Moment of Momentum

The conservation of angular momentum states that changes in the angular momemntum is balanced by the net moment acting on the body. Local form of balance of

angular momentum ensures that the Cauchy stress is symmetric

$$\boxed{\boldsymbol{\sigma} = \boldsymbol{\sigma}^T}. \tag{2.40}$$

As a result, following equities hold

$$\boxed{\boldsymbol{\tau} = \boldsymbol{\tau}^T, \quad \boldsymbol{P}\boldsymbol{F}^T = \boldsymbol{F}\boldsymbol{P}^T, \quad \boldsymbol{S} = \boldsymbol{S}^T} \tag{2.41}$$

for the Kirchhoff stress tensor, the First Piola-Kirchhoff stress tensor and the second Piola-Kirchhoff stress tensor, respectively.

2.2.4 Conservation of Energy: First Axiom of Thermodynamics

The energy conservation or namely first axiom of thermodynamics is an expression of the interconvertibility of heat and work in a system and can be expressed as

$$\boxed{\frac{d}{dt}\int_{\mathcal{B}} \rho(e + \frac{1}{2}\boldsymbol{v}\cdot\boldsymbol{v})d\upsilon = \int_{\mathcal{B}} \rho(\boldsymbol{b}\cdot\boldsymbol{v} + r)d\upsilon + \int_{\mathcal{B}} (\boldsymbol{t}\cdot\boldsymbol{v} - h)da} \tag{2.42}$$

In the above equation, e is the mass specific internal energy, r is the heat source generated by internal processes in the body and h is the outwards heat flux. The global expression of the internal energy balance can be shown as

$$\frac{d}{dt}(\mathcal{K} + \mathcal{E}) = \mathcal{P} + \mathcal{Q}, \tag{2.43}$$

where $\mathcal{K}$, $\mathcal{E}$, $\mathcal{P}$ and $\mathcal{Q}$ are the kinetic energy, the internal energy, the mechanical power and non-mechanical power, respectively. It states that the rate of change of the total kinetic and internal energy equals to the sum of mechanical and non–mechanical power in a closed system. The specific forms of each component in equation (2.43) can be defined as,

$$\begin{aligned}
\mathcal{K} &:= \int_{\mathcal{B}} \frac{1}{2}\rho\boldsymbol{v}\cdot\boldsymbol{v}d\upsilon, \\
\mathcal{E} &:= \int_{\mathcal{B}} \rho e d\upsilon, \\
\mathcal{P} &:= \int_{\mathcal{B}} \rho\boldsymbol{b}\cdot\boldsymbol{v}d\upsilon + \int_{\partial\mathcal{B}} \boldsymbol{t}\cdot\boldsymbol{v}da, \\
\mathcal{Q} &:= \int_{\mathcal{B}} \rho r d\upsilon - \int_{\partial\mathcal{B}} h da.
\end{aligned} \tag{2.44}$$

Considering all the spesific form of balance equations given above, final form of the balance of internal energy is written as

$$\boxed{\rho\dot{e} + \operatorname{div}\boldsymbol{q} = \boldsymbol{\sigma} : \boldsymbol{d} + \rho r}, \tag{2.45}$$

where $\boldsymbol{d} := \operatorname{sym}[\boldsymbol{gl}]$ is the symmmetric part of the spatial velocity gradient $\boldsymbol{l} := \dot{\boldsymbol{F}}\boldsymbol{F}^{-1}$.

2.2.5 Clausius-Duhem Inequality: Second Axiom of Thermodynamics

The second law of thermodynamics imposes limitations on the constitutive relations governing both elastic and inelastic dissipative mechanisms in mechanical processes, as well as on the direction of heat flow in thermal processes.
The Clausius-Duhem inequality is denoted as

$$\frac{d}{dt}\int_{\mathcal{B}} \rho\eta d\upsilon \geqslant \int_{\mathcal{B}} \frac{\rho r}{\theta} d\upsilon - \int_{\partial\mathcal{B}} \frac{h}{\theta} da \tag{2.46}$$

where η and θ correspond to entrophy per volume and absolute temperature , respectively. It simply implies that rate of entropy increase must be greater than the entropy input rate. Using the Gauss integral theorems and the Cauchy law ($h = \boldsymbol{q} \cdot \boldsymbol{n}$) yields final form of

$$\boxed{\rho\dot{\eta} \geqslant \frac{\rho r}{\theta} - \operatorname{div}(\frac{\boldsymbol{q}}{\theta}) = \frac{\rho r}{\theta} - \frac{1}{\theta}\operatorname{div}\boldsymbol{q} + \frac{1}{\theta^2}\boldsymbol{q} \cdot \nabla_x\theta}. \tag{2.47}$$

2.3 Dissipation Inequality: Coleman's Method

The constitutive relations are constructed in a way that inherently satisfies the second law of thermodynamics so that these relations are thermodynamically consistent. In other saying, the Clausius-Duhem Inequality (CDI) given in equation (2.47) imposes a restriction on the constitutive relations. Considering the local form of global balance of energy equation (2.45) in CDI, we get,

$$\rho\gamma = \rho\dot{\eta} - \frac{1}{\theta}(\rho\dot{e} - \boldsymbol{\sigma} : \boldsymbol{d}) - \frac{1}{\theta^2}\boldsymbol{q} \cdot \nabla_x\theta \geqslant 0 \tag{2.48}$$

where γ entrophy production per volume. Modified form of CDI express the dissipation at an arbitrary material point as follows

$$\mathcal{D} := \theta\gamma = \dot{\eta} - (\dot{e} - \frac{1}{\rho}\boldsymbol{\sigma} : \boldsymbol{d}) - \frac{1}{\rho\theta}\boldsymbol{q} \cdot \nabla_x\theta \geqslant 0 \tag{2.49}$$

The dissipation terms is divided into two components: local and conductive parts, both of which are greater than zero

$$\mathcal{D} = \mathcal{D}_{loc} + \mathcal{D}_{con} \geqslant 0, \tag{2.50}$$

where

$$\rho\mathcal{D}_{loc} := \boldsymbol{\sigma} : \boldsymbol{d} - \rho\dot{e} + \rho\theta\dot{\eta} \geqslant 0 \tag{2.51}$$

and

$$\rho\mathcal{D}_{con} := -\frac{1}{\theta}\boldsymbol{q} \cdot \nabla_x\theta \geqslant 0. \tag{2.52}$$

The stronger conditions mentioned in equations (2.51) and (2.52) are referred as the Clausius-Planck Inequality (CPI) and the Fourier Inequality (FI), respectively.
Helmholtz free energy is oftenly used rather than internal energy e in solid mechanics. By using the Legendre transformation, the Helmholtz free energy can be defined as

$$\Psi := e - \theta\eta. \tag{2.53}$$

The derivative of the internal energy with respect to time in CPI can be rewritten as

$$\dot{e} = \dot{\Psi} + \eta\dot{\theta} + \theta\dot{\eta}. \tag{2.54}$$

then plugging into equation (2.51) yields

$$\rho\mathcal{D}_{loc} := \boldsymbol{\sigma} : \boldsymbol{d} - \rho\dot{\Psi} - \rho\eta\dot{\theta} \geqslant 0, \tag{2.55}$$

an alternative form for the CPI. The equations (2.52) and (2.55) fulfill the fundamental thermodynamic restriction on constitutive equations.
The Helmholtz free energy function and the heat flux are stated for general formulation of inelasticity problem as follows

$$\Psi = \hat{\Psi}(\boldsymbol{X}, \boldsymbol{F}, \theta, \boldsymbol{\mathcal{I}}, \boldsymbol{g}) \quad \boldsymbol{q} = \hat{\boldsymbol{q}}(\boldsymbol{X}, \theta, \boldsymbol{F}, \boldsymbol{g}) \tag{2.56}$$

where $\boldsymbol{\mathcal{I}}$ is the generalized internal variables vector and $\boldsymbol{g}$ is the temperature gradient. Then, time derivative of the Helmholtz free energy function turns out

$$\dot{\Psi} = \partial_{\boldsymbol{F}}\Psi : \dot{\boldsymbol{F}} + \partial_\theta\Psi\dot{\theta} + \partial_{\boldsymbol{\mathcal{I}}}\Psi : \dot{\boldsymbol{\mathcal{I}}} + \partial_{\boldsymbol{g}}\Psi \cdot \dot{\boldsymbol{g}}. \tag{2.57}$$

Substituting obtained derivative into equation (2.55) with alternative expression of stress power $\boldsymbol{\sigma} : \boldsymbol{d}$ (2.58)

$$\boldsymbol{\sigma} : \boldsymbol{d} = \boldsymbol{\sigma} : \boldsymbol{l} = J^{-1}\boldsymbol{P} : \dot{\boldsymbol{F}} = J^{-1}\boldsymbol{S} : \frac{1}{2}\dot{\boldsymbol{C}} = J^{-1}\boldsymbol{\tau} : \boldsymbol{d} \tag{2.58}$$

results in

$$[J^{-1}\boldsymbol{P} - \rho\partial_{\boldsymbol{F}}\Psi] : \dot{\boldsymbol{F}} - \rho[\eta + \partial_\theta\Psi]\dot{\theta} - \rho[\partial_{\boldsymbol{\mathcal{I}}}\Psi] : \dot{\boldsymbol{\mathcal{I}}} - \rho[\partial_{\boldsymbol{g}}\Psi] \cdot \dot{\boldsymbol{g}} \geqslant 0 \tag{2.59}$$

The equality of equation (2.59) must be satisfied for any arbitrary rates of deformation, temperature and temperature gradient. Hence, Coleman's explotation method implies

$$[\boldsymbol{P} - \rho_0\partial_{\boldsymbol{F}}\Psi] = \boldsymbol{0}, [\eta + \partial_\theta\Psi] = 0, [\partial_{\boldsymbol{g}}\Psi] = \boldsymbol{0}. \tag{2.60}$$

It is clearly shown that the Helmholtz free energy is not a function of temperature gradient beside it behaves as a potential for the stress and the entropy with following relations

$$\boldsymbol{P} = \rho_0\partial_{\boldsymbol{F}}\Psi \quad \text{and} \quad \eta = -\partial_\theta\Psi \tag{2.61}$$

Finally, local dissipation can be expressed

$$\rho\mathcal{D}_{loc} := -\rho[\partial_{\boldsymbol{\mathcal{I}}}\Psi] : \dot{\boldsymbol{\mathcal{I}}} = J^{-1}\boldsymbol{\beta} : \dot{\boldsymbol{\mathcal{I}}} \geqslant 0, \tag{2.62}$$

where $\boldsymbol{\beta} = -\rho_0\partial_{\boldsymbol{\mathcal{I}}}\Psi$ stands for thermodynamical force conjugate to any internal variables, $\boldsymbol{\mathcal{I}}$,of viscoplasticty or damage mechanism.

CHAPTER 3

A PHASE-FIELD APPROACH FOR DUCTILE-BRITTLE FAILURE OF AMORPHOUS GLASSY POLYMERS

This chapter will examine a proposed phase field approach for ductile-brittle failure of amorphous glassy polymers. First, we will investigate kinematics and thermodynamical restriction underlying inelastic formulation of proposed approach. Then, evolution equations stemming shear yielding and crazing which induce the evolution of void volume fraction will be outlined. Hereafter, global form of multi-physic problem is concerned regarding balance and non-local evolution equations describing deformation, crack phase-field and thermal field. Later, we will introduce specific forms of the constitutive relations governing the finite thermoviscoplasticity of amorphous glassy polymers and the novel failure criterion which demonstrate the ductile and brittle failure simultaneously.

3.1 Kinematics and Thermodynamics

3.1.1 Kinematics

Let $\mathcal{B}$ and $\mathcal{S} \subset \mathcal{R}^3$ be the Lagrangian (reference) and the Eulerian (spatial) configuration of a continuous body at specific time t_0 and $t \in \mathcal{T} \subset \mathcal{R}_+$, respectively. Then, the nonlinear one-to-one deformation mapping $\boldsymbol{\varphi}(\boldsymbol{X}, t)$ can be defined as follows

$$\boldsymbol{\varphi}_t(\boldsymbol{X}) : \begin{cases} \mathcal{B} \times \mathcal{T} & \rightarrow & \mathcal{S} \in \mathcal{R}^3 \\ (\boldsymbol{X}, t) & \mapsto & \boldsymbol{x} = \boldsymbol{\varphi}(\boldsymbol{X}, t) \end{cases} , \tag{3.1}$$

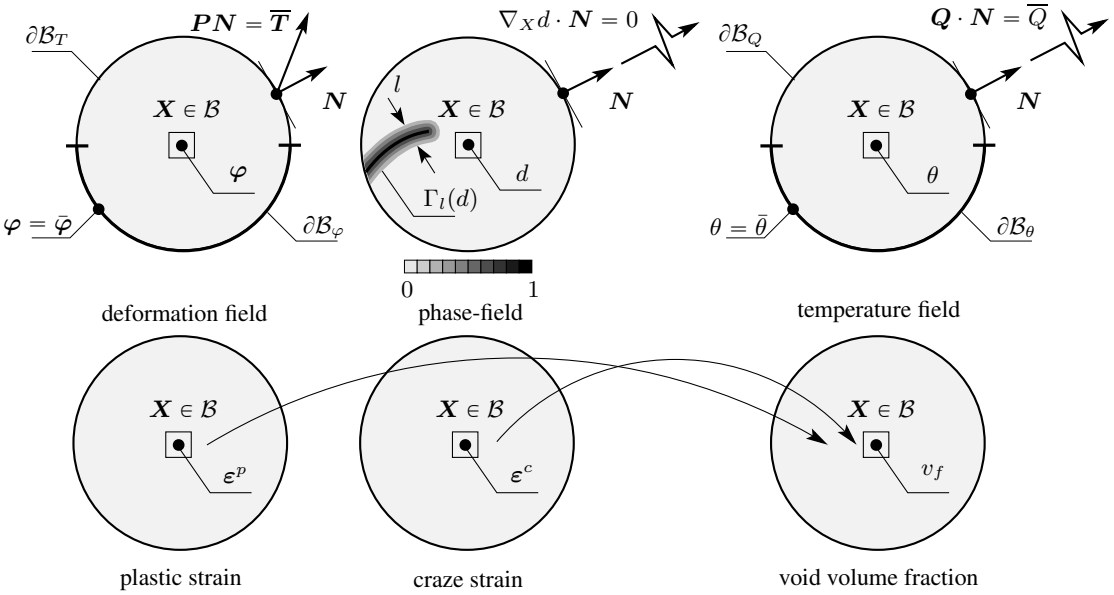

Figure 3.1: Primary and local field variables constituting the multi-physics of ductile and brittle fracture in the reference frame; deformation map $\boldsymbol{\varphi}$ along with Dirichlet and Neumann-type boundary conditions

The deformation map projects the reference configuration onto its counterpart in the spatial configuration, see Fig. 3.1. Additionaly, the crack phase-field variable, d, reads

$$d : \begin{cases} \mathcal{B} \times \mathcal{T} \to [0,1] \\ (\boldsymbol{X}, t) \mapsto d(\boldsymbol{X}, t) \end{cases} . \tag{3.2}$$

While phase field parameter is $d = 0$, material is intact. On the other hand, material can be said in fully ruptured state when $d = 1$. Therefore, phase field variable lies in interval of $[0, 1]$. As mentioned in previous chapter, deformation map $\boldsymbol{\varphi}_t(\boldsymbol{X})$ at a fixed time t, the deformation gradient and its determinant are defined as

$$\boldsymbol{F} := \nabla_{\boldsymbol{X}} \boldsymbol{\varphi}_t(\boldsymbol{X}) \quad \text{and} \quad J := \det(\boldsymbol{F}) > 0 \,. \tag{3.3}$$

Afterwards, we describe the temperature field in the finite strain context

$$\theta : \begin{cases} \mathcal{B} \times \mathcal{T} \to \mathcal{R}^1_+ \\ (\boldsymbol{X}, t) \mapsto \theta(\boldsymbol{X}, t) \end{cases} , \tag{3.4}$$

as shown in Fig. 3.1

In mathematical saying, the deformation gradient is a basic nonlinear bijective mapping which construct a relation between tangent vectors of material curves and tangent vectors of the deformed curves. The gradient operator $\nabla_{\boldsymbol{X}}(\bullet)$ and the Jacobian

J in (3.3) denote the spatial derivative with respect to the reference $\boldsymbol{X}$ and linear transformation between an infinitesimal reference volume and associated spatial one, respectively. As we move further, consider the reference $\mathcal{B}$ and the spatial $\mathcal{S}$ manifolds with the covariant reference $\boldsymbol{G}$ and spatial $\boldsymbol{g}$ metric tensors. These metric tensors are identical to Kronecker delta, i.e. $g_{ab} = \delta_{ab}$ and $G_{AB} = \delta_{AB}$, in Cartesian coordinates system. Then, the right Cauchy Green tensor can be defined as

$$\boldsymbol{C} := \boldsymbol{F}^T \boldsymbol{g} \boldsymbol{F} \qquad \text{where} \qquad C_{AB} = F^a{}_A g_{ab} F^b{}_B, \tag{3.5}$$

in the reference configuration. Beyond the aforementioned primary deformation variables of mechanics, any inelastic response is history dependent and is hence incorporated through internal variables evolving over time. For the problem of interest, these internal variables are the covariant Lagrangian inelastic metrics $\boldsymbol{G}^p$ and $\boldsymbol{G}^c$ which are related to shear yielding and crazing, respectively. These metrics are defined as follows

$$\boldsymbol{G}^p : \begin{cases} \mathcal{B} \times \mathcal{T} & \rightarrow & \mathcal{R}^6 \\ (\boldsymbol{X}, t) & \mapsto & \boldsymbol{G}^p(\boldsymbol{X}, t) \end{cases} \qquad \text{and} \qquad \boldsymbol{G}^c : \begin{cases} \mathcal{B} \times \mathcal{T} & \rightarrow & \mathcal{R}^6 \\ (\boldsymbol{X}, t) & \mapsto & \boldsymbol{G}^c(\boldsymbol{X}, t) \end{cases}, \tag{3.6}$$

with initial conditions $\boldsymbol{G}^{p,c}(t = t_0) = \boldsymbol{G}$. Considering MIEHE ET AL. [87], Hencky–type total, plastic and crazing strains are presented, i.e.

$$\boldsymbol{\varepsilon} := \frac{1}{2} \ln \boldsymbol{C} \,, \qquad \boldsymbol{\varepsilon}^p := \frac{1}{2} \ln \boldsymbol{G}^p \qquad \text{and} \qquad \boldsymbol{\varepsilon}^c := \frac{1}{2} \ln \boldsymbol{G}^c \,, \tag{3.7}$$

in the logarithmic strain space, which provides the usage of additive decomposition of the strain measurements analogous to small strain approach such that

$$\boldsymbol{\varepsilon}^e := \boldsymbol{\varepsilon} - \boldsymbol{\varepsilon}^p - \boldsymbol{\varepsilon}^c. \tag{3.8}$$

Since there is one-to-one correspondance between $\{\boldsymbol{\varepsilon}^p,\ \boldsymbol{\varepsilon}^c\}$ and $\{\boldsymbol{G}^p,\ \boldsymbol{G}^c\}$, the logarithmic inelastic strains $\boldsymbol{\varepsilon}^p$ and $\boldsymbol{\varepsilon}^c$ are used as internal variables elucidating the local inelastic deformations. Additionaly, we also introduce v_f representing the void volume fraction in a continuum point which serve as a micromechanically motivated damage variable, i.e.

$$v_f : \begin{cases} \mathcal{B} \times \mathcal{T} & \rightarrow & [v_{f0}, 1] \\ (\boldsymbol{X}, t) & \mapsto & v_f(\boldsymbol{X}, t) \end{cases} \tag{3.9}$$

where $v_f(t = t_0) = v_{f0}$ stands for the initial value of the void volume fraction.

3.1.2 Stress and heat flux

Consider a body which admits the Kirchhoff stress tensor $\boldsymbol{\tau}$. Then,

$$\boldsymbol{P} = \boldsymbol{\tau}\boldsymbol{F}^{-T} \qquad \text{and} \qquad \boldsymbol{S} = \boldsymbol{F}^{-1}\boldsymbol{\tau}\boldsymbol{F}^{-T}, \tag{3.10}$$

characterize the first Piola–Kirchhoff (nominal) and the second Piola–Kirchhoff stress tensor, respectively. Besides, let us consider the Cauchy–type (true) heat flux vector $\boldsymbol{q}$ and $\boldsymbol{h} = J\boldsymbol{q}$ being the corresponding Kirchhoff–type heat flux vector. The Cauchy–type and the Lagrangian heat flux vectors are related through the identity

$$\boldsymbol{Q} \cdot d\boldsymbol{A} = \boldsymbol{q} \cdot d\boldsymbol{a}. \tag{3.11}$$

where $d\boldsymbol{A}$ and $d\boldsymbol{a}$ are the infinitesimal material and spatial areal vectors, respectively. From (3.11), the material (Lagrangian) heat flux vector reads $\boldsymbol{Q} = \boldsymbol{F}^{-1}J\boldsymbol{q}$. Then, an important relation between the two for the subsequent construction is obtained via the Piola identity, i.e.

$$\text{Div}(\boldsymbol{Q}) = \boldsymbol{F}^{-1}J\text{Div}(\boldsymbol{q}) = J\,\text{div}\,(\boldsymbol{q}). \tag{3.12}$$

2

3.1.3 Thermodynamical framework

To construct the mathematical framework of thermodynamical restrictions for the multi-physics problem we are dealing with, it is introduced the rate of the total logarithmic strain first, i.e.

$$\dot{\boldsymbol{\varepsilon}} := \mathbb{T} : \frac{1}{2}\boldsymbol{\pounds}_{\boldsymbol{\nu}}\,\boldsymbol{g} \quad \text{and} \quad \dot{\mathbb{T}} := \mathbb{t} : \frac{1}{2}\boldsymbol{\pounds}_{\boldsymbol{\nu}}\,\boldsymbol{g} \tag{3.13}$$

in terms of the Eulerian transformation tensors $\mathbb{T}$ and $\mathbb{t}$ which is defined as first and second derivatives of the total logarithmic strain with respect to the spatial metric tensor $\boldsymbol{g}$ such that

$$\mathbb{T} := 2\partial_{\boldsymbol{g}}\boldsymbol{\varepsilon} \quad \text{and} \quad \mathbb{t} := 4\partial^2_{\boldsymbol{g}\boldsymbol{g}}\boldsymbol{\varepsilon}\,. \tag{3.14}$$

At a local point, the material response is assumed to depend on the total Hencky strain $\boldsymbol{\varepsilon}$, the plastic strain $\boldsymbol{\varepsilon}^p$, the crazing strain $\boldsymbol{\varepsilon}^c$ as well as the void volume fraction v_f, the crack phase–field d and the temperature θ. Then, the Helmholtz free energy is composed of these internal variables as follows

$$\Psi = \hat{\Psi}(\boldsymbol{\varepsilon}, \boldsymbol{\varepsilon}^p, \boldsymbol{\varepsilon}^c, v_f, d, \theta), \tag{3.15}$$

3.1.3.1 Local dissipation inequality

The local dissipation inequality, or namely the Clausius–Planck inequality, combined with the time derivative of the free energy function and in view of the Legendre transformation, i.e. $\Psi := e - \theta\eta_e$, in (3.15) yields

$$\mathcal{D}_{loc} := \boldsymbol{\tau} : \frac{1}{2}\boldsymbol{\pounds}_{\boldsymbol{\nu}}\, \boldsymbol{g} - \eta_e\dot{\theta} - \dot{\Psi} \;\geqslant\; 0, \tag{3.16}$$

where η_e stands for the specific entropy per unit volume. Insertion of the time derivative of (3.15) into (3.16) gives rise to

$$\mathcal{D}_{loc} := (\boldsymbol{\tau} - 2\partial_{\boldsymbol{g}}\Psi) : \frac{1}{2}\boldsymbol{\pounds}_{\boldsymbol{\nu}}\boldsymbol{g} - \partial_{\boldsymbol{\varepsilon}^p}\Psi : \dot{\boldsymbol{\varepsilon}}^p - \partial_{\boldsymbol{\varepsilon}^c}\Psi : \dot{\boldsymbol{\varepsilon}}^c - \partial_{v_f}\Psi\, \dot{v}_f - \partial_d\Psi\, \dot{d} - (\eta_e + \partial_\theta\Psi)\, \dot{\theta} \geqslant 0. \tag{3.17}$$

Here, $\boldsymbol{\tau}$ denotes the Kirchhoff stress tensor. The constitutive expressions for the Kirchhoff stress tensor and the corresponding logarithmic stress tensor, i.e. $\boldsymbol{\sigma}$, obtained from (3.17) by using Colemann–Noll exploitation method, i.e.

$$\boldsymbol{\tau} := 2\partial_{\boldsymbol{g}}\Psi = \partial_{\boldsymbol{\varepsilon}}\Psi : 2\partial_{\boldsymbol{g}}\boldsymbol{\varepsilon} = \boldsymbol{\sigma} : \mathbb{T} \qquad \text{where} \qquad \boldsymbol{\sigma} := \partial_{\boldsymbol{\varepsilon}}\Psi, \qquad \text{and} \qquad \eta_e := -\partial_\theta\Psi \tag{3.18}$$

in regard to the transformation tensor $\mathbb{T}$ in (3.14). This procedure directly leads to the reduced form of the Clausius–Planck inequality (3.17) in the following form

$$\mathcal{D}^{red}_{loc} := \boldsymbol{\sigma}^p : \dot{\boldsymbol{\varepsilon}}^p + \boldsymbol{\sigma}^c : \dot{\boldsymbol{\varepsilon}}^c + \sigma^{v_f}\dot{v}_f + \sigma^d\dot{d} \;\geqslant\; 0, \tag{3.19}$$

in which the thermodynamic driving stress tensors, i.e. $\boldsymbol{\sigma}^p$ and $\boldsymbol{\sigma}^c$, and scalars, i.e. σ^{v_f} and σ^d, are introduced which are work conjugate to the rate of the inelastic strains, i.e. $\dot{\boldsymbol{\varepsilon}}^p$ and $\dot{\boldsymbol{\varepsilon}}^c$, and the rate of the void volume fraction $\dot{v}_f$ and the crack phase–field $\dot{d}$. Their definitions are

$$\boldsymbol{\sigma}^p := -\partial_{\boldsymbol{\varepsilon}^p}\Psi, \quad \boldsymbol{\sigma}^c := -\partial_{\boldsymbol{\varepsilon}^c}\Psi, \quad \sigma^{v_f} := -\partial_{v_f}\Psi, \quad \sigma^d := -\partial_d\Psi. \tag{3.20}$$

We impose a stronger condition than (3.19 to split the processes of shear yielding, crazing, void growth and damage i.e.

$$\boldsymbol{\sigma}^p : \dot{\boldsymbol{\varepsilon}}^p \geqslant 0, \quad \boldsymbol{\sigma}^c : \dot{\boldsymbol{\varepsilon}}^c \geqslant 0, \quad \sigma^{v_f}\dot{v}_f \geqslant 0, \quad \sigma^d\dot{d} \geqslant 0. \tag{3.21}$$

3.1.3.2 Algorithmic tangent moduli

In order to derive these stress tensors, we set up the algorithmic expression for the tangent moduli by computing Lie–derivative of the Kirchhoff stress tensor $\boldsymbol{\tau}$ with

respect to the velocity $\boldsymbol{v}$ and the incremental deformation map $\Delta\boldsymbol{\varphi}$, obtaining

$$\begin{aligned} \boldsymbol{\pounds}_{\boldsymbol{\nu}}\boldsymbol{\tau} \quad &\rightarrow \quad \boldsymbol{\pounds}_{\Delta\boldsymbol{\varphi}}\boldsymbol{\tau} \\ \mathbb{c}^{algo} : \tfrac{1}{2}\boldsymbol{\pounds}_{\boldsymbol{\nu}}\,\boldsymbol{g} \quad &\rightarrow \quad \left(\mathbb{T}^T : \mathbb{E}^{algo} : \mathbb{T} + \boldsymbol{\sigma} : \mathbb{t}\right) : \tfrac{1}{2}\boldsymbol{\pounds}_{\Delta\boldsymbol{\varphi}}\boldsymbol{g}. \end{aligned} \tag{3.22}$$

The Eulerian tangent moduli $\mathbb{c}^{algo}$ follow from $(3.22)_2$, i.e.

$$\mathbb{c}^{algo} := \mathbb{T}^T : \mathbb{E}^{algo} : \mathbb{T} + \boldsymbol{\sigma} : \mathbb{t}, \tag{3.23}$$

which can be simply regarded as the geometric transformation between Eulerian and logarithmic arguments, i.e. the consistent logarithmic tangent moduli $\mathbb{E}^{algo}$ and the stress $\boldsymbol{\sigma}$.

3.1.3.3 Non-local heat conduction

The locally generated heat is conducted throughout the material in a non–local fashion as given in the conductive part of the total dissipation inequality known as the Fourier's inequality, i.e.

$$\mathcal{D}_{con} := -\frac{1}{\theta}\boldsymbol{Q}\cdot\nabla_{\boldsymbol{X}}\theta = -\frac{1}{\theta}\boldsymbol{q}\cdot\nabla_{\boldsymbol{x}}\theta \;\geqslant\; 0, \tag{3.24}$$

according to the material and spatial configurations. Moreover, the temperature gradients are described as follows

$$\mathfrak{G} := -\nabla_{\boldsymbol{X}}\theta \qquad \text{and} \qquad \mathfrak{g} := -\nabla_{\boldsymbol{x}}\theta, \tag{3.25}$$

in both reference and spatial configurations, respectively. The heat flux vectors outlined in Sec.3.1.2stand on an objective dissipation potential function for the given state of the material, i.e.

$$\Phi_{con} = \hat{\Phi}_{con}(\mathfrak{G};\boldsymbol{C},d,\theta,\boldsymbol{X}) = \hat{\Phi}_{con}(\mathfrak{g};\boldsymbol{g},\boldsymbol{F},d,\theta,\boldsymbol{X}). \tag{3.26}$$

It should be emphasized that the inequality in (3.24) is fulfilled as long as the Φ_{con} is adopted to be a convex function with respect to $\mathfrak{G}$ and $\mathfrak{g}$.

3.2 Evolution Equations

3.2.1 Shear yielding

As stated in BOYCE ET AL. [26], the local description of the shear yielding is manifested by an isotropic and isochoric viscoplastic flow in the direction of deviatoric

plastic force, see $(3.20)_1$, i.e.

$$\dot{\boldsymbol{\varepsilon}}^p = \dot{\gamma}^p \frac{\mathrm{dev}(\tilde{\boldsymbol{\sigma}}^p)}{\|\mathrm{dev}(\tilde{\boldsymbol{\sigma}}^p)\|} \quad \text{where} \quad \dot{\gamma}^p := \dot{\gamma}_0^p \exp\left\{-\frac{As}{\theta}\left[1-\left(\frac{\tilde{\sigma}^p}{\tilde{s}}\right)^{\frac{5}{6}}\right]\right\}, \tag{3.27}$$

in terms of the scalar flow function $\dot{\gamma}^p$ according to the double–kink theory which will be outlined under specification of the flow rule. In this manner, $\tilde{s}$ denotes the effective athermal shear strength of the polymer reckon with the pressure dependency of yielding, i.e.

$$\tilde{s} = s + \varrho\tilde{p}, \tag{3.28}$$

where p stands for the hydrostatic pressure and $\varrho \in [0.1, 0.2]$ is a parameter handling the pressure sensitivity of the yield stress, see, e.g., BOWDEN & JUKES [23]. In (3.27), $\mathrm{dev}(\tilde{\boldsymbol{\sigma}}^p) := \tilde{\boldsymbol{\sigma}}^p : \mathbb{P}$ designates the deviatoric part of the effective thermodynamic driving stress $\tilde{\boldsymbol{\sigma}}^p$ which is simply double contraction of that stress and fourth order projection tensor, $\mathbb{P} = \mathbb{I} - \mathbf{1} \otimes \mathbf{1}/3$. Parameters, such as the pre–exponential factor $\dot{\gamma}_0^p$, the lumped parameter A and the temperature θ are retrieved from experiments and/or micro–structural data. In addition, J_2 flow theory is incorporated into (3.27) via $\tilde{\sigma}^p$ such that

$$\tilde{\sigma}^p := \sqrt{J_2} = \sqrt{\frac{1}{2}\left[\ \mathrm{dev}(\tilde{\boldsymbol{\sigma}}^p) : \mathrm{dev}(\tilde{\boldsymbol{\sigma}}^p)\ \right]} \tag{3.29}$$

Other than the pressure dependence, stress softening which is observed in amorphous glassy polymers is assessed by a phenomenological evolution law for s, i.e.

$$\dot{s} = h_1\left(1 - \frac{s}{s_s(v_f)}\right)\dot{\gamma}^p \quad \text{with} \quad s(0) = s_0 \tag{3.30}$$

where s_0 and h_1 imply the material parameters controlling the initial value of the athermal shear strength s and the slope of the softening, respectively, while $s_s(v_f)$ denotes the saturation value of s and is considered as function of the void volume fraction v_f, i.e.

$$s_s(v_f) = s_{ss}[1 + h_2(v_f^{ss} - v_f)], \tag{3.31}$$

similar to the local free volume theory proposed by ANAND & GURTIN [7]. In (3.31), s_{ss} and v_f^{ss} are the steady–state values of s and v_f under shear yielding and h_2 is another material parameter controlling post-yield softening, respectively.

3.2.2 Crazing

The flow rule associated with crazing is assumed to occur in the direction of maximum principle tensile stress based on GEARING & ANAND [46] in the form of

$$\dot{\boldsymbol{\varepsilon}}^c = \dot{\gamma}^c \boldsymbol{f} \otimes \boldsymbol{f} \quad \text{where} \quad \dot{\gamma}^c = \dot{\gamma}_0^c \left(\frac{\tilde{\sigma}_{max}}{s_{cr}} \right)^m , \tag{3.32}$$

Here, $\dot{\gamma}^c$ is a scalar function for the craze flow and $\boldsymbol{f} = \boldsymbol{e}_{max}$ is denoted the eigenvector that refers to the effective maximum principle tensile stress, i.e. $\tilde{\sigma}_{max} = \max\{\tilde{\sigma}_A\}_{A=1,2,3}$,obtained from the spectral decomposition, i.e.

$$\tilde{\boldsymbol{\sigma}} = \sum_{A=1}^{3} \tilde{\sigma}_A \boldsymbol{e}_A \otimes \boldsymbol{e}_A. \tag{3.33}$$

In $(3.32)_2$, $\dot{\gamma}_0^c$ corresponds to the reference rate of the craze strain, while the resistance to craze flow is asserted by s_{cr} and m is just a parameter stands for the strain–rate sensitivity. We highlight that the eigenvector $\boldsymbol{f}$ is not changed once the craze initiates.

3.2.3 Void volume fraction

Craze nucleation is driven by both deviatoric and volumetric components of the applied stress. Hence, both the shear yielding and crazing mechanisms contributes the growth of the void volume fraction.

Shear yielding is only effective mechanism for the evolution of void volume fraction between $v_f \in [v_{f0}, v_f^{ss}]$. On the contrary, once craze initiation criterion is met then the void volume fraction evolves, i.e. $v_f \in [v_f^{ss}, 1]$, under the action of craze flow. Therefore, the evolution equation incorporates two cases, i.e.

$$\dot{v}_f : \begin{cases} h_3 \left(\frac{s}{s_{ss}} - 1 \right) \dot{\gamma^p} & \Longrightarrow \quad \text{shear yielding} \\ (1 - v_f)\, \mathrm{tr}(\dot{\boldsymbol{\varepsilon}}^c) & \Longrightarrow \quad \text{crazing} \end{cases} \tag{3.34}$$

where h_3 is another constant which control the slope of the growth. Note that such a interpretation is motivated by the classical growth theory related to crazing, beside the evolution of free volumes presented in GEARING & ANAND [46] is considered for shear yielding. Dealing with (3.30) in combination of (3.31) and $(3.34)_1$ as a system of ordinary differential equations (ODEs), we investigate the equilibrium points (critical points) on (s,v_f)–plane as $t \to 0$. Accepting h_1, h_2, h_3 and $\dot{\gamma^p}$ are all positive

scalars and solving the algebraic equations $\dot{s} = 0$ and $\dot{v}_f = 0$, the system come up to a single equilibrium point, i.e. (s_{ss}, v_f^{ss}). Consequently, $s \to s_{ss}$ and $v_f \to v_f^{ss}$ under shear yielding mechanism.

3.3 Global Equations of the Multi–Field Problem

The constituve framework emphasized in aforementioned sections embedded into governing global equations of the thermo-viscoplastic fracture at finite strains. First, we outline fundamental balance laws that satisfy the core axioms of the thermomechanics are the balance of linear and angular momentum such that

$$J \operatorname{div}(\boldsymbol{\tau}/J) + \rho_0 \boldsymbol{\gamma} = \mathbf{0} \quad \text{and} \quad \boldsymbol{\tau}^T = \boldsymbol{\tau}, \tag{3.35}$$

governing the initial boundary value problem. ρ_0 stands for the density of the reference configuration and $\boldsymbol{\gamma}$ is the prescribed body–force field. $\operatorname{div}(\bullet)$ denotes the divergence operator with respect to the spatial coordinates $\boldsymbol{x}$. The second global equation is the nonlocal evolution equation of the crack phase–field for a rate dependent case

$$\dot{d} = \frac{1}{\eta}[2(1-d)\mathcal{H} - \frac{1}{l}(d - l^2 \Delta d)] \,, \tag{3.36}$$

driven by the local history field $\mathcal{H}$ storing the loading unloading conditions in terms of the relevant quantities which will be specified in Section 3.4. The term $\Delta(\bullet) = \operatorname{Div}[\operatorname{Grad}(\bullet)]$ represents the Laplace operator with respect to the reference coordinates $\boldsymbol{X}$. The l indicates the length–scale parameter appear in the phase-field theory inherently whereas the artificial viscosity parameter, η, is for stabilization of the solution algorithm. For very small values of the length–scale, the Laplacian term can be omitted. Then, it conduces to a closed form solution for the local evolution of the phase-field. The desired growth conditions for the phase–field from initially intact state, i.e. $d = 0$, to a fully broken state where $d = 1$ are satisfied by a monotonically increasing specific crack driving source term $\mathcal{H}$.

The third global equation features the balance of internal energy, i.e.

$$\dot{e} = \boldsymbol{\tau} : \frac{1}{2} \pounds_{\boldsymbol{\nu}} \, \boldsymbol{g} + r - J \operatorname{div}(\boldsymbol{q}), \tag{3.37}$$

in the spatial configuration where e refers to the specific energy per unit volume, while r is the prescribed heat source. With the first law of thermodynamics at hand, one can

exploit the Legendre transformation, i.e. $e = \Psi + \theta\eta_e$. Taking the time derivative of the Legendre transformation and substituting (3.18) and (3.19) into $\dot{\Psi}$, we arrive at the following intermediate result, i.e.

$$\dot{e} = \boldsymbol{\tau} : \frac{1}{2}\boldsymbol{\pounds}_{\boldsymbol{\nu}}\, \boldsymbol{g} - \mathcal{D}_{loc}^{red} + \theta\dot{\eta}_e. \tag{3.38}$$

Comparing (3.37) and (3.38) we obtain the evolution equation for the entropy

$$\theta\dot{\eta}_e = -J\,\mathrm{div}(\boldsymbol{q}) + r + \mathcal{D}_{loc}^{red}, \tag{3.39}$$

Remembering the definition of the entropy $(3.18)_2$ the temperature times the evolution of the entropy with respect to time reads

$$\begin{aligned} \theta\dot{\eta}_e &= \theta\partial_\theta\eta_e\dot{\theta} - \theta\partial_\theta(\boldsymbol{\tau} : \tfrac{1}{2}\boldsymbol{\pounds}_{\boldsymbol{\nu}}\, \boldsymbol{g} - \mathcal{D}_{loc}^{red}) \\ &= c\dot{\theta} - \mathcal{L}, \end{aligned} \tag{3.40}$$

where we have introduced the specific heat capacity and latent heating, i.e.

$$c := \theta\partial_\theta\eta_e = -\theta\partial_{\theta\theta}^2\Psi \qquad \text{and} \qquad \mathcal{L} := \theta\partial_\theta(\boldsymbol{\tau} : \frac{1}{2}\boldsymbol{\pounds}_{\boldsymbol{\nu}}\, \boldsymbol{g} - \mathcal{D}_{loc}^{red}), \tag{3.41}$$

respectively. Next, the evolution equation of the temperature follows from (3.40) substituted into (3.39) such that

$$c\dot{\theta} = -J\,\mathrm{div}(\boldsymbol{q}) + r + \mathcal{D}_{loc}^{red} + \mathcal{L}. \tag{3.42}$$

we end up with $\boldsymbol{q} \equiv 0$ and $r \equiv 0$ for an adiabatic process. As stated in MIEHE [84],for entropic thermo-elasticity the amount of latent heating is remarkably small compared to the dissipative heating . Hence, one can omit the latent heating, i.e. $\mathcal{L} \approx 0$ without loss of generality.

3.4 Specific Constitutive Functions

3.4.1 Free energy function

The free energy introduced in (3.15) can be decomposed into thermally coupled elastic and plastic parts along with a purely thermal contribution, i.e.

$$\begin{aligned} \hat{\Psi}(\boldsymbol{\varepsilon}, \boldsymbol{\varepsilon}^p, \boldsymbol{\varepsilon}^c, d, v_f, \theta) &:= \hat{\Psi}^e(\boldsymbol{\varepsilon}^e, d, \theta) + \hat{\Psi}^p(\boldsymbol{\varepsilon}^p, v_f, \theta) + \hat{\Psi}^\theta(\theta) \\ &= g^e(d)\hat{\Psi}_0^e(\boldsymbol{\varepsilon}^e, \theta) + g^p(v_f)\hat{\Psi}_0^p(\boldsymbol{\varepsilon}^p, \theta) + \hat{\Psi}^\theta(\theta), \end{aligned} \tag{3.43}$$

where $\hat{\Psi}_0^e(\boldsymbol{\varepsilon}^e, \theta)$ and $\hat{\Psi}_0^p(\boldsymbol{\varepsilon}^p, \theta)$ account for the elastic impetus of the chains and the entropic resistance to molecular alignment, acting as potentials for the effective and back–stress response, respectively. $g^e(d)$ and $g^p(v_f)$ show the degradation functions due to phase–field and void volume fraction acting on the elastic and the plastic part of the free energy function, respectively. We highlight that $g^p(v_f)$ would only be operational provided that the switch function (3.63) is dropped out of the constitutive formulation, see DAL ET AL. [37] for the related discussion. Unlike $\hat{\Psi}_0^e(\boldsymbol{\varepsilon}^e, \theta)$ and $\hat{\Psi}_0^p(\boldsymbol{\varepsilon}^p, \theta)$, the thermally stored energy $\hat{\Psi}^\theta(\theta)$ is not influenced by the fracture or void growth so thermal energy is not released instantaneously right after fracture occurs. In accordance with the additive split of the free energy, the effective plastic driving force $(3.20)_1$ is obtained via

$$\tilde{\boldsymbol{\sigma}}^p = \tilde{\boldsymbol{\sigma}} - \tilde{\boldsymbol{\sigma}}^b \quad \text{with} \quad \tilde{\boldsymbol{\sigma}} := \partial_{\boldsymbol{\varepsilon}^e} \hat{\Psi}_0^e(\boldsymbol{\varepsilon}^e, \theta) \quad \text{and} \quad \tilde{\boldsymbol{\sigma}}^b := \partial_{\boldsymbol{\varepsilon}^p} \hat{\Psi}_0^p(\boldsymbol{\varepsilon}^p, \theta), \tag{3.44}$$

in the sense of the effective stress and back–stress tensors $\tilde{\boldsymbol{\sigma}}$ and $\tilde{\boldsymbol{\sigma}}^b$ formulated in the logarithmic strain space. It should be underlined that only the effective deviatoric part of the driving force $\tilde{\boldsymbol{\sigma}}^p$ enters the flow rule (3.27).

3.4.1.1 Thermo-elastic contribution

Amorphous glassy polymers show noticeably small elastic deformation before yielding. Therefore, linear elastic model can be used to describe the behavior of the material in that regime, i.e.

$$\hat{\Psi}_0^e(\boldsymbol{\varepsilon}^e, \theta) = \frac{\kappa}{2} \operatorname{tr}^2(\boldsymbol{\varepsilon}^e) - \kappa \alpha_T \operatorname{tr}(\boldsymbol{\varepsilon}^e)\,(\theta - \theta_0) + \hat{\mu}(\theta)\,\|\operatorname{dev}(\boldsymbol{\varepsilon}^e)\|^2\,, \tag{3.45}$$

where κ, $\hat{\mu}(\theta)$ and α_T stand for the bulk modulus, the temperature dependent shear modulus and the thermal expansion coefficient, respectively, while θ_0 denotes the initial temperature of the material. The effective Kirchhoff stress and its logarithmic counterpart are obtained by exploitation of (3.18), i.e.

$$\tilde{\boldsymbol{\tau}} := \tilde{\boldsymbol{\sigma}} : \mathbb{T} \quad \text{where} \quad \tilde{\boldsymbol{\sigma}} := \kappa\big[\operatorname{tr}(\boldsymbol{\varepsilon}^e) - \alpha_T(\theta - \theta_0)\big]\boldsymbol{1} + 2\hat{\mu}(\theta)\operatorname{dev}(\boldsymbol{\varepsilon}^e). \tag{3.46}$$

Temperature effect on the shear modulus can be identified by the following empirical relation as proposed in BOYCE ET AL. [25]

$$\hat{\mu}(\theta) = \exp\big[\ln(\mu_r) - c_s(\theta - \theta_r)\big]\,, \tag{3.47}$$

in which θ_r, μ_r and c_s represent the reference temperature, shear modulus at reference temperature and sensitivity parameter, respectively.

3.4.1.2 Thermoplastic contribution

The plastic part of the intact free energy describes the post–kinematic hardening effect via effective back–stress $\tilde{\boldsymbol{\sigma}}^b$ resulting from the intramolecular resistance to the plastic flow owing to the chain alignment in the principal deformation directions, see $(3.44)_3$. Also, amorphous glassy polymers show entropic nature as in rubbery polymers. Hence, polymer network theories are oftenly used to model plastic part of the free energy function and post–kinematic hardening region.

There are pervasive approaches in the literature which construct a relationship between microscopic and macroscopic deformations through particular kinematic assumptions, see among others the three chain model of JAMES & GUTH [64] and WANG & GUTH [114], the eight chain model of ARRUDA & BOYCE [14]. We refer to DAL ET AL. [35] for further information. As the plastic part is modelled as polymer network, it can be considered to be isotropic and can be identified by plastic principal stretches, i.e.

$$\lambda_i^p = \exp(\epsilon_i^p) \quad \text{where} \quad i = 1, 2, 3. \tag{3.48}$$

These are derived by the spectral decomposition of the plastic stretch tensor via the Hencky–type plastic strain $\boldsymbol{\varepsilon}^p$, i.e.

$$\boldsymbol{U}^p := \boldsymbol{G}^{p\,1/2} = \exp(\boldsymbol{\varepsilon}^p) = \sum_{i=1}^{3} \exp(\epsilon_i^p)\, \boldsymbol{n}_i^p \otimes \boldsymbol{n}_i^p, \tag{3.49}$$

where $\{\boldsymbol{n}_i^p\}_{i=1,2,3}$ are the principal directions of the plastic strain. We directly adopt the eight chain model proposed by ARRUDA & BOYCE [14] all among the polymer network theories mentioned above. Accordingly, the network stretch Λ^p is calculated from the following relationship

$$\Lambda^{p2} := \frac{1}{3}(\lambda_1^{p2} + \lambda_2^{p2} + \lambda_3^{p2}) = \frac{1}{3}\mathrm{tr}(\boldsymbol{G}^p). \tag{3.50}$$

Conclusively, one can declare the energetic state of the full network considering the energy of a fictitious prototype chain via

$$\hat{\Psi}_0^p(\hat{\Lambda}_r^p, \theta) = \hat{\mu}^p(\theta)\hat{N}^p(\theta)\left(\hat{\Lambda}_r^p(\theta)\mathcal{L}^{-1}[\hat{\Lambda}_r^p(\theta)] + \ln\frac{\mathcal{L}^{-1}[\hat{\Lambda}_r^p(\theta)]}{\sinh\mathcal{L}^{-1}[\hat{\Lambda}_r^p(\theta)]}\right). \tag{3.51}$$

Here, $\hat{\mu}^p(\theta)$ and $\hat{N}^p(\theta)$ represent the thermally dependent plastic shear modulus and the number of segments per chain, respectively. In fact, the standard argument based on TRELOAR [111] determines the plastic shear modulus

$$\hat{\mu}^p(\theta) = \hat{n}^p(\theta) k_B \theta, \tag{3.52}$$

where $n^p(\theta)$ stands for the temperature dependent fictitious chain density, while k_B is the Boltzmann constant. Unlike cross–linked rubbery polymers, the chain density in amorphous glassy polymers is not constant rather subject to decrease as the temperature of the domain rises. This phenomenon is elucidated according to RAHA & BOWDEN [101] and ARRUDA ET AL. [16] by the following empirical relation

$$\hat{n}^p(\theta) = B - D \exp\left(-\frac{E_d}{R\theta}\right), \tag{3.53}$$

in which B and D appear as constants, while E_d denotes the dissociation energy of the entanglements in the molecular network. R stands for the gas constant. The ratio between B and D can be determined from experimental observations conducted at the glass transition temperature θ_g, whereby the molecular network completely breaks down leading to $\hat{n}^p(\theta) = 0$. Then, we have

$$\frac{B}{D} = \exp\left(-\frac{E_d}{R\theta_g}\right), \tag{3.54}$$

according to BASU & GIESSEN [17]. The total number of rigid links in the network is assumed to be conserved at any temperature, i.e. $\hat{n}^p(\theta)\hat{N}^p(\theta) = const.$, whereby the actual number of segments per chain can be calculated as follows,

$$\hat{N}^p(\theta) = \frac{\hat{n}^p(\theta_r)}{\hat{n}^p(\theta)} \hat{N}^p(\theta_r), \tag{3.55}$$

see, e.g., ARRUDA ET AL. [16] and the references therein. Here, $\hat{n}^p(\theta_r)$ and $\hat{N}^p(\theta_r)$ express the chain density and the number of segments for a single chain at the reference temperature θ_r. Returning back to (3.51), $\mathcal{L}^{-1}[\cdot]$ denotes nothing but the inverse of the well–known Langevin function, i.e. $\mathcal{L}[\cdot] := \coth(\cdot) - 1/(\cdot)$. In following section, well accepted approaches are classified and investiagated by means of complexity and accuracy.

In proposed approach, Padè approximation for the inverse Langevion function is used, i.e.

$$\mathcal{L}^{-1}[\hat{\Lambda}_r^p(\theta)] \approx \hat{\Lambda}_r^p(\theta) \frac{3 - \hat{\Lambda}_r^{p2}(\theta)}{1 - \hat{\Lambda}_r^{p2}(\theta)}, \tag{3.56}$$

see COHEN [33] for details. In (3.51), the temperature dependent relative plastic network stretch $\hat{\Lambda}_r^p(\theta) := \Lambda^p/\sqrt{\hat{N}^p(\theta)}$ where $\hat{\Lambda}_r^p(\theta) \in [0,1]$ gives an account of the limited extensibility of the chains as $\hat{\Lambda}_l^p(\theta) = \sqrt{\hat{N}^p(\theta)}$ being the locking stretch. Accordingly, the back–stress $(3.44)_3$ in the logarithmic strain space is computed via the chain rule

$$\tilde{\boldsymbol{\sigma}}^b := \partial_{\hat{\Lambda}_r^p} \hat{\Psi}_0^p(\hat{\Lambda}_r^p, \theta)\, \partial_{\Lambda^p} \hat{\Lambda}_r^p\, \partial_{\lambda_i^p} \Lambda^p\, \partial_{\epsilon_i^p} \lambda_i^p\, \partial_{\boldsymbol{\varepsilon}^p} \epsilon_i^p \quad \text{where} \quad i \in \{1,2,3\}. \tag{3.57}$$

Inserting the respective derivatives into (3.57) we end up with the effective back–stress tensor

$$\tilde{\boldsymbol{\sigma}}^b := \frac{\hat{\mu}^p(\theta)}{3} \left(\frac{3\hat{N}^p(\theta) - \Lambda^{p2}}{\hat{N}^p(\theta) - \Lambda^{p2}} \right) \boldsymbol{G}^p \qquad \text{with} \qquad \boldsymbol{G}^p = \sum_{i=1}^{3} \lambda_i^{p2} \boldsymbol{n}_i^p \otimes \boldsymbol{n}_i^p. \tag{3.58}$$

It should be emphasized that only the deviatoric part of the effective back–stress $\tilde{\boldsymbol{\sigma}}^b$ enters the flow rule in (3.27).

3.4.1.3 Thermal contribution

Following form is enough to elucidate to purely thermal part of the free energy function, i.e

$$\hat{\Psi}_0^\theta(\theta) = -c \left[\theta \frac{\theta}{\theta_0} - (\theta - \theta_0) \right], \tag{3.59}$$

Here, c denotes the specific heat capacity while θ_0 indicates the initial temperature of the body.

3.4.2 Degradation functions

The degradation function for the elastic part $g^e(d)$ in (3.43) describes the softening of the material with evolving damage parameter d. The chosen function must satisfy following restrictions

$$g^e(0) = 1, \quad g^e(1) = 0, \quad \partial_d g^e(1) = 0. \tag{3.60}$$

The first two constraints in (3.60) set limits for the intact and the ruptured state of the material, whereas the latter condition ensures that the energy dissipation reaches a saturated value as the damage converges to the fully–broken state, i.e. $d = 1$. Even alternative forms of degradation functions can be found in KUHN ET AL. [74] and

BORDEN ET AL. [20], we prefer to directly adopt a simple quadratic form for $g^e(d)$ which satisfies predefined conditions in the sense of MIEHE ET AL. [94].

$$g^e(d) = (1-d)^2, \tag{3.61}$$

Note that $g^e(d)$ acts on only elastic part of the free energy function in (3.43). Since accumulated plastic deformation is not altered by fracture, plastic energy release does not take place. Therefore, it is assumed that plastic stored energy is not affected by fracture in general.

Glassy polymers lose their ability of exhibiting ductile response due to evolution of voids in the material and they start to show brittle-type response. Therefore, the degradation function $g^p(v_f)$ is plugged into plastic part of the free energy function to emphasize the decline the contribution of the plastic part due to shear yielding in an analogous form to (3.61), i.e.

$$g^p(v_f) = (1-v_f)^2, \tag{3.62}$$

The proposed degradation form above is enough to characterize the lessening in the plastic contribution accounting for the void growth.

3.4.3 Craze nucleation criterion

Simultaneous evolution of both shear yielding and crazing is omitted[1],see DAL ET AL. [37] for further discussion . Alternatively, we consider two serial viscoplastic dashpots together with an irreversible switch function F_c for the onset of crazing

$$F_c(\tilde{\boldsymbol{\sigma}}) : \begin{cases} f_c(\tilde{\boldsymbol{\sigma}}) \leqslant 0 \quad \vee \quad \tilde{\sigma}_{max} \leqslant 0 \quad \vee \quad \tilde{\sigma}_{vol} \leqslant 0 \quad \Longrightarrow \text{shear yielding} \\ f_c(\tilde{\boldsymbol{\sigma}}) > 0 \quad \wedge \quad \tilde{\sigma}_{max} > 0 \quad \wedge \quad \tilde{\sigma}_{vol} > 0 \quad \Longrightarrow \text{crazing} \end{cases} \tag{3.63}$$

where the effective mean normal stress (negative hydrostatic pressure) is defined as $\kappa[\mathrm{tr}(\boldsymbol{\varepsilon}^e) - \alpha_T(\theta - \theta_0)]$ in the logarithmic strain space and f_c stands for the nucleation function to be stated. At the beginning, the material behaves viscoplastic in which the crazing strains have not evolved yet, $\dot{\boldsymbol{\varepsilon}}^c = \mathbf{0}$. When the stress state of the material reaches the criterion proposed in (3.63), craze initiates and the rate of plastic strains due to shear yielding become frozen $\dot{\boldsymbol{\varepsilon}}^p = \mathbf{0}$. It needs to be underlined that the plastic deformation due to shear yielding is a volume preserving process, i.e.

$\mathrm{tr}(\boldsymbol{\varepsilon}^p) = 0$, which is in accordance with the finite viscoplastic behavior of ductile amorphous glassy polymers. However, crazing is associated with dilatational plastic straining, thereby making the inelastic flow compressible once the craze nucleation criterion (3.63) is satisfied. Influenced by the criterion proposed by STERNSTEIN & MYERS [105] we enhance the following craze initiation function in the sense of GEARING & ANAND [46] to provide temperature dependency, i.e.

$$f_c(\tilde{\boldsymbol{\sigma}}, \theta) = \tilde{\sigma}_{max} - \left(\hat{c}_1(\theta) + \frac{\hat{c}_2(\theta)}{\tilde{\sigma}_{vol}} + \hat{c}_3(\theta)\tilde{\sigma}_{vol} \right) \quad \text{with} \quad \hat{c}_3(\theta) = \frac{3\nu(\theta)}{1+\nu(\theta)}, \tag{3.64}$$

where $\hat{c}_1(\theta)$ [MPa], $\hat{c}_2(\theta)$ [MPa^2], and $\hat{c}_3(\theta)$ [-] represent temperature dependent material parameters according to

$$\hat{c}_i(\theta) = \hat{c}_i(\theta_r) \exp\left(\frac{\mathcal{Q}_i}{k_B \theta}\right) \quad \text{where} \quad i = 1, 2. \tag{3.65}$$

Therein, $\mathcal{Q}_1$ [Nmm] and $\mathcal{Q}_2$ [Nmm] should be determined from experimental data as proposed by TIJSSENS ET AL. [108]. Note that in $(3.64)_2$, $\nu(\theta)$ denote the temperature dependent Poissons' ratio. Given criterion in (3.63) operates as a one–way switch function in proposed model.

3.4.4 Local history field as a failure criterion

For the purpose of establish the novel failure criterion for simultaneous modeling of ductile and brittle fracture, we introduce an equivalent plastic strain due to the shear yielding

$$\alpha := \|\boldsymbol{\varepsilon}^p\| = \sqrt{\boldsymbol{\varepsilon}^p : \boldsymbol{\varepsilon}^p}. \tag{3.66}$$

Then we propose the crack driving source term in (3.36) for the local evolution of of the crack phase field d.

$$\mathcal{H}(\boldsymbol{x}, \alpha, v_f, t) := \zeta \langle \left(\frac{\alpha}{\bar{\alpha}}\right)^2 + \left(\frac{v_f}{\bar{v}_f}\right)^2 - 1 \rangle, \tag{3.67}$$

[1] Concurrent evolution of crazing and shear yielding has been profoundly investigated by postulating a single evolution equation of the inelastic strains, that is, $\dot{\boldsymbol{\varepsilon}}^{pc} = g^c(v_f)\dot{\boldsymbol{\varepsilon}}^c + g^p(v_f)\dot{\boldsymbol{\varepsilon}}^p$ resulting in $\boldsymbol{\varepsilon}^e = \boldsymbol{\varepsilon} - \boldsymbol{\varepsilon}^{pc}$. There, $g^c(v_f)$ signifies a general growth function for crazing, e.g., $g^c(v_f) = v_f^2$, while $g^p(v_f)$ is a degradation function for shear yielding analogous to (3.61). Such a formalism dispenses with the plastic incompressibility. However, this has led to enormous numerical issues, especially when combined with phase-field modeling of fracture and could not be circumvented. Therefore, we need to rely on the switch function separating the evolution of the two phenomena. In this case, the degradation term $g^p(v_f)$ in front of $\hat{\Psi}_0^p(\boldsymbol{\varepsilon}^p)$ in (3.43) becomes trivial since the switch function already carries out the intended purpose in an abrupt manner.

ζ is a parameter associated with the growth process for the crack phase field and the Macaulay brackets, i.e. $\langle x \rangle = \frac{1}{2}(x + |x|)$, ensure only the positive values are taken into account.Therein, $\bar{\alpha}$ and $\bar{v}_f$ are the critical equivalent plastic strain and void volume fraction associated with shear yielding and crazing, respectively.
Such a modality in constitutive modelling of amorphous glassy polymers can not only relate the phenomena of crazing to more physically grounded measure rathert than the extant criteria in the literature but also simultaneously models shear yielding and crazing induced crack initiation and growth in the context of crack phase–field approach.

3.4.5 Dissipation potential for heat conduction

The objective dissipation potential function stated in (3.26) represent the heat flux within the body and is formulated in the following convex quadratic form

$$\hat{\Phi}_{con}(\mathfrak{g}; \boldsymbol{g}, \boldsymbol{F}, \theta) = \frac{1}{2}\, k\, \boldsymbol{g}^{-1} : \mathfrak{g} \otimes \mathfrak{g}, \tag{3.68}$$

where $\mathfrak{g}$ is the temperature gradient vector in the spatial configuration and k is the heat conductivity constant which is chosen greater than zero in order to generate a positive dissipation. From (3.68) we conclude the Cauchy–type (true) heat flux vector defined in Sec.3.1.2, i.e.

$$\boldsymbol{q} = k\mathfrak{g}\boldsymbol{g}^{-1} = -k\nabla_{\boldsymbol{x}}\theta\boldsymbol{g}^{-1}. \tag{3.69}$$

The Lagrangian equivalent of (3.69) is given as

$$\boldsymbol{Q} = k\mathfrak{G}\boldsymbol{C}^{-1} = -k\nabla_{\boldsymbol{X}}\theta\boldsymbol{C}^{-1}. \tag{3.70}$$

3.5 Global algorithmic treatment

The coupled global field equations stated in (3.35), (3.36) and (3.42) in Sec. 3.3 describe the multi–physics nature of the phenomena in an analytical sense. To go one step further in the numerical development, let us focus on a time interval $[\, t_n,\, t_{n+1}\,] \subset \mathcal{R}$ during which the initial boundary–value problem is depicted by the initial conditions at t_n, i.e.

$$\{\, \boldsymbol{\varphi},\, d,\, \theta\}|_{(t=t_n)} = \{\, \boldsymbol{\varphi}_n,\, d_n,\, \theta_n\}, \tag{3.71}$$

for the primary field variables. In what follows, the Dirichlet–type boundary conditions for the deformation field, the crack phase–field and the temperature field are

prescribed as follows

$$\boldsymbol{\varphi} = \bar{\boldsymbol{\varphi}} \quad \text{on } \partial\mathcal{B}_{\varphi}, \qquad d = \bar{d} \quad \text{on } \partial\mathcal{B}_{d} \quad \text{and} \quad \theta = \bar{\theta} \quad \text{on } \partial\mathcal{B}_{\theta}, \tag{3.72}$$

along with the Neumann–type boundary conditions, i.e.

$$\boldsymbol{\tau}\cdot\boldsymbol{n} = \bar{\boldsymbol{t}} \quad \text{on } \partial\mathcal{S}_{t}, \qquad \nabla_{\boldsymbol{X}} d\cdot\boldsymbol{N} = 0 \quad \text{on } \partial\mathcal{B}_{\nabla d} \quad \text{and} \quad \boldsymbol{h}\cdot\boldsymbol{n} = \bar{h} \quad \text{on } \partial\mathcal{S}_{h}. \tag{3.73}$$

In (3.73), $\boldsymbol{N}$ and $\boldsymbol{n} = \boldsymbol{F}^{-T}\boldsymbol{N}$ are the outward normals on the surface $\partial\mathcal{B}$ of the reference configuration and $\partial\mathcal{S}$ of the spatial configuration. Having demonstrated the initial and boundary conditions of the multi–field problem, an important concept apropos the thermal problem awaits to be set on the exterior boundary which is the convective heat exchange. A linear relationship holds for the heat exchange between the ambient and the solid domain such that

$$\bar{h} = h_c(\theta - \theta_{\infty}) \quad \text{on } \partial\mathcal{S}_{h}, \tag{3.74}$$

where h_c is the coefficient of the convective heat exchange and θ_{∞} represent the ambient temperature. The numerical setup starts with the one–pass operator splitting algorithm featuring a concept of dividing the non-convex monolithic problem into convex sub–problems according to $\boldsymbol{\varphi}$, θ and d. In this way, they are successively updated in a typical time step $\Delta t = t_{n+1} - t_n$,

$$ALGO_{MTC} = ALGO_M \circ ALGO_T \circ ALGO_C, \tag{3.75}$$

where each partitioned system reads

$$\begin{aligned}
(M) \quad : \quad & \begin{cases} J\,\mathrm{div}(J^{-1}\boldsymbol{\tau}) + \rho_0\boldsymbol{\gamma} = \boldsymbol{0} \\ \dot{\theta} = 0 \\ \dot{d} = 0, \end{cases} \\
(T) \quad : \quad & \begin{cases} \dot{\boldsymbol{\varphi}} = \boldsymbol{0} \\ \dot{\theta} = -J\,\mathrm{div}(\boldsymbol{q})/c + \mathcal{D}^{red}_{loc}/c \\ \dot{d} = 0, \end{cases} \\
(C) \quad : \quad & \begin{cases} \dot{\boldsymbol{\varphi}} = \boldsymbol{0} \\ \dot{\theta} = 0 \\ \dot{d} = \dfrac{1}{\eta}[2(1-d)\mathcal{H} - \dfrac{1}{l}(d - l^2\Delta d)]. \end{cases}
\end{aligned} \tag{3.76}$$

Therein, the mechanical step (M) is solved for the frozen the temperature and the crack phase–field $\theta_{n+1} = \theta_n$ and $d_{n+1} = d_n$, respectively, whereas the temperature evolution step (T) admits a frozen deformation map $\boldsymbol{\varphi}_{n+1} = \boldsymbol{\varphi}_n$ and the frozen crack phase–field $d_{n+1} = d_n$. Finally, the evolution step for the crack phase–field accepts the frozen states for the deformation map and the temperature in which $\boldsymbol{\varphi}_{n+1} = \boldsymbol{\varphi}_n$ and $\theta_{n+1} = \theta_n$, respectively. Note that all variables without subscript are hereinafter evaluated at time t_{n+1} and gradients without subscripts, i.e. $\nabla(\cdot)$, refer to the reference configuration.

3.6 A one-pass predictor-corrector algortihm for the inverse Langevin function

Langevin function, named after *Paul Langevin*, is expressed by

$$\mathcal{L}(x) = \coth x - \frac{1}{x}\,, \tag{3.77}$$

where $\coth x$ is hyperbolic cotangent. Its inverse function is widely used in several fields of statistical mechanics such as magnetism, polymer physics [73] and rubber elasticity [41]. Since the *inverse Langevin function* $\mathcal{L}^{-1}(x)$ cannot be expressed in closed form, there are mainly two ways to compute it: (i) by approximate functions and (ii) numerical methods. Approximate functions can be classified into three classes: power series [41, 63, 110], rational functions [33, 38, 65, 73, 100, 111] and trigonometric functions [19, 69, 70]. Taylor series expansion is the most commonly used power series approximation for an arbitrary function yielding very accurate predictions within a convergence radius that increases with increased number of series terms [62, 110]. However, the Taylor series approximation is divergent in the limit $y = \mathcal{L}(x) \to 1$. The general formula for the Taylor series expansion of the inverse Langevin function is

$$\mathcal{L}^{-1}(y) \approx \sum_{k=1}^{n} a_k y^k, \quad a_{2k} = 0 \quad \text{for} \quad k = 1, ..., n \tag{3.78}$$

First five non-zero terms of Taylor series expansion for the inverse Langevin function were introduced by KUHN & GRÜN [75] and it paved the way for further contributions based on Taylor expansion [15, 115, 120]

$$\mathcal{L}^{-1}(y) \approx 3y + \frac{y^3}{5} + \frac{297y^5}{175} + \frac{1539y^7}{785} + \frac{126117y^9}{67375}. \tag{3.79}$$

A simple iterative procedure to obtain the coefficients a_i of the Taylor series at any order is proposed by KRÖGER [73]. Recently, radius of convergence of Taylor series for the inverse Langevin function was estimated as $r = 0.904$ [66] for first 1500 non-zero terms of Taylor expansion on the basis of the procedure by MERCER & ROBERTS [82]. Since $r < 1$, Taylor series of the inverse Langevin function cannot provide accurate results near the singularity around $y \approx 1$ [62]. Rational functions are proposed as an alternative for approximating the inverse Langevin function. It is based on Padé approximant technique which is expanding a given function $f(x)$ as a ratio of two power series. These functions are usually more accurate, yet they have more complex mathematical forms. Many approximation functions [33,38,65,73,100,110] have been proposed with different level of accuracy and complexity based on Padé approximant technique but most common approximation of the inverse Langevin function in rubber mechanics is the Cohen's approximation [33]. Other approximate functions will be discussed in the following section. Last class of approximants is the trigonometric functions [19,69,70]. BERGSTRÖM [19] suggested a piecewise function that contains trigonometric terms. His approach has lower maximum relative error compared to functions based on Padé approximant. However, its implementation into analytical works is quite compelling due to its piecewise form. Several approximations based on non-piecewise trigonometric functions were developed to handle this difficulty [69,70]. In recent years, numerical techniques have been used to find better approximations for the inverse Langevin function. MARCHI& ARRUDA [80] introduced new formulae in the form of rational functions resulting from a standard optimization problem. Coefficients in the formulae were obtained by the method of differential evolution. MOROVATI ET AL. [95] proposed an approach that consists of two parts: first part is the main function ($f(x)$) with correct poles and residues and second part is a power series ($\mathcal{M}(\mathcal{E})$) derived to reduce the error $\mathcal{E}$ arising from chosen main function.

$$\mathcal{L}^{-1}(x) = f(x) + \mathcal{M}(\mathcal{E}) \text{ with } \mathcal{E} = \mathcal{L}^{-1}(x) - f(x)\,. \tag{3.80}$$

Adding more terms in the Maclaurin series $\mathcal{M}$ reduces the relative error. To illustrate the proposed approach, they considered two main functions: namely a Warner-like function ($\frac{2x}{1-x^2}$) and a trigonometric function ($\frac{\pi}{2}\tan(\frac{\pi}{2}x)$). Furthermore, they optimized the coefficient of the last term of power series to reduce the relative error.

Among all these type of approaches, there is a tradeoff between accuracy and complexity. The interested reader is referred to the excellent reviews of KRÖGER [73], MARCHI & ARRUDA [80], MOROVATI ET AL. [95].

In this work, we propose a one-pass predictor-corrector algorithm for the approximation of the inverse Langevin function. In the predictor step, an approximant function $y_p(x)$ is used to predict the inverse of the Langevin function $y(x) = \mathcal{L}^{-1}(x)$. In order to improve the approximation y_p an error function $\mathcal{E}(y_p) = \mathcal{L}(y_p) - x$ is introduced. The linearization of $\mathcal{E}(y_p)$ around y_p and its y-intercept $y_p^\star$ leads to the corrected value of the approximant. The novelty of the approach lies in the fact that, the current corrector is a function of y_p rather than "x", opposed to the the correction terms proposed in the literature.

3.6.1 Proposed approach

Let the error function be given

$$\mathcal{E} = \mathcal{L}(y_p) - x \quad \rightarrow \quad \mathcal{E} = \coth(y_p) - \frac{1}{y_p} - x\,. \tag{3.81}$$

The linearization of the error function around y reads

$$\text{Lin}\mathcal{E} = \mathcal{E}(y_p) + \left.\frac{d\mathcal{E}}{dy}\right|_{y_p} \Delta y \stackrel{!}{=} 0\,. \tag{3.82}$$

The tangent of the error function with respect to y can be derived as

$$\mathcal{K} = \left.\frac{d\mathcal{E}}{dy}\right|_{y_p} \quad \rightarrow \quad \mathcal{K} = \frac{1}{\sinh^2(y_p)} - \frac{1}{y_p^2}\,. \tag{3.83}$$

Incorporation of (3.83) and (3.81) into the linearized error expression (3.82) , the approximation can be updated

$$y_c = y_p + \Delta y = y_p - \frac{\mathcal{E}}{\mathcal{K}}\,. \tag{3.84}$$

The interval [0,1] is divided equally into 10^4 intervals and the error is calculated for each point except the singular ones. The calculations are repeated for 6 different approximants outlined in Table 3.1. The *elapsed time* is observed after the predictor and the corrector steps. To compare these features, a MATLAB code is compiled and `timeit` function is used to keep record of the run-time. It calls the specified function multiple times and returns the median of the time intervals.

Table 3.1: One-pass predictor-corrector algorithm for e.g. Padé approximation [33].

I. Predictor step	Given: $y_p = x\dfrac{3-x^2}{1-x^2}$
II. Corrector step	
1. Error function	$\mathcal{E} := \coth(y_p) - \dfrac{1}{y_p} - x$
2. Linearization	$\text{Lin}\,\mathcal{E} = \mathcal{E} + \mathcal{K}\Delta y \stackrel{!}{=} 0\,.$
3. Tangent	$\mathcal{K} = \dfrac{1}{\sinh^2(y_p)} - \dfrac{1}{y_p^2}$
4. Solve	$\Delta y = -\dfrac{\mathcal{E}}{\mathcal{K}}$
5. Update	$y_c = y_p - \dfrac{\mathcal{E}}{\mathcal{K}}$

Table 3.2: Approximate rational functions for the inverse Langevin function

Proposed by	Approximant
Cohen [33]	$\mathcal{L}^{-1}(x) = x\dfrac{3-x^2}{1-x^2}$
Treloar [111]	$\mathcal{L}^{-1}(x) = \dfrac{3x}{(1-x^2)(1+0.4x^2+0.2x^4)}$
Puso [100]	$\mathcal{L}^{-1}(x) = \dfrac{3x}{1-x^3}$
Jedynak [65]	$\mathcal{L}^{-1}(x) = \dfrac{3x-2.6x^2+0.7x^3}{(1-x)(1+0.1x)}$
Kröger [73]	$\mathcal{L}^{-1}(x) = \dfrac{3x}{(1-x^2)(1+0.5x^2)}$
Itskov & Darabi [38]	$\mathcal{L}^{-1}(x) = \dfrac{3x-3x^2+x^3}{1-x}$

KRÖGER [73] suggested the term *complexity* defined as the sum of the orders of polynomials in the nominator and denominator for rational functions. In the lights of this claim, one can infer why Treloar [1/6] approach takes more time than Itksov and Darabi [3/1], see Figure 3.2. On the other hand, according to Kröger's complexity definition, Puso approach [1/3] (order 4) is less complex than Cohen approach [3/2] (order 5). However, required time for Puso approach is obviously larger. It shows

that such a definiton is not a persistent way of measuring the computational cost of an approximant. In this work, we pursue with the *elapsed time* instead of *complexity* which is more general allowing comparison of functions of any type. As can be seen from Figure 3.2, elapsed time for corrector step is identical for all approximants as the methodology suggests. For Cohen and Kröger approaches, elapsed time for predictor steps are quite similar and the elapsed time for corrector step is less than half that of predictor step. Moreover, elapsed time for predictor step of the approximants of Puso, Jedynak and Itskov are almost identical and the corrector steps take nearly one fourth of the elapsed time for predictor step. The relative error distributions for the predictor and correctors steps of each approximant are plotted in the range $x \in [0, 1)$ and depicted in Figure 3.3. Maximum relative errors of rational functions are given in

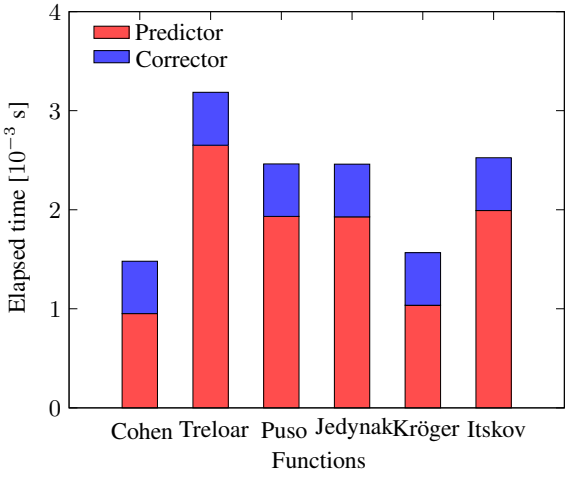

Figure 3.2: Elapsed time for the predictor and corrector steps of the rational approximants to Langevin function.

Table 3.3. Therein, the exact results are obtained by employing 10 Newton-Raphson (NR) iterations to the error expression (3.81). After a few steps, NR iterations lead to the machine tolerance for the error. According to results, the predictor step applied to Cohen's approximant reduces the relative error from 4.937% to 0.240% and still takes less time than initial call of other approaches, such as Treloar, Jedynak, and Itskov & Darabi. Similarly, Kröger approximation performs the best among others both after the predictor ($\mathcal{E}_{\text{rel}} = 1.264\%$) and the corrector steps ($\mathcal{E}_{rel} = 0.016\%$). Kröger approximation is not only the most accurate approximant but also computationally the most feasible approximation. For all approximations, the corrector step reduces

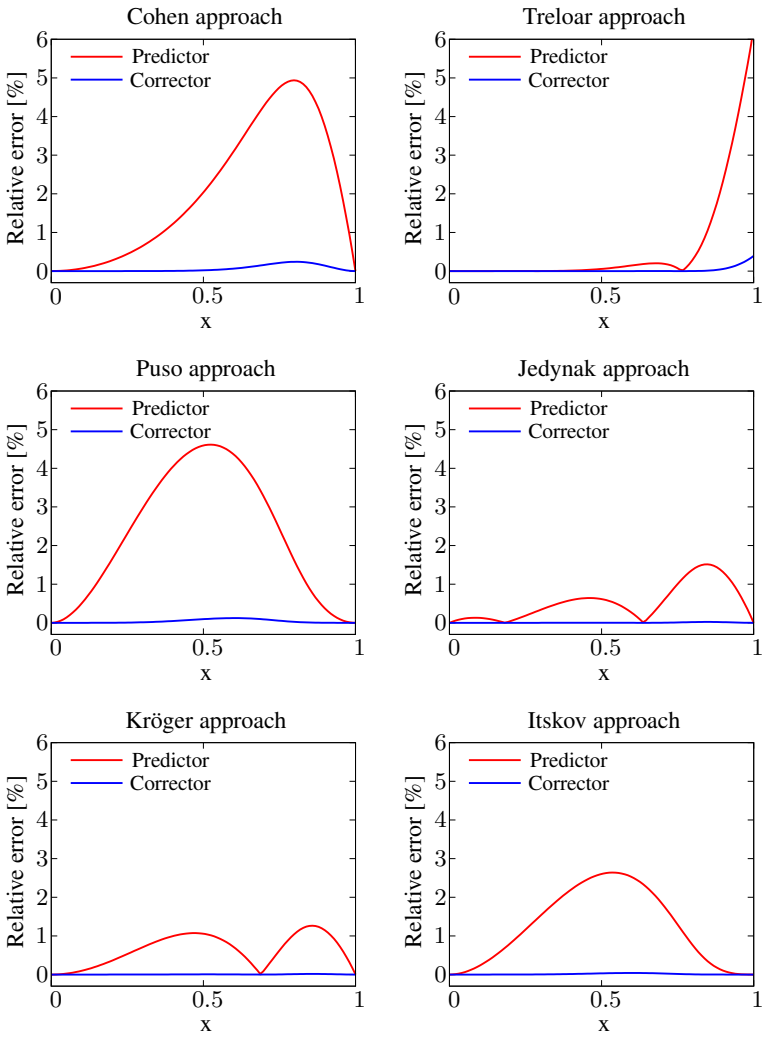

Figure 3.3: Relative errors for the predictor and corrector steps of rational approximants to inverse Langevin function.

the relative error by at least an order of magnitude, see Table 3.2.

Besides the rational functions given in Table 3.1, 4 different functions which were proposed by Morovati et al. [95] are investigated as a second set of examples. In a similar way, max relative error and elapsed time for each function are calculated and presented in Table 3.3 and Figure 3.4. Approximants #1 and #2 are constructed on the modified version of Warner approach ($\frac{2y}{1-y^2}$). On the other hand, approximants #3 and #4 are produced by taking a trigonometric function as a basis function ($\frac{\pi}{2}\tan(\frac{\pi}{2}y)$) and adding power series terms to reduce the relative error. Both main functions are odd, have simple poles at $y = \pm 1$ and a residue of -1. Thus, the second set of ap-

Table 3.3: Relative errors for the predictor and corrector steps of rational approximants to inverse Langevin function.

	Max relative error [%]	
Approach	Predictor	Corrector
Cohen	4.937	0.240
Treloar	6.250	0.391
Puso	4.612	0.122
Jedynak	1.513	0.023
Kröger	1.264	0.016
Itskov & Darabi	2.639	0.041

proximants exhibit asymptotic behavior similar to the inverse Langevin function. For further discussion on the features of admissible approximants for inverse Langevin function, we refer to KRÖGER [73].

To show the effectiveness of the proposed approach, it is applied to approximants

Table 3.4: Relative errors of approximate functions at predictor and corrector steps

2*Function type	Max relative error [%]	
	Predictor	Corrector
Warner-like functions [95]		
1) $\frac{2y}{1-y^2} + y - \frac{y^3}{5}$	2.90	0.084
2) $\frac{2y}{1-y^2} + y - \frac{y^3}{5} - \frac{53y^5}{175} - 0.16y^7$	0.41	-
Trigonometric functions [95]		
3) $\frac{\pi}{2}\tan(\frac{\pi}{2}y) + 0.53y - 0.23y^3$	2.92	0.085
4) $\frac{\pi}{2}\tan(\frac{\pi}{2}y) + 0.53y - 0.23y^3 - 0.31y^5 - 0.14y^7$	0.35	-

#1 and #3, then maximum relative error of predicor and corrector steps are calculated. The approximants #2 and #4 are already proposed as improvement to #1 and

#3. Therefore the corrector step of our approach is compared to the additional terms added by MOROVATI ET AL. [95] in order to compare its efficiency. Hence, the corrector step is not applied to approximants #2 and #4 as the main idea behind the our idea is to use relatively simpler expressions as predictors. The improvement of our approach can be clearly seen from the maximum relative errors reported in Table 3.3. Maximum relative error for approximant #1 reduces from 2.90% to 0.084% in the predictor step whereas the correction term added in #2 reduces the maximum relative error to 0.41%. Although the approximant #2 has a series expansion up to seventh order term, the maximum relative error resulting from the predictor step is about one fifth of the approximant #2. Furthermore, the additional computational cost of the corrector step is less than half that of #2, see Figure 3.4. Similar trend is observed

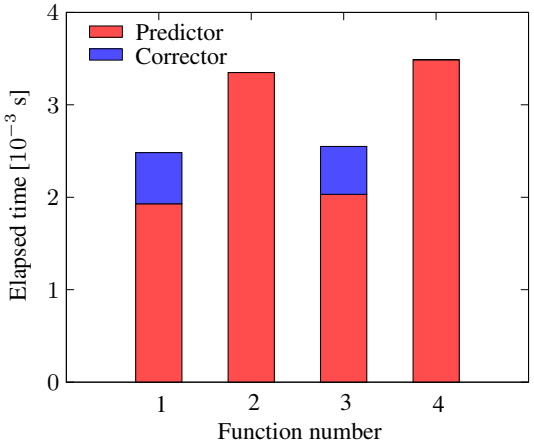

Figure 3.4: Elapsed time for the approximants from Morovati et al. [95] and the proposed predictor-corrector algorithm.

as the one-pass predictor-corrector algorithm is applied to approximant #3 and compared to #4. Maximum relative error for approximant #3 decreases to 0.085% after corrector step whereas the the approximant #4 leads 0.35% maximum relative error. As the the predictor-corrector algorithm is used to improve approximant #3, the additional computational cost considerably less than that of #4, which also is used to improve #3 with additional polynomial terms, see Figure 3.4.

3.6.2 Representative example: Rubber elasticity

In this section, the proposed approximant is applied for the computation of the inverse Langevin function in rubber elasticity. Our aim is to assess (i) the quality of the ap-

proximant on the fitting performance of the constitutive model and (ii) the sensitivity of model parameters on the approximant. We choose the Cohen's approximant as the predictor. The particular reason for this choice is its wide use of Cohen's approximant $\mathcal{L}^{-1}(x) = x\frac{3-x^2}{1-x^2}$ in rubber elasticity [35]. To this end, eight-chain model [15] and the extended eight-chain model [36] are investigated with respect to the experimental dataset of TRELOAR [112]. The eight-chain model is derived based on the non-Gaussian Langevin statistics of an ideal, freely jointed phantom chains that can pass freely through their neighbouring chains so that, effect of constrained junctions and entanglements are neglected. This fact manifests itself in terms of underestimated stress-strain response under biaxial deformation states in the Gaussian-region. The extended eight-chain model incorporates a tube-like constraint that accounts for the entanglements restricting the free-motion of the chains. This is achieved in terms of an areal stretch based constraint free energy function. Both models are based on the first and second invariants. In this regard, the stress expressions under uniaxial (UT), equibiaxial (ET) and pure shear (PS) deformations read

$$\begin{aligned}
\text{(UT)} \qquad P_1 &= 2(c_1 + \frac{c_2}{\lambda})(\lambda - \frac{1}{\lambda^2}) \\
\text{(ET)} \qquad P_1 &= 2(c_1 + c_2\lambda^2)(\lambda - \frac{1}{\lambda^5}) \\
\text{(PS)} \qquad P_1 &= 2(c_1 + c_2)(\lambda - \frac{1}{\lambda^3})
\end{aligned} \tag{3.85}$$

with

$$c_1 = \frac{\partial \psi}{\partial I_1} \quad \text{and} \qquad c_2 = \frac{\partial \psi}{\partial I_2}\,. \tag{3.86}$$

For the extended eight-chain model, the partial derivatives are

$$c_1 = \frac{\mu}{6}\frac{\mathcal{L}^{-1}(\lambda_r)}{\lambda_r} \quad \text{and} \quad c_2 = \frac{1}{9}\frac{\mu_c}{\nu_c^2}\,. \tag{3.87}$$

Herein, the average network stretch, the relative average network stretch and the average areal network stretches are, respectively,

$$\lambda_n = \sqrt{\frac{\lambda_1^2 + \lambda_2^2 + \lambda_3^2}{3}} = \sqrt{\frac{I_1}{3}}\,, \quad \lambda_r = \frac{\lambda_n}{\sqrt{N}} \tag{3.88}$$

and

$$\nu_n = \sqrt[3]{\frac{\nu_1^2 + \nu_2^2 + \nu_3^2}{3}} = \sqrt[3]{\frac{I_2}{3}}\,. \tag{3.89}$$

The λ_i^2 and ν_i^2 are the eigenvalues of the right Cauchy-Green tensor $\boldsymbol{C}$ and its cofactor $\mathrm{cof}\,\boldsymbol{C}$, respectively. The model parameters μ, N, and μ_c are the shear modulus,

segment number and tube-constraint parameter, respectively. The model recovers the eight-chain model for $c_1 = 0$ or $\mu_c = 0$. In both investigations, the parameter identification procedure outlined in DAL ET AL. [35] is utilized and the model parameters of the eight-chain model is obtained for the cases: (i) Cohen's approximant used for the inverse Langevin function and (ii) corrector scheme applied to the Cohen's approximant used as predictor. In short, the cost function is defined as

$$\mathcal{E}_{\text{TOT}}(\boldsymbol{\zeta}, \boldsymbol{w}) = w_1 \mathcal{E}_{\text{UT}} + w_2 \mathcal{E}_{\text{ET}} + w_3 \mathcal{E}_{\text{PS}} \,, \tag{3.90}$$

where error expression for uniaxial, equibiaxial and pure shear experiments read

$$\mathcal{E}_k(\boldsymbol{\zeta}) = \sum_{i=1}^{n_k} (P_{11}(\boldsymbol{\zeta}, \lambda_i) - P_{11}^{\text{exp}}(\lambda_i))^2 \tag{3.91}$$

with $k = \{\text{UT}, \text{ET}, \text{PS}\}$. w_1, w_2, w_3 are the associated weight factors.

Table 3.5: Optimized model parameters and relative stretch range for eight-chain model obtained for UT dataset of Treloar: (i) Cohen's approximant (predictor) and (ii) one-pass corrector term.

Eight-chain model	μ [MPa]	N	$\lambda_r \in [\text{min} \,,\, \text{max}]$
Cohen's approximant [33]	0.2672	25.5927	[0.1977 , 0.8693]
Predictor-corrector	0.2782	25.5108	[0.1980 , 0.8707]

Table 3.6: The quality of fit values obtained from the parameter identification process for the eight-chain model: (i) Cohen's approximant (predictor) and (ii) one-pass corrector term.

	Quality of fit			
Eight-chain model	Total	Region 1	Region 2	Region 3
Cohen's approximant [33]	0.2468	0.0756	0.0809	0.0930
Predictor-corrrector	0.2010	0.567	0.0644	0.0799

In the first example, the eight-chain model parameters are obtained from the UT dataset of Treloar. The material parameters obtained from fitting process are outlined

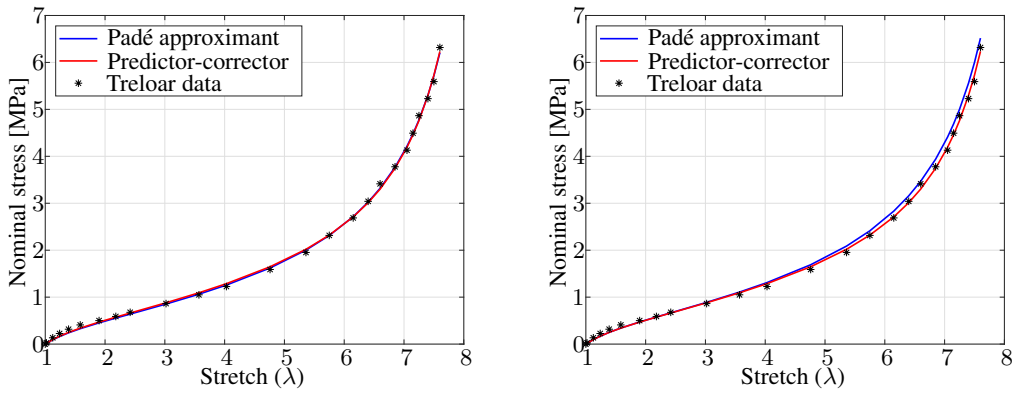

Figure 3.5: Predictions of eight chain model with (i) Padé approximant and (ii) one-pass predictor-corrector algorithm employed for the inverse Langevin function: The parameters are fitted to the uniaxial tension experiment of Treloar: (left) The eight-chain model parameters $\mu = 0.2672$ & $N = 25.5927$ (Padé approximant) and $\mu = 0.2782$ & $N = 25.5108$ (predictor-corrector algorithm) are identified. (right) Parameters $\mu = 0.2782$ & $N = 25.5108$ are taken identical for comparison.

in Table 3.5. Model parameters change slightly as the Padé approximant is replaced with the corrector term during the parameter identification. To express the agreement between the model prediction and the experimental data in a comprehensive manner, the *quality of fit* expressions for both cases are tabulated for three regions of deformation in Table 3.6, see also DAL ET AL. [35] The inverse Langevin function enters the stress expression as a function of the relative stretch $\lambda_r = \lambda_n/\sqrt{N}$ which varies in between $\lambda_r \in [0.19, 0.88]$ during the uniaxial tension test, see Table 3.7. This value varies slightly according to the variations in segment number N as the Padé approximation is replaced with the correcter term. It is shown that one-pass predictor-corrector step improves the fitting quality marginally. On the other hand, a more noticeable change is observed in the identified paramters. The initial shear modulus is about 4.12% higher when the predictor-corrector scheme is employed, see Figure 3.5(left). In order to assess the variation in model prediction when Padé approximation is replaced with the predictor-corrector scheme for fixed model parameters, the stress-stretch results for the uniaxial tensile deformations for the eight-chain model are plotted for the two cases, see Figure 3.5(right). The model parameters for two cases are $\mu = 0.2782$ & $N = 25.5108$. The nominal stresses obtained with Padé approximation slightly overshoot the values obtained from the predictor-

corrector scheme in the non-Gaussian region and the gap decreases towards the chain extensibility limit. However, it is possible to improve the quality of fit of the estimates obtained from Padé approximation by modifying the material parameters of the eight-chain model.

In the second example, the proposed predictor-corrector scheme is embedded into extended eight-chain model [36] and new model parameter sets are computed for simultaneous fitting of UT+ET+PS dataset of Treloar. The fitted curves for both approaches are illustrated in Figure 3.6. The identified material parameters, and the quality of fit results for the (i) Padé approximant and (ii) predictor-correcter scheme based computations are outlined in Table 3.7 and Table 3.8, respectively. It is observed that quality of fit decreases slighlty after switching from Padé approximant to the predictor-correcter scheme. The difference between the identified shear moduli μ and μ_c are 4.4%, 5.2%, respectively. Although the difference between the identified shear moduli parameters are more pronounced in each case, the effective shear modulus $\mu_{\text{eff}} = \mu + 4/9\mu_c = 0.471$ in the former and $\mu_{\text{eff}} = 0.472$ for the latter case. The difference between the identified segment numbers N is less than 0.2%.

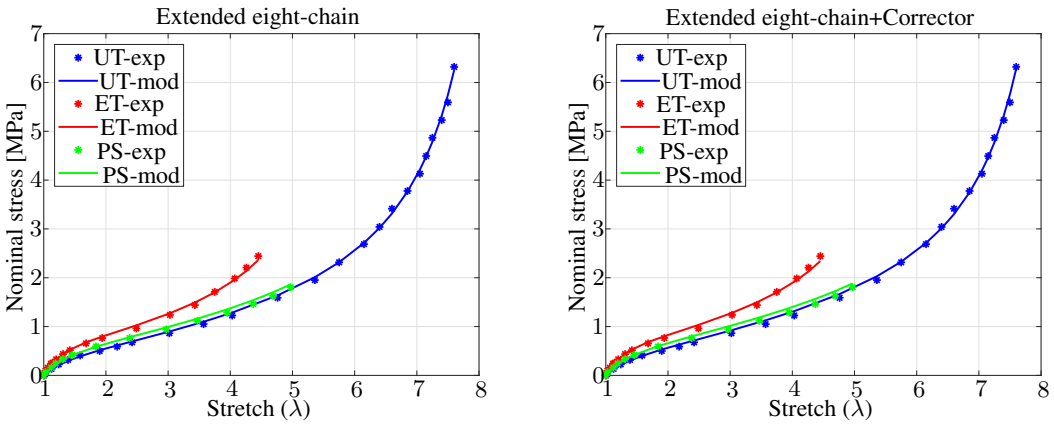

Figure 3.6: Predictions of extended eight-chain model and its modified version with one-pass predictor-corrector algorithm for combination of uniaxial, equibiaxial, and pure shear loadings using Treloar data.

Table 3.7: The material parameters, relative stretch range, and the quality of fit values obtained from the parameter identification process for the extended eight-chain model with Padé approximation.

Material parameters	$\mu = 0.2614$	$N = 25.3775$	$\mu_c = 0.4715$	
Relative stretch		UT	ET	PS
$\lambda_r^{\min}$		0.1985	0.1985	0.1985
$\lambda_r^{\max}$		0.8730	0.7213	0.5815

		Quality of fit			
	Weight	Total	Region 1	Region 2	Region 3
UT	0.1	0.0526	0.0070	0.0154	0.0302
ET	0.8	0.0849	0.0216	0.0278	0.0355
PS	0.1	0.0526	0.0118	0.0123	0.0285
Total	1.0	0.1902	0.0404	0.0555	0.0943

Table 3.8: The material parameters, relative stretch range, and the quality of fit values obtained from the parameter identification process for the extended eight-chain model with predictor-corrector scheme.

Material parameters	$\mu = 0.2730$	$N = 25.3308$	$\mu_c = 0.4470$	
Relative stretch		UT	ET	PS
$\lambda_r^{\min}$		0.1987	0.1987	0.1987
$\lambda_r^{\max}$		0.8738	0.7219	0.5820

		Quality of fit			
	Weight	Total	Region 1	Region 2	Region 3
UT	0.1	0.0858	0.0079	0.0302	0.0477
ET	0.8	0.0871	0.0197	0.0281	0.0393
PS	0.1	0.0651	0.0102	0.0118	0.0431
Total	1.0	0.2380	0.0378	0.0701	0.1301

CHAPTER 4

REPRESENTATIVE NUMERICAL EXAMPLES

The theoretical framework proposed in Chapter 3, have been implemented into FEAP developed by TAYLOR [106]. Modeling capacity of the employed approach is assesed by matchting between experimental data in the literature and simulation results. In Section 4.1, only mechano-fracture is investigated for a complex geometry in order to show model sensitivity, i.e thermal field is not solved. Then, beside uniaxial compression tests under various temperature with constant strain rate, uniaxial tension tests under room temperature with several strain rate are considered to assign material parameters of PMMA. Once parameter identification process is done, then coupled thermo-mechanic fracture problem is simulated for a complex geometry under different strain rates and temperature values to emphasize the modeling ability of transition in between ductile-brittle fracture.

4.1 Tensile test on a double notched specimen

A benchmark example has been performed in order to assess the sensitivity of the computations with regard to various fracture parameters under shear yielding and crazing induced failure and to assess the ability of the numerical model to capture complex crack patterns. Motivated by the blanking process, a problem geometry with two asymmetrically placed rounded notches is used as originally proposed by [28]. We also refer to the investigations carried out on the same geometry by [1, 81] for ductile and porous plasticity of metals. The bottom and right boundaries remain fixed, and the specimen is driven by $\hat{u}(t) = vt$ on the left and top boundary, see Figure 4.1(a). The tip velocity is taken as $v = 6$ [mm/s]. The left edge is fixed against horizontal motion. The sensitivity analysis is based on various combinations of $\bar{v}$, $\bar{\alpha}$

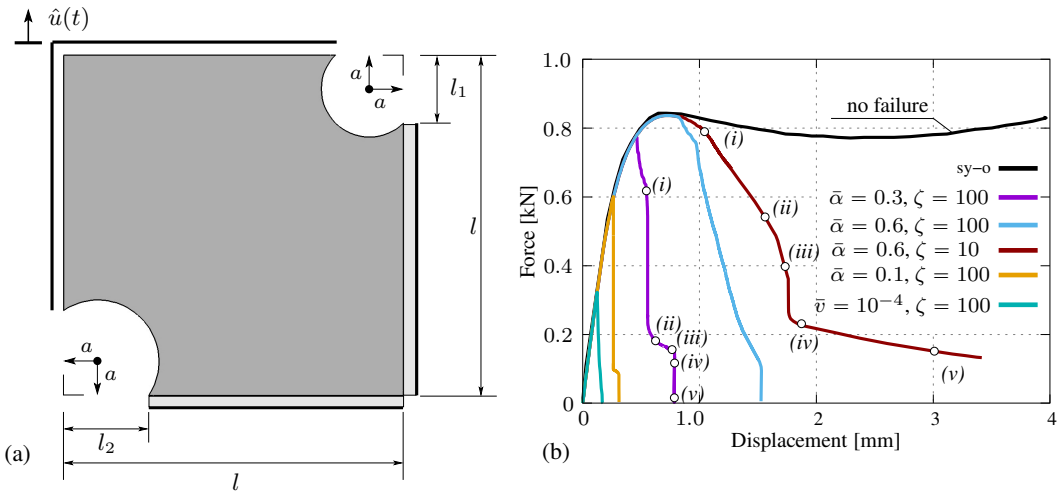

Figure 4.1: (a) Geometry and boundary conditions for tensile test on double notched square specimen. The dimensions of the geometry are, $l_1 = 2$mm, $l_2 = 2.5$mm, $a = 1$mm, $l = 10$ mm, respectively. (b) Brittle-to-ductile failure due to shear yielding: Force-displacement curves for various $\{\bar{\alpha}, \zeta\}$ parameters.The parameter set $\bar{v} = 10^{-4}$, $\zeta = 100$ refers to the brittle failure due to crazing. All other simulations are carried out for shear yielding dominated failure where the craze switch is off.

and ζ. The rest of the material parameters can be found in [37].

The IBVP is solved for various scenarios. The limit viscoplastic shear-yielding behaviour is depicted with black curve where the craze switch and crack initiation criteria are suppressed, see Figure 4.1(b). Then, various combinations of $\bar{\alpha}$ that controls the damage initiation in terms of equivalent plastic strain can be observed. Increasing the value $\bar{\alpha}$ delays the crack initiation. For a constant value of $\bar{\alpha} = 0.6$ two different values of ζ clearly demonstrate that the lower value of ζ promotes a more ductile failure pattern as it creates a larger domain of plastic region in the crack process zone, see Figure 4.4. In Figure 4.2, various snapshots which correspond to the points (i)-(v) on Figure 4.1(b) for the parameter set $\bar{\alpha} = 0.3$, $\zeta = 100$ are depicted for a relatively more brittle and premature failure. The snapshots are also marked in Figure 4.1(b). On the other hand, 4.3 shows the same simulation repeated for $\bar{\alpha} = 0.6$, $\zeta = 10$ as an example for ductile failure. In this scenario, the material is extremely ductile and the specimen could not be totally broken since the damage variable d evolves slowly. The simulation terminated due to extreme mesh distortion around degraded elements.

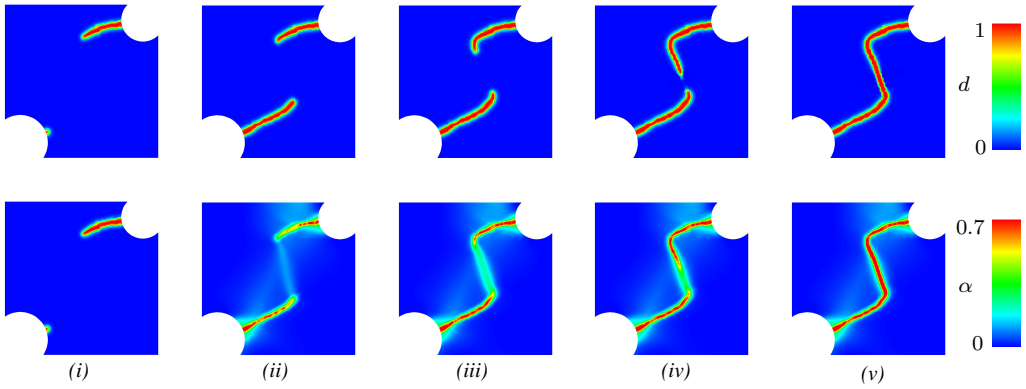

Figure 4.2: Brittle fracture due to shear yielding: Snapshots of damage field d and equivalent plastic strain α at various stages for $\bar{\alpha} = 0.3$, $\zeta = 100$.

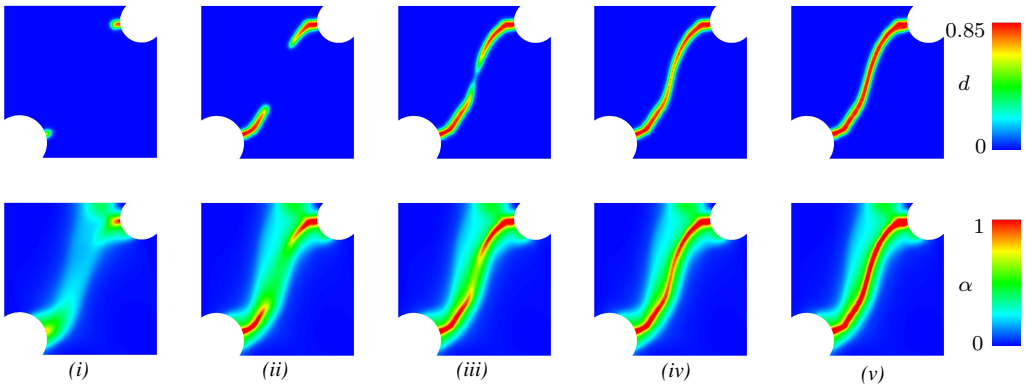

Figure 4.3: Ductile fracture due to shear yielding: Snapshots of damage field d and equivalent plastic strain α at various stages for $\bar{\alpha} = 0.6$, $\zeta = 10$.

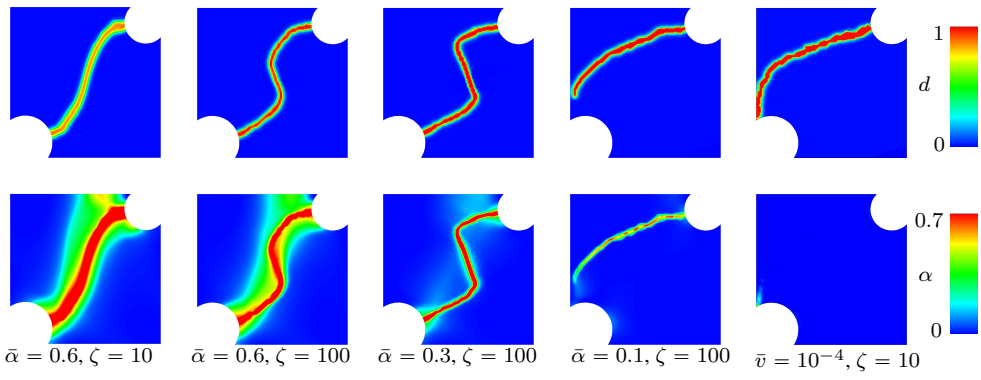

Figure 4.4: The final snapshots of simulations corresponding to five different scenarios.

Comparison of both figures clearly demonstrates the role of the damage growth parameter ζ on the ductility of the material during crack propagation. In order to demonstrate the difference in shear yielding and crazing dominated failure the craze switch function F_c is reactivated and material parameters $\bar{v} = 10^{-4}$ is taken. This choice leads to nearly identical stress-strain curve and onset of damage to the case $\bar{\alpha} = 0.1$ at material level. However, comparison of the load-displacement curves in Figure 4.1(b) clearly demonstrates that crazing induced failure is considerably more brittle compared to the shear yielding dominated failure. For crazing-dominated failure scenario, the one observe no significant amount of plastic deformation. The final snapshots of simulations corresponding to five different scenarios are depicted in Figure 4.4. For higher $\bar{\alpha}$ value,material shows more ductile behavior and crack growths like in S-shape between doublenotches. However, material behavior become more brittle and crack pattern sraightens, as $\bar{\alpha}$ value decreases.

4.2 Uniaxial compression behavior

In this section, we investigate uniaxial compression behaviour of proposed consitutive model. ARRUDA ET AL. [16] conducted uniaxial compression experiments on PMMA at $25°$C, $50°$C and $75°$C with true strain rate $\dot{\varepsilon} = 10^{-3}\ [1/s]$ under isothermal condition in order to observe the temperature effect on stress-strain response. As the test results show shear-yielding dominant behavior, these tests are considered to assign parameters related to shear yielding. In order to calibrate these parameters, three simulations are performed under same conditions with experiments and are fitted on those experiments simultaneously as shown in Figure 4.5. Notice that linear pre-yield regime and post-yield thermal softening are well captured quantitatively and qualitatively. Obtained parameters are kept constant for rest of the simulations.

4.3 Uniaxial tension behavior

In the sequel, uniaxial tension tests conducted by JIANG ET AL. [67] are considered to understand strain rate effect on the craze initiation of PMMA and to assign the crazing-related parameters of the proposed model. Response of uniaxial tension tests under three different strain level are provided in Figure 4.6 with corresponding finite element analysis. Clearly seen that stress level at craze initiation increases with

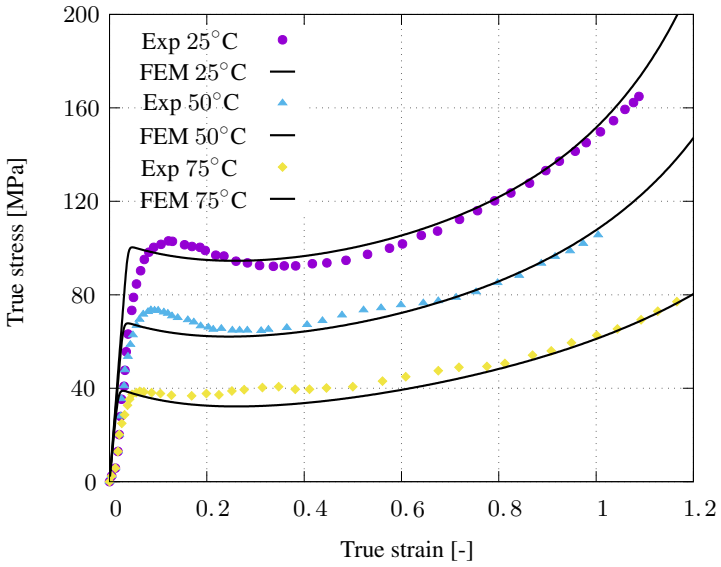

Figure 4.5: Isothermal simulations at a material point under uniaxial compression

increasing strain rate and this agrees with experimental observation of HAWARD ET AL. [55]. Shear-yielding related parameters obtained from uniaxial compression tests are fixed and only crazing related parameters are adjusted while finite elements simulations are running simultaneously until sufficient agreement is satisfied. At low strain rate levels, proposed approach captures the behaviour of PMMA under uniaxial tension reasonably. On the other hand, at high strain level simulation result shows poor agreement with experiment.

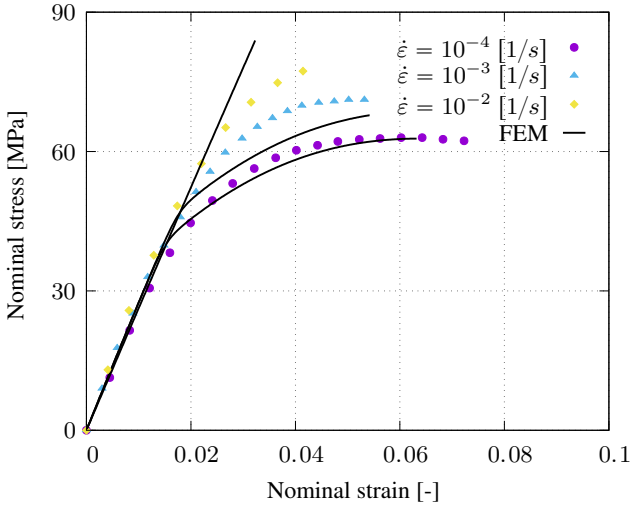

Figure 4.6: Uniaxial tension test data and FEM analysis under different strain rates

Table 4.1: Material & model parameters associated with thermo-viscoplasticity, crazing and crack phase–field.

Par.	Description	Value	Unit	Par.	Description	Value	Unit
κ	Eq. (3.45)	2500	MPa	h_2	Eq. (3.31)	100	-
μ_0	Eq. (3.47)	1005	MPa	s_{cr}	Eq. (3.32)	200	MPa
c_s	Eq. (3.47)	0.0040	-	m	Eq. (3.32)	2	-
B	Eq. (3.53)	4.08×10^{18}	mm^{-3}	$\dot{\gamma}_0^c$	Eq. (3.32)	10	s^{-1}
D	Eq. (3.53)	5.54×10^{21}	mm^{-3}	v_f^{ss}	Eq. (3.31)	3×10^{-4}	-
E_d	Eq. (3.53)	23.43×10^6	Nmm/mol	h_3	Eq. (3.34)	9×10^{-3}	-
$\hat{N}^p(\theta_r)$	Eq. (3.55)	2.7	-	$\hat{c}_1(\theta_r)$	Eq. (3.65)	12.96	MPa
$\hat{n}^p(\theta_r)$	Eq. (3.55)	3.67×10^{18}	mm^{-3}	$\hat{c}_2(\theta_r)$	Eq. (3.65)	728.14	MPa^2
$\dot{\gamma}_0^p$	Eq. (3.27)	2.8×10^7	s^{-1}	$\mathcal{Q}_1$	Eq. (3.65)	375.76	Nmm
A	Eq. (3.27)	100.6	K/MPa	$\mathcal{Q}_2$	Eq. (3.65)	433.16	Nmm
ϱ	Eq. (3.28)	0.2	-	l	Eq. (3.36)	$2 \times h_{min}$	mm
θ_r	Eq. (3.45)	296	K	η	Eq. (3.36)	1×10^{-4}	MPa . s
h_1	Eq. (3.30)	315	MPa	ζ	Eq. (3.67)	1	-
s_0	Eq. (3.30)	138	MPa	$\bar{v}_f$	Eq. (3.67)	0.03	-
s_{ss}	Eq. (3.31)	114.45	MPa	$\bar{\alpha}$	Eq. (3.67)	0.9	-

These tests being conducted over a span of more than 20 years by different research teams following different test protocols, and the fact that the materials they used, although they tested PMMA, were supplied by different vendors, makes it challenging to calibrate the proposed model and determine a unique set of parameters specifically for PMMA.

Table 4.1 indicates the list of the material and model parameters used in following example. Recall that the thermo-viscoplastic parameters are obtained from the uniaxial compression tests by ARRUDA ET AL. [16] and parameters related to crazing calibrated based on the those identified by JIANG ET AL. [67]. The parameters for crack-phase field are adjusted according to work of MIEHE ET AL. [92]. Finally, critical plastic strain and void volume fraction values inheretly appear in local evaluation of crack phase field are directly taken from DAL ET AL. [37].

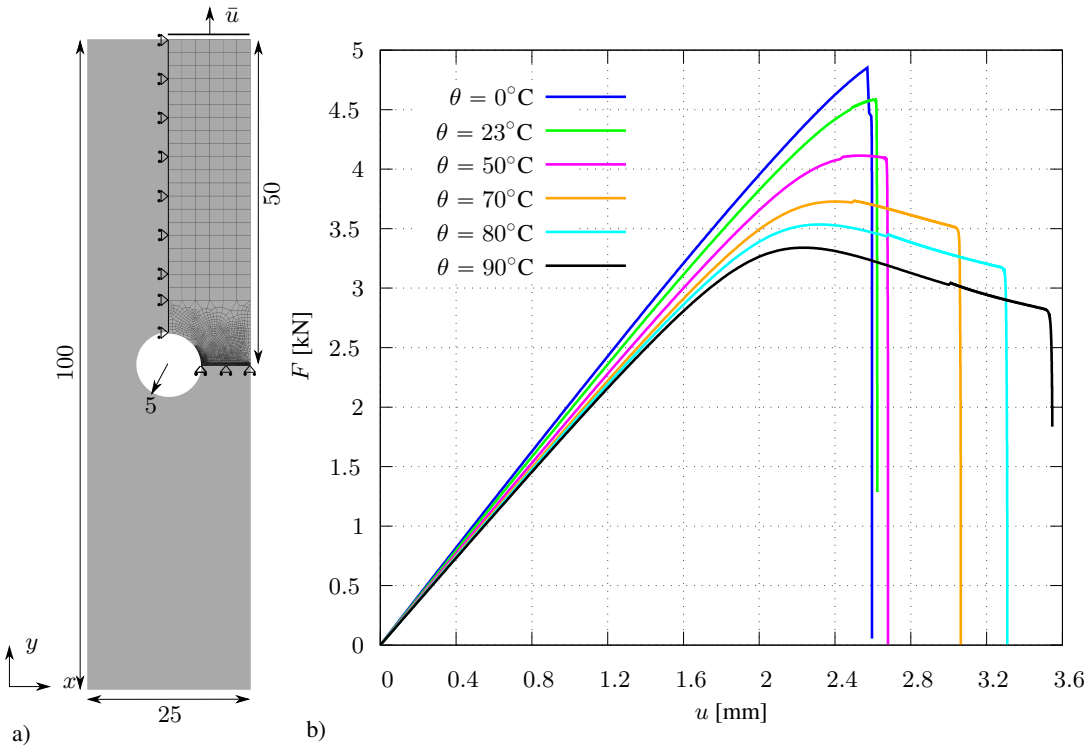

Figure 4.7: (a) Rectangular specimen with a circular hole located in the middle of the solid subjected to tension. One quadrant of the domain is discretized due to symmetries associated with x– and y–axis. Given also are the appropriate boundary and loading conditions. All dimensions are in [mm]. (b) Force–displacement curves resulting from simulations carried out at temperatures $\theta = \{0°, 23°, 50°, 70°, 80°, 90°\}$ [C], corresponding to blue, green, magenta, orange, cyan and black solid lines, respectively.

4.4 Brittle to ductile transition due to homogeneous temperature rise under uniaxial tension

This example investigates the transition of brittle mechanical response into ductile one for glassy polymers as the temperature gradually rises from 273 K (0° C) to the nearly glass–transition temperature 363 K (90° C) for each simulation of a uniaxial extension test. To this end, a replica of the experimental test setup given in JIANG ET AL. [67] is created. The geometry is composed of a rectangular PMMA plate with a circular hole located in the middle of the geometry, see Fig. 4.7(a). However, only one quadrant of the entire domain is modeled thanks to the symmetry with respect to x– and y–axis. The finite element mesh generated involves 3027 4–node Q1P0 elements

connected by 3154 nodes. Besides, regions where the crack growth is expected are refined with the minimum mesh size $h_{min} = 0.0625$ [mm]. Considering apposite boundary conditions for a plane–strain case, the displacement–driven loading $\bar{u}$ is applied on the upper edge along y–direction at the rate $\dot{u} = 5 \times 10^{-2}$ [mm/s], ensuring isothermal conditions with the temperature value being uniform all over the solid. Therefore, it should be underlined that the coupled thermo-mechanical effects are entirely neglected for this example.

Fig. 4.7(b) show the force–displacement curves in regard to various simulations performed at distinct temperature levels, i.e. blue, green, magenta, orange, cyan and black solid lines correspond to $\theta = \{0^\circ, 23^\circ, 50^\circ, 70^\circ, 80^\circ, 90^\circ\}$ [C], respectively. Clear manifestation of brittle to ductile transition of failure can be observed. While the mechanical response of the glassy polymer is palpably brittle when far away from the glass transition temperature, e.g., the blue solid line indicating the result at $\theta = 0^\circ$ C, ductility gradually builds up with the yield stress significantly lowered under elevated temperatures close the glass transition temperature, see, e.g., the cyan and black solid lines corresponding to $\theta = 80^\circ$ C and $\theta = 90^\circ$ C, respectively. Upon a closer look, the drop in the shear modulus, see (3.47), due to temperature increase is discernible which is accompanied by substantial drop of the yield point at which the peak stress level is reached. Such a decrease in the yield stress is explained by the increase in the value of the scalar flow function $\dot{\gamma}^p$, see (3.27), for elevated temperatures where $\tilde{\sigma}^p < \tilde{s}$. The immediate effect of this increase in $\dot{\gamma}^p$ is seen in the evolution of the athermal shear strength such that the right hand side of (3.30) grows in magnitude, assuming a greater negative value since $s > s_s(v_f)$ before yielding. As a result, the value of the athermal shear strength s and therefore its effective value $\tilde{s}$ are reduced at that particular strain, thereby diminishing the yield stress level.

Figure 4.8(a) illustrates the evolution of the crack phase-field d, the void volume fraction v_f , and the equivalent plastic strain α under the temperature $\theta = 0^\circ$ C at three instants where (I) the craze initiates, (II) the crack grows, and finally (III) the ultimate failure takes place. Note that the finite elements where $d \geqslant 0.9$ are blanked for the sake of visuality. The polymer initially exhibits a viscoplastic response with a small plastically deformed region subjected to shear yielding around the two sides of the circular hole as indicated by the equivalent plastic strain α. Afterwards, the

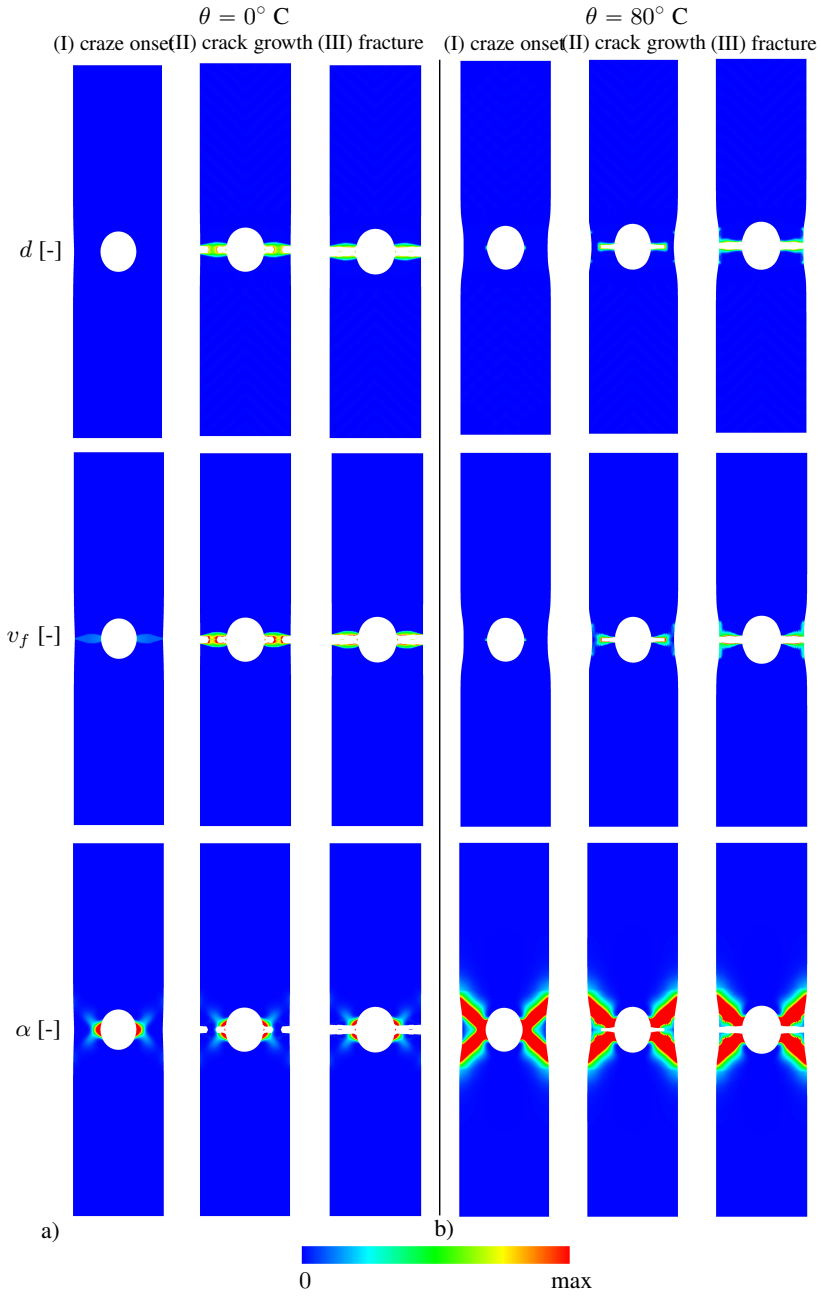

Figure 4.8: Contour plots of the crack phase-field d in relation to void volume fraction v_f and the equivalent plastic strain α under the tensile loading at (a) $\theta = 0^\circ$ C at the instants (I) the onset of crazing, (II) during crack growth, and (III) when the rupture takes place; (b) $\theta = 80^\circ$ C at the instants (I) the initiation of cracking, (II) the onset of crazing, (II) during crack growth, and (III) when the fracture occurs. Note that max $\in \{1, 0.1, 0.1\}$ for d, v_f, and α, respectively. For visual purposes, elements where $d \geqslant 0.9$ are blanked.

viscoplastic flow is terminated in regions subjected to crazing which, in fact, commences at the entire mid–plane of the specimen marked by the void volume fraction v_f greater than v_f^{ss}. During the evolution of the crack phase–field d, both the void volume fraction v_f and the equivalent plastic strain α contribute to the crack growth, see (3.67). Nevertheless, it is the crazing that is dominant during the fracture process for the test conducted at $\theta = 0^\circ$ C. The maximum values v_f and α attain during the simulation are 0.67 and 0.18, respectively.

In fact, the crack grows from not only the inner circular hole but also the outer edges at the mid–plane following the voids that are merged together. Finally, the ultimate failure takes place breaking the specimen into two pieces.

Figure 4.8(b) depicts the state of the crack phase-field d, the void volume fraction v_f , and the equivalent plastic strain α for the under the temperature $\theta = 80^\circ$ C at three instants where (I) the crazes initiate, (II) the crack propagates, and finally (III) the rupture occurs. For visual purposes, elements where $d \geqslant 0.9$ are blanked here as well. In contrast to Fig. 4.8(a), a much larger full-fledged shear band around the circular hole is evident until crazes initiate. Upon the onset of crazing, however, the development of shear band is impeded in regions where crazes initiate. During the crack growth, shear yielding takes more precedence over crazing even though both void volume fraction v_f and the equivalent plastic strain α contribute to the cracking phenomenon. The maximum values that v_f and α attain in this case are 0.78 and 0.79, respectively. Later, the crack propagates at the intersection of the circular hole and the mid–plane following the voids that are merged together, leading to complete fracture of the polymer.

4.5 Ductile to brittle transition due to increase in loading rate under uniaxial tension

This example demonstrates how the ductile failure behavior changes into a brittle one upon increasing the loading rate from $\dot{u} = 1$ [mm/min] to $\dot{u} = 100$ [mm/min] along with the associated heating in the solid due to the local dissipation $\mathcal{D}_{loc}^{red}$ of the energy in terms of heat. Therefore, the numerical solution features the coupled thermo-mechanical effects with fracture. As for the geometrical setup, we generate

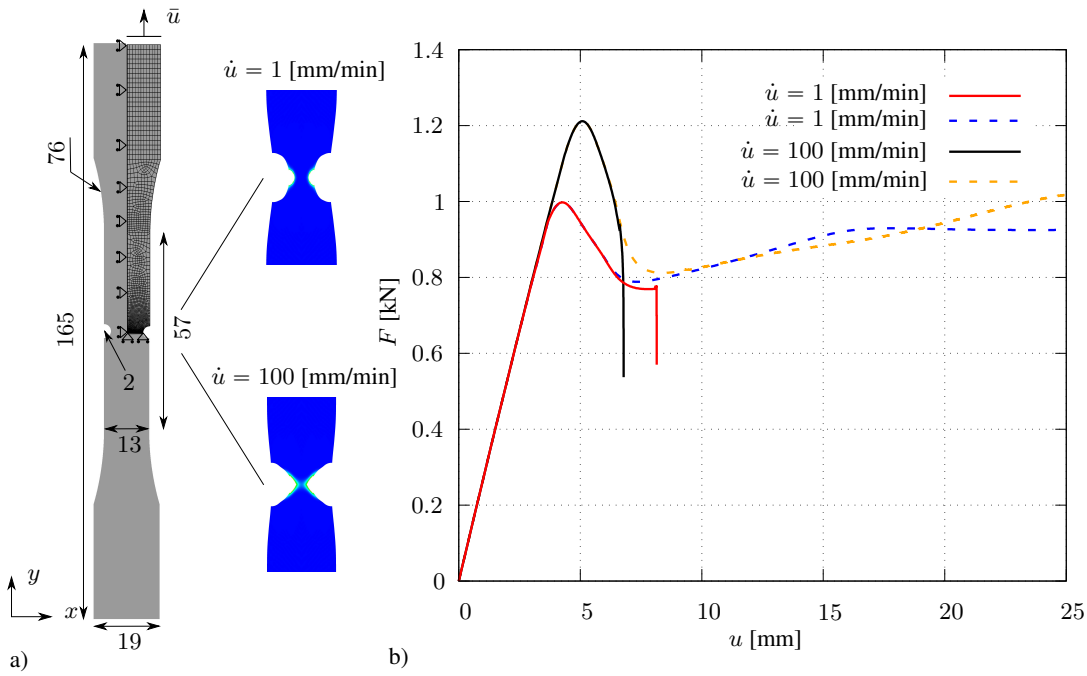

Figure 4.9: (a) Dumbbell–shaped specimen with two symmetrically applied radial notches ($r = 2[mm]$) located in the middle of the geometry subjected to tension. One quadrant of the domain is discretized due to symmetries associated with x– and y–axis along with the appropriate boundary and loading conditions. Given also are the contour plots of the final state of d for $\dot{u} = 1$ [mm/min] and $\dot{u} = 100$ [mm/min] in the area of interest. For visual purposes, elements where $d \geqslant 0.9$ are blanked. All dimensions are in [mm]. (b) Force–displacement curves emanating from the thermo–mechano–fracture analyses such that red and black solid lines corresponding to $\dot{u} = 1$ [mm/min] and $\dot{u} = 100$ [mm/min], respectively. Also shown are the thermo-viscoplastic analyses alone with crazing being suppressed in blue and orange dashed lines for $\dot{u} = 1$ [mm/min] and $\dot{u} = 100$ [mm/min], respectively.

a dumbbell–shaped solid domain in accordance with ASTM D638–14 TYPE I [34] with the addition of a 2–mm–radius notch applied symmetrically in the middle of the specimen as shown in Fig. 4.9(a). The symmetrical layout of the geometry permits the modeling of only one quadrant of the entire domain and generate a finite element mesh composed of 1935 4–node Q1P0 elements connected by 2081 nodes. Regions where the crack propagation is expected are refined with the minimum mesh size $h_{min} = 0.075$ [mm]. Appropriate boundary conditions are applied to avoid rigid body motion for a plane–strain case. The displacement–driven loading $\bar{u}$ is applied

on the upper edge along y–direction at loading rates $\dot{u} = 1$ [mm/min] and $\dot{u} = 100$ [mm/min].

Table 4.2: Material parameters associated with the incorporated temperature field.

Par.	Description	Value	Unit	Par.	Description	Value	Unit
c	Eq. (3.41)	1.46	J g^{-1} K^{-1}	k	Eq. (3.68)	0.192	W m^{-1} K^{-1}
α_T	Eq. (3.45)	8.4×10^{-5}	K^{-1}	h_c	Eq. (3.74)	0.01	W K^{-1}

Purely thermal material parameters are listed in Table 4.2 which are retrieved partly from ARRUDA ET AL. [16] and MIEHE ET AL. [90]. The rest of the material and model parameters are considered according to Table 4.1.

The contour plots in Fig. 4.9(a) reveal the final state of the crack phase–field d for $\dot{u} = 1$ [mm/min] to $\dot{u} = 100$ [mm/min] with elements where $d \geqslant 0.9$ are blanked for the sake of visuality. Unfortunately, as the plastic deformations become dominant within the notched region, extreme mesh distortions present tremendous challenges in regard to numerical convergence, causing the simulation to crush prematurely. Nonetheless, the trend of the red and black solid lines corresponding to $\dot{u} = 1$ [mm/min] and $\dot{u} = 100$ [mm/min], respectively, is tangible in Fig. 4.9(b), manifesting the remarkable loss in the load bearing capacity, thereby indicating the location of fracture. In addition to the three–field coupled thermo–mechano–fracture analyses, we also perform two–field coupled thermo-viscoplastic simulations under $\dot{u} = 1$ [mm/min] and $\dot{u} = 100$ [mm/min] while the onset of crazing is suppressed. By comparing the solid and the dashed lines in Fig. 4.9(b), one can clearly ascertain the damage induced softening due to phase–field evolution, namely the loss in the load bearing capacity of the specimen. Also deduced from the purely thermo-viscoplastic analyses is the effect of thermal softening associated with $\dot{u} = 100$ [mm/min] on the post–yield response which almost overlaps that of $\dot{u} = 1$ [mm/min]. In fact, the struggle between the strain hardening and the thermal softening is tipped in the favor of the latter for relatively high loading rates.

Figures 4.10(a)–(b) depict the state of the temperature θ, the void volume fraction v_f, and the equivalent plastic strain α at $\dot{u} = 1$ [mm/min] and $\dot{u} = 100$ [mm/min], respectively, at three instants where (I) the craze initiates, (II) the crack grows, and fi-

nally (III) at the end of the simulation. Observe that the finite elements where $d \geqslant 0.9$ are blanked for the sake of visuality. The initial thermo-viscoplastic response of the glassy polymer is revealed first by the well–developed plastic regions between two notches. We infer from the distribution of the equivalent plastic strain α that in the case of $\dot{u} = 1$ [mm/min] the material exhibits more ductility. Thermal softning is manifested by the heating inbetween the notches marked by the temperature distribution. As a matter of fact, the higher loading rate leads to greater dissipative heating and thereby higher temperatures, i.e. the maximum value of θ are 346.8 [K] and 427.7 [K] for $\dot{u} = 1$ [mm/min] and $\dot{u} = 100$ [mm/min], respectively. Later, the development of the shear yielding is hindered in regions undergoing crazing whose distribution is comparable under both loading rates, see the evolution of v_f in Figs. 4.10(a)–(b). The maximum values v_f and α attain during the simulation are 0.9 and 1.53 under $\dot{u} = 1$ [mm/min], respectively. These values change slightly but not much for $\dot{u} = 100$ [mm/min] where v_f and α take on 0.8 and 2.23, respectively. With the aid of these simulations, the interplay between loading rate and the temperature is unveiled in a systematic way.

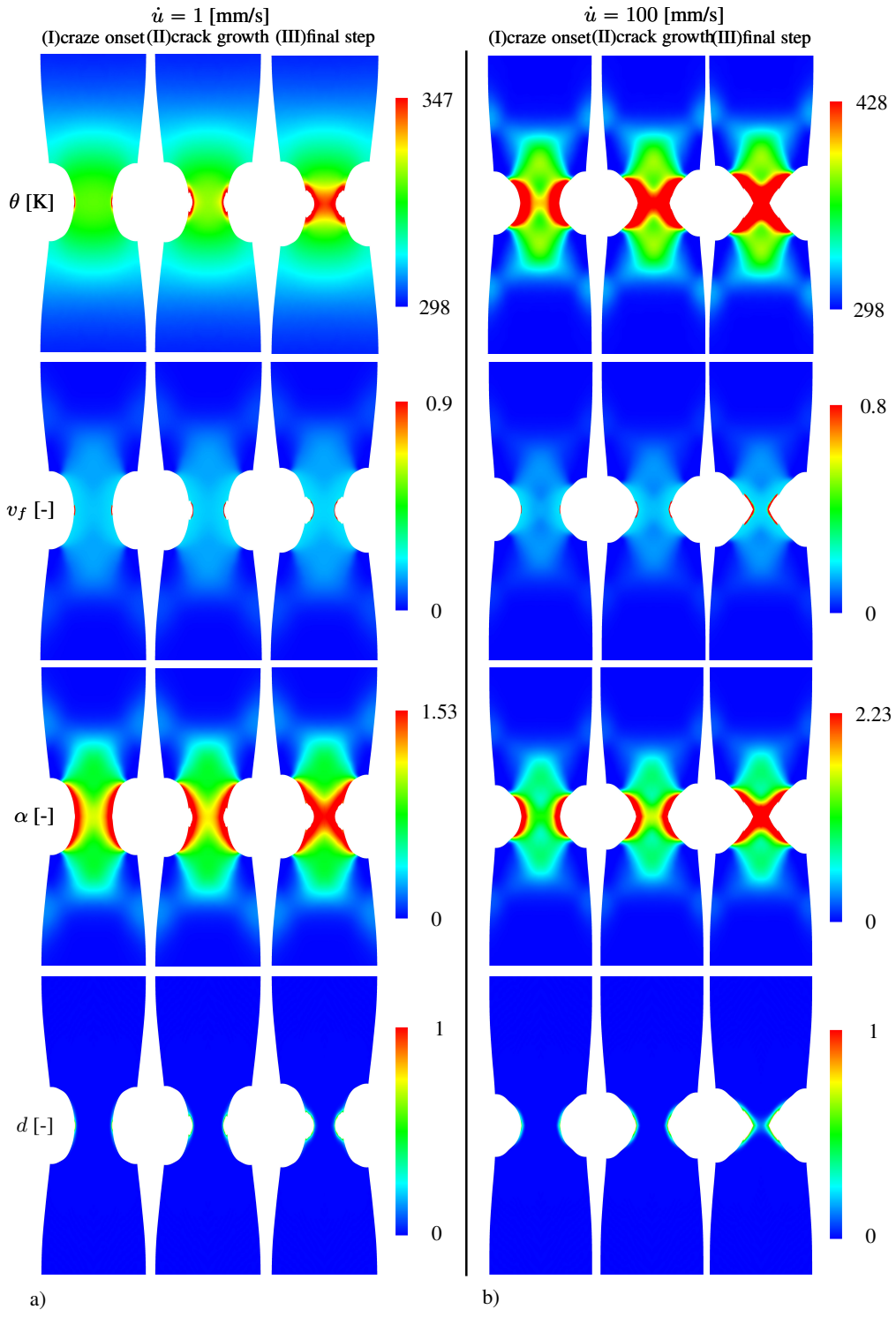

Figure 4.10: Contour plots of the temperature θ in relation to void volume fraction v_f and the amount of plastic strain α and phase field parameter d in the area of interest at (a) $\dot{u} = 1$ [mm/min] at the instants (I) the onset of crazing, (II) during crack growth, and (III) the end of the simulation; (b) $\dot{u} = 100$ [mm/min] at the instants (I) the onset of crazing, (II) during crack growth, and (III) the end of the simulation. Elements where $d \geqslant 0.9$ are blanked for the sake of visuality.

CHAPTER 5

CONCLUSION

The current study presents a three–field thermo–mechano–fracture model for the shear yielding and/or crazing induced failure of amorphous glassy polymers indicated by ductile or brittle mechanical response, respectively. The employed continuum mechanical framework features the Hencky–type elastic, plastic and craze strains in the logarithmic strain space along with the auxiliary variable, i.e. the void volume fraction, in order to characterize the deformation field. Once the mechanical groundwork was laid, the other primary fields such as the crack phase–field elucidating the ruptured state of the material and the temperature field accounting for the change in the temperature of the domain were assigned to the system. Local evolution laws for the plastic strain ε^p by BOYCE ET AL. [26], the craze strain as presented by GEARING & ANAND [46] and the void volume fraction as specified by DAL ET AL. [37] were adopted. The constitutive relations – established entirely in the Eulerian form– essentially entail (i) a Helmholtz free energy function composed of a linear thermo–elastic, thermo–plastic network and a purely thermal contribution; (ii) a degradation function in order to describe the transition from intact to fractured state; (iii) a switch function between shear yielding and crazing; (iv) a failure criterion consisting of the critical equivalent plastic strain and the critical void volume fraction; (v) a dissipation potential function portraying the heat conduction. On the numerical side, the global field equations were temporally discretized by operator splitting algorithm, while a typical Galerkin–type weak formulation established the spatial discretization. Having constructed the local and global Newton–type update algorithms in regard to the dissipative internal and the primary field variables, respectively, the robustness of the model was assessed via several numerical testing. Results obtained shed light on the dependence of the type of the failure on temperature as well as the interplay between

the loading rate and the change in temperature due to dissipative heating.

With this study, while coming up with a new model to understand the fracture of amorphous polymers, it has been also tried to reach up the mechanisms inherent in the microstructure from form to meaning as we have introduced the void volume fraction to the model. On one hand, the model analyses testify the ubiquitous role of loading rate as well as the temperature level in the failure of glassy polymers; on the other hand, the model proposed still sits in the realm of continuum mechanics with all of its limitations, especially, in terms of the number of material and model parameters that soar up with the addition of new primary and auxiliary fields. Crack phase–field approach has been successfully applied to several multi–physics problems including, but not restricted to, isotropic materials, such as AMBATI ET AL. [2], BORDEN ET AL. [21], and MIEHE ET AL. [85, 88, 93] and anisotropic materials as presented by LI ET AL. [76], TEICHTMEISTER ET AL. [107], NGUYEN ET AL. [97], GÜLTEKIN ET AL. [50–52], DENLI ET AL. [39], and MANDAL ET AL. [79]. The use of phase–field poses certain challenges, particularly in the crack propagation in the post–yield region as mentioned in Sec. 4.5. These issues can be circumvented via increasing the polynomial order of the shape functions from $\mathcal{C}^0$ to $\mathcal{C}^1$ continuity so that extremely distorted mesh in the plastically deformed region can be sufficiently treated. Another aspect of future development can be the use of data–driven and/or machine learning approaches, see e.g., ROVINELLI ET AL. [102], CARRARA ET AL. [31], LIU ET AL. [77], in the context of failure in amorphous glassy polymers. These may be assembled to generate more potent and more balanced tools with less material parameters in the prediction of polymer failure.

REFERENCES

[1] F. Aldakheel, C. Miehe, and P. Wriggers. A modified gurson-type plasticity model at finite strains: formulation, numerical analysis and phase-field coupling. *Comput Mech*, 62:815–833, 2018.

[2] M. Ambati, T. Gerasimov, and L. D. Lorenzis. A review on phase-field models of brittle fracture and a new fast hybrid formulation. *Computational Mechanics*, 55:383–405, 2015.

[3] M. Ambati, T. Gerasimov, and L. D. Lorenzis. Phase–field modeling of ductile fracture. *Computational Mechanics*, 55:1017–1040, 2016.

[4] M. Ambati, T. Gerasimov, and L. D. Lorenzis. A phase-field model for ductile fracture at finite strains and its experimental verification. *Computational Mechanics*, 57:149–167, 2016.

[5] N. M. Ames, V. Srivastava, S. A. Chester, and L. Anand. A thermo-mechanically coupled theory for large deformations of amorphous polymers. part ii: Applications. *International Journal of Plasticity*, 25(8):1495–1539, 2009.

[6] L. Anand, N. M. Ames, V. Srivastava, and S. A. Chester. A thermo-mechanically coupled theory for large deformations of amorphous polymers. part i: Formulation. *International Journal of Plasticity*, 25(8):1474–1494, 2009.

[7] L. Anand and M. E. Gurtin. A theory of amorphous solids undergoing large deformations with appl,cations to polymeric glasses. *International Journal of Solids and Structures*, 40:1465–1487, 2003.

[8] E. H. Andrews and L. Bevan. Mechanics and mechanism of environmental crazing in a polymeric glass. *Polymer*, 13(7):337–346, 1972.

[9] A. S. Argon. Physical basis of distortional and dilational plastic flow in glassy polymers. *Journal of Macromolecular Science, Part B*, 8:3:573–596, 1973.

[10] A. S. Argon. A theory for the low-temperature plastic deformation of glassy polymers. *Philosophical Magazine*, 28:4:839–865, 1973.

[11] A. S. Argon. Role of heterogeneities in the crazing of glassy polymers. *Pure and Applied Chemistry*, 43(1-2):247–272, 1975.

[12] A. S. Argon and J. G. Hannoosh. Initiations of crazes in polystyrene. *Philosophical Magazine*, 36:1195–1216, 1977.

[13] A. S. Argon and M. M. Salama. Growth of crazes in glassy polymers. *Philosophical Magazine*, 36:1217–1234, 1977.

[14] E. M. Arruda and M. C. Boyce. A three-dimensional constitutive model for the large stretch behavior of rubber elastic materials. *Journal of the Mechanics and Physics of Solids*, 41:389–412, 1993.

[15] E. M. Arruda and M. C. Boyce. A three-dimensional constitutive model for the large stretch behavior of rubber elastic materials. *Journal of the Mechanics and Physics of Solids*, 41(2):389–412, 1993.

[16] E. M. Arruda, M. C. Boyce, and R. Jayachandran. Effects of strain rate, temperature and thermomechanical coupling on the finite strain deformation of glassy polymers. *Mechanics of Materials*, 19:193–212, 1995.

[17] S. Basu and E. van der Giessen. A thermo-mechanical study of mode i, small-scale yielding crack-tip fields in glassy polymers. *International Journal of Plasticty*, 18:1395–1423, 2002.

[18] L. L. Berger and E. Kramer. Chain disentanglement during high-temperature crazing of polystrene. *Macromolecules*, 20:1980–1985, 1987.

[19] J. S. Bergström. *Large strain time-dependent behavior of elastomeric materials*. PhD thesis, Massachusetts Institute of Technology, 1999.

[20] M. J. Borden, T. J. R. Hughes, C. M. Landis, A. Anvari, and I. J. Lee. A phase-

field formulation for fracture in ductile materials: Finite deformation balance law derivation, plastic degradation, and stress triaxiality effects. *Computer Methods in Applied Mechanics and Engineering*, 312:130–166, 2016.

[21] M. J. Borden, T. J. R. Hughes, C. M. Landis, and C. V. Verhoosel. A higher-order phase-field model for brittle fracture: Formulation and analysis within the isogeometric analysis framework. *Computer Methods in Applied Mechanics and Engineering*, 273:100–118, 2014.

[22] B. Bourdin, G. A. Francfort, and J.-J. Marigo. The variational approach to fracture. *Journal of Elasticity, Springer Verlag, Germany*, 91:5–148, 2008.

[23] P. B. Bowden and J. A. Jukes. The plastic flow of isotropic polymers. *J Mater Sci*, 7:52–63, 1972.

[24] P. B. Bowden and S. Raha. The formation of micro shear bands in polystyrene and polymethylmethacrylate. *Philosophical Magazine*, 22:177:463–482, 1970.

[25] M. C. Boyce, E. L. Montagut, and A. S. Argon. The effects of thermomechanical coupling on the cold drawing process of glassy polymers. *Polymer Engineering and Science*, 32:1073–1085, 1992.

[26] M. C. Boyce, D. M. Parks, and A. S. Argon. Large inelastic deformation of glassy polymers. part i: Rate dependent constitutive model. *Mechanics of Materials*, 7:15–33, 1988.

[27] A. Braides. *Introduction to Homogenization and Gamma-convergence*. Oxford University Press, Oxford, UK, – edition, 1998.

[28] D. Brokken. *Numerical modelling of ductile fracture in blanking*. PhD thesis, Eindhoven University of Technology, 1999. Ph.D. Thesis.

[29] C. Bucknall. New criterion for craze initiation. *Polymer*, 48(4):1030–1041, 2007.

[30] M. Buliga. Energy minimizing brittle crack propagation. *Journal of Elasticity*, 52:201–238, 1998.

[31] P. Carrara, L. De Lorenzis, L. Stainier, and M. Ortiz. Data-driven fracture mechanics. *Computer Methods in Applied Mechanics and Engineering*, 372:113390, 2020.

[32] J. D. Clayton and J. Knap. Phase-field modeling of directional fracture in anisotropic polycrystals. *Computational Materials Science*, 98:158–169, 2015.

[33] A. Cohen. A padé approximant to the inverse langevin function. *Rheological Acta*, 30:270–273, 1991.

[34] A. D638-14. Standard test method for tensile properties of plastics. Technical Report 14, ASTM International, 100 Barr Harbor Drive, PO Box C700, West Conshohocken, PA 19428-2959. United States, 2014.

[35] H. Dal, K. Açıkgöz, and Y. Badienia. On the Performance of Isotropic Hyperelastic Constitutive Models for Rubber-Like Materials: A State of the Art Review. *Applied Mechanics Reviews*, 73(2), 05 2021.

[36] H. Dal, O. Gültekin, and K. Açıkgöz. An extended eight-chain model for hyperelastic and finite viscoelastic response of rubberlike materials: Theory, experiments and numerical aspects. *Journal of the Mechanics and Physics of Solids*, 145:104159, 2020.

[37] H. Dal, O. Gültekin, S. Başdemir, and A. K. Açan. Ductile–brittle failure of amorphous glassy polymers: A phase-field approach. *Computer Methods in Applied Mechanics and Engineering*, 401:115639, 2022.

[38] E. Darabi and M. Itskov. A simple and accurate approximation of the inverse langevin function. *Rheologica Acta*, 54, 2015.

[39] F. A. Denli, O. Gültekin, G. A. Holzapfel, and H. Dal. A phase-field model for fracture of unidirectional fiber-reinforced polymer matrix composites. *Computational Mechanics*, 65:1149–1166, 2020.

[40] W. Döll. Optical interference measurements and fracture mechanics analysis of crack tip craze zones. In H. Kausch, editor, *Crazing in Polymers*, pages

295–341. Springer, Berlin/Heidelberg, 1983.

[41] A. E. Ehret. On a molecular statistical basis for ogden's model of rubber elasticity. *Journal of the Mechanics and Physics of Solids*, 78:249–268, 2015.

[42] R. Estevez, M. Tijssens, and E. van der Giessen. Modeling of the competition between shear yielding and crazing in glassy polymers. *Journal of the Mechanics and Physics of Solids*, 48:2585–2617, 2000.

[43] R. Fleischhauer, H. Dal, M. Kaliske, and K. Schneider. A constitutive model for finite deformation of amorphous polymers. *International Journal of Mechanical Sciences*, 65(1):48–63, 2012.

[44] G. A. Francfort and J. J. Marigo. Revisiting brittle fracture as an energy minimization problem. *Journal of the Mechanics and Physics of Solids*, 46:1319–1342, 1998.

[45] B. P. Gearing and L. Anand. Notch-sensitive fracture of polycarbonate. *International Journal of Solids and Structures*, 41:827–845, 2004.

[46] B. P. Gearing and L. Anand. On modeling the deformation and fracture response of glassy polymers due to shear-yielding and crazing. *International Journal of Solids and Structures*, 41:3125–3150, 2004.

[47] A. N. Gent. Hypothetical mechanism of crazing in glassy plastics. *J. Mater. Sci.*, 5:925–932, 1970.

[48] L. E. Govaert, P. Timmermans, and W. Brekelmans. The influence of intrinsic strain softening on strain localization in polycarbonate: modeling and experimental validation. *Journal of Engineering Materials and Technology*, 122:177–185, 2000.

[49] A. A. Griffith. The phenomena of rupture and flow in solids. *The Royal Society*, 221:163–198, 1921.

[50] O. Gültekin, H. Dal, and G. A. Holzapfel. A phase-field approach to model fracture of arterial walls: Theory and finite element analysis. *Computer Methods in Applied Mechanics and Engineering*, 312:542–566, 2016.

[51] O. Gültekin, H. Dal, and G. A. Holzapfel. Numerical aspects of anisotropic failure in soft biological tissues favor energy-based criteria: A rate-dependent anisotropic crack phase-field model. *Computer Methods in Applied Mechanics and Engineering*, 331:23–52, 2018.

[52] O. Gültekin, S. P. Hager, H. Dal, and G. A. Holzapfel. Computational modeling of progressive damage and rupture in fibrous biological tissues: application to aortic dissection. *Biomech Model Mechanobiol*, 18:1607–1628, 2019.

[53] O. A. Hasan and M. C. Boyce. A constitutive model for the nonlinear viscoelastic viscoplastic behavior of glasy polymes. *Polymer Engineering and Science*, 35(4):331–344, 1995.

[54] P. Haupt. On the mathematical modelling of material behavior in continuum mechanics. *Acta Mechanica*, 100:129–154, 1993.

[55] R. N. Haward, B. M. Murphy, and E. White. Relationship between compressive yield and tensile behavior in glassy thermoplastics. *Journal of Polymer Science*, 9:801–814, 1971.

[56] R. N. Haward and R. J. Young. *The Physics of Glassy Polymers*. Springer Science + Business Media, Dordrecht, Netherlands, 2nd edition, 1997.

[57] G. A. Holzapfel. Nonlinear solid mechanics: a continuum approach for engineering science, 2002.

[58] C. Hui, A. Ruina, C. Creton, and K. Kramer. Micromechanics of crack growth into a craze in a polymer glass. *Macromolecules*, 25:3948–3955, 1992.

[59] Y. Imai and N. Brown. The effect of strain rate on craze yielding, shear yielding, and brittle fracture of polymers at 77k. *Journal of Polymer Science: Polymer Physics Edition*, 14:723–739, 1976.

[60] G. R. Irwin. Onset of fast crack propagation in high strength steel and aluminum alloys. Technical Report 631-030, Naval Research Laboratory, Washington D.C., USA, 1956.

[61] M. Ishikawa, I. Narisawa, and H. Ogawa. Criterion for craze nucleation

in polycarbonate. *Journal of Polymer Science: Polymer Physics Edition*, 15:1791–1804, 1977.

[62] M. Itskov, R. Dargazany, and K. Hörnes. Taylor expansion of the inverse function with application to the langevin function. *Mathematics and Mechanics of Solids*, 17(7):693–701, 2012.

[63] M. Itskov, A. E. Ehret, and R. Dargazany. A full-network rubber elasticity model based on analytical integration. *Mathematics and Mechanics of Solids*, 15(6):655–671, 2010.

[64] H. M. James and E. Guth. Theory of the elastic properties of rubber. *The Journal of Chemical Physics*, 11(10):455–481, 1943.

[65] R. Jedynak. Approximation of the inverse langevin function revisited. *Rheologica Acta*, 54:29–39, 2015.

[66] R. Jedynak. New facts concerning the approximation of the inverse langevin function. *Journal of Non-Newtonian Fluid Mechanics*, 249, 2017.

[67] H. Jiang, J. Zhang, Z. Yang, C. Jiang, and G. Kang. Modeling of competition between shear yielding and crazing in amorphous polymers' scratch. *International Journal of Solids and Structures*, 124:215 – 228, 2017.

[68] R. P. Kambour. Structure and properties of crazes in polycarbonate and other glassy polymers. *Polymer*, 5:143–155, 1964.

[69] G. Keady. The langevin function and truncated exponential distributions. 01 2015.

[70] V. Khiem and M. Itskov. Analytical network-averaging of the tube model: Rubber elasticity. *Journal of the Mechanics and Physics of Solids*, 95:254–269, 05 2016.

[71] U. F. Kocks, A. S. Argon, and M. F. Ashby. *Thermodynamics and kinematics of slip*. Pergamon Press, Headington Hill Hall, Oxford, England, 1st edition, 1975.

[72] E. J. Kramer. Microscopic and molecular fundamentals of crazing. In H. H. Kausch, editor, *Crazing in Polymers. Advances in Polymer Science*, volume 52–53, pages 1–56. Springer, Berlin, Heidelberg, 1983.

[73] M. Kröger. Simple, admissible, and accurate approximants of the inverse langevin and brillouin functions, relevant for strong polymer deformations and flows. *Journal of Non-Newtonian Fluid Mechanics*, 223:77–87, 2015.

[74] C. Kuhn, A. Schlüter, and R. Müller. On degradation functions in phase field fracture models. *Computational Materials Science*, 108:374–384, 2015. Selected Articles from Phase-field Method 2014 International Seminar.

[75] W. Kuhn and F. Grün. Beziehungen zwischen elastischen konstanten und dehnungsdoppelbrechung hochelastischer stoffe. *Kolloid-Zeitschrift*, 101:248–271, 1942.

[76] B. Li, C. Peco, D. Millán, I. Arias, and M. Arroyo. Phase-field modeling and simulation of fracture in brittle materials with strongly anisotropic surface energy. *International Journal for Numerical Methods in Engineering*, 102:711–727, 2015.

[77] X. Liu, C. Athanasiou, N. Padture, B. Sheldon, and H. Gao. Knowledge extraction and transfer in data-driven fracture mechanics. *Proceedings of the National Academy of Sciences*, 118(23):e2104765118, 2021.

[78] T. K. Mandal, A. Gupta, V. P. Nguyen, R. Chowdhury, and A. de Vaucorbeil. A length scale insensitive phase field model for brittle fracture of hyperelastic solids. *Engineering Fracture Mechanics*, 236:107196, 2020.

[79] T. K. Mandal, V. P. Nguyen, and J.-Y. Wu. A length scale insensitive anisotropic phase field fracture model for hyperelastic composites. *International Journal of Mechanical Sciences*, 188:105941, 2021.

[80] B. C. Marchi and E. M. Arruda. An error-minimizing approach to inverse langevin approximations. *Rheologica Acta*, 54:887–902, 2015.

[81] J. Mediavilla, R. Peerlings, and M. Geers. A robust and consistent remeshing-

transfer operator for ductile fracture simulations. *Computers & Structures*, 84(8):604–623, 2006.

[82] G. N. Mercer and A. J. Roberts. A centre manifold description of containment dispersion in channels with varying flow properties. *Siam Journal on Applied Mathematics*, 50:1547–1565, 1990.

[83] G. H. Michler and F. J. Baltá-Calleja. Crazing. In G. H. Michler and F. J. Baltá-Calleja, editors, *Nano- and Micromechanics of Polymers*, pages 119–157. Hanser, 2012.

[84] C. Miehe. Entropic thermoelasticity at finite strains. aspects of the formulation and numerical implementation. *Computer Methods in Applied Mechanics and Engineering*, 120:243–269, 1995.

[85] C. Miehe, F. Aldakheel, and A. Raina. Phase field modeling of ductile fracture at finite strains: A variational gradient-extended plasticity-damage theory. *International Journal of Plasticity*, 84:1–32, 2016.

[86] C. Miehe, F. Aldakheel, and S. Teichtmeister. Phase-field modelling of ductile fracture at finite strains: A robust variational-based numerical implementation of a gradient-extended theory by micromorphic regularization. *International Journal for Numerical Methods in Engineering*, 111:816–863, 2017.

[87] C. Miehe, N. Apel, and M. Lambrecht. Anisotropic additive plasticity in the logarithmic strain space: modular kinematic formulation and implementation based on incremental minimization principles for standard materials. *Computer Methods in Applied Mechanics and Engineering*, 191:5383–5425, 2002.

[88] C. Miehe, H. Dal, L. M. Schänzel, and A. Raina. A phase-field model for chemo-mechanical induced fracture in lithium-ion battery electrode particles. *International Journal for Numerical Methods in Engineering*, 106:683–711, 2016.

[89] C. Miehe, J. M. Diez, and S. Göktepe. Finite viscoplasticity of amorphous glassy polymers in the logarithmicstrain space. *International Journal of Solids and Structures*, 46:181–202, 2009.

[90] C. Miehe, J. M. Diez, S. Göktepe, and L. M. Schänzel. Coupled thermoviscoplasticity of glassy polymers in the logarithmic strain space based on the free volume theory. *International Journal of Solids and Structures*, 48:1799–1817, 2011.

[91] C. Miehe, M. Hofacker, and F. Welschinger. A phase field model for rate-independent crack propagation : Robust algorithmic implementation based on operator splits. *Computer Methods in Apllied Mechanics and Engineering*, 199:2765–2778, 2010.

[92] C. Miehe, L. M. Schänzel, and H. Ulmer. Phase field modeling of fracture in multi-physics problems. part ii. coupled brittle-to-ductile failure criteria and crack propagation in thermo-elastic–plastic solids. *Computer Methods in Apllied Mechanics and Engineering*, 294:486–522, 2015.

[93] C. Miehe, S. Teichtmeister, and F. Aldakheel. Phase-field modelling of ductile fracture: a variational gradient-extended plasticity-damage theory and its micromorphic regularization. *The Royal Society: Philosophical Transactions A*, 374:20150170, 2016.

[94] C. Miehe, F. Welschinger, and M. Hofacker. Thermodynamically consistent phase-field models of fracture: Variational principles and multi-field fe implementations. *International Journal for Numerical Methods in Engineering*, 83:1273–1311, 2010.

[95] V. Morovati, H. Mohammadi, and R. Dargazany. A generalized approach to generate optimized approximations of the inverse langevin function. *Mathematics and Mechanics of Solids*, 24(7):2047–2059, 2019.

[96] S. Narayan and L. Anand. Fracture of amorphous polymers: A gradient-damage theory. *Journal of the Mechanics and Physics of Solids*, 146:104164, 2021.

[97] T.-T. Nguyen, J. Réthoré, J. Yvonnet, and M.-C. Baietto. Multi-phase-field modeling of anisotropic crack propagation for polycrystalline materials. *Computational Mechanics*, 60:289–314, 2017.

[98] R. J. Oxborough and P. B. Bowden. A general critical-strain criterion for crazing in amorphous glassy polymers. *Philosophical Magazine*, 28:3:547–559, 1973.

[99] P. C. Powell and A. J. I. Housz. *Engineering with Polymers*. Stanley Thornes Ltd, Cheltenham, United Kingdom, 2nd edition, 1998.

[100] M. Puso. Mechanistic constitutive models for rubber elasticity and viscoelasticity. 2003.

[101] S. Raha and P. B. Bowden. Birefringence of plastically deformed poly(methyl methacrylate). *Polymer*, 13:174–183, 1972.

[102] A. Rovinelli, M. Sangid, H. Proudhon, and W. Ludwig. Using machine learning and a data-driven approach to identify the small fatigue crack driving force in polycrystalline materials. *npj Comput Mater*, 4(35), 2018.

[103] T. Seelig and E. van der Giessen. Localized plastic deformation in ternary polymer blends. *International Journal of Solids and Structures*, 39:3505–3522, 2002.

[104] T. Seelig and E. van der Giessen. Effects of microstructure on crack tip fields and fracture thoughness in pc/abs polymer blends. *International Journal of Fracture*, 145:205–222, 2007.

[105] S. S. Sternstein and F. Myers. Yielding of glassy polymers in the second quadrant of principal stress space. *Journal of Macromolecular Science, Part B*, 8:3-4:539–571, 1973.

[106] R. L. Taylor. A finite element analysis program. Technical Report –, Department of Civil and Environmental Engineering, University of California at Berkeley, USA, 2017.

[107] S. Teichtmeister, D. Kienle, F. Aldakheel, and M. A. Keip. Phase-field modeling of fracture in anisotropic brittle solids. *International Journal of Non-Linear Mechanics*, 97:1–21, 2017.

[108] M. Tijssens, E. van der Giessen, and L. J. Sluys. Modeling of crazing using a

cohesive surface methodology. *Mechanics of Materials*, 32:19–35, 2000.

[109] Y. Tomita and S. Tanaka. Prediction of deformation behavior of glassy polymers based on molecular chain network model. *Int. J. Solids Structures*, 32:3423–3434, 1995.

[110] L. Treloar. The photoelastic properties of short-chain molecular networks. *Transactions of the Faraday Society*, 50:881–896, 1954.

[111] L. Treloar. *The physics of rubber elasticity*. Clarendon Press, Oxford, third edition, 1975.

[112] L. R. G. Treloar. The elasticity of a network of long-chain molecules-ii. *Transactions of the Faraday Society*, 39:241–246, 1943.

[113] K. Valanis. A theory of viscoplasticity without a yield surface. *Archives of Mechanics*, 23:517–533, 1971.

[114] M. C. Wang and E. Guth. Statistical theory of networks of non-gaussian flexible chains. *The Journal of Chemical Physics*, 20(4):1144–1157, 1952.

[115] I. M. Ward and P. R. Pinnock. The mechanical properties of solid polymers. *British Journal of Applied Physics*, 17:3–32, 1966.

[116] P. D. Wu and E. van der Giessen. On improved network models for rubber elasticity and their applications to orientation hardening in glassy polymers. *J. Mech. Phys. Solids*, 41(3):427–456, 1993.

[117] P. D. Wu and E. van der Giessen. Analysis of shear band propagation in amorphous glassy polymers. *Int. J. Solids Structures*, 31(11):1493–1517, 1994.

[118] P. D. Wu and E. van der Giessen. On neck propagation in amorphous glassy polymers under plane strain tension. *International Journal of Plasticity*, 11(3):211–235, 1995.

[119] A. Yang, E. Kramer, C. Kuo, and S. Phoenix. Craze fibril stability and breakdown in polysterene. *Macromolecules*, 19:2010–2019, 1986.

[120] B. H. Zimm. Dynamics of polymer molecules in dilute solution: Viscoelastic-

ity, flow birefringence and dielectric loss. *The Journal of Chemical Physics*, 24(2):269–278, 1956.